University of Southampton

Faculty of Physical Sciences and Engineering

Optoelectronics Research Centre

Toroidal excitations in free-space and metamaterials

Timothy Andrew Raybould

Thesis for the degree Doctor of Philosophy

April 13, 2017

UNIVERSITY OF SOUTHAMPTON

ABSTRACT

FACULTY OF PHYSICAL SCIENCES AND ENGINEERING

OPTOELECTRONICS RESEARCH CENTRE

Doctor of Philosophy

Toroidal excitations in metamaterials and free-space

by Timothy Andrew Raybould

Toroidal excitations represent an intriguing new concept in classical electrodynamics that is rapidly becoming increasingly important in the interpretation of light-matter interactions. This thesis reports on new manifestations of electromagnetic toroidal excitations, both localised in matter, and propagating through free-space.

I have developed a set of new computational frameworks for evaluating the creation, propagation, and interaction of toroidal excitations. This framework shall form a key basis for the future study of toroidal excitations in free-space and matter. Key results of this framework are outlined below.

I have developed a methodology for generating “focused doughnut” pulses from metasurface arrays of dipole resonators. Numerical simulations indicate the generated pulse from such an array would be a 93% match for an ideal “focused doughnut”. The generation scheme has been tested and found to perform well under anticipated experimental bandwidth limitations. Generation of a continuous train of “focused doughnut” pulses from a frequency-comb-like excitation of the array has been demonstrated.

I have, for the first time, investigated the interactions of “focused doughnut” pulses with continuous and particulate matter. I report on the peculiar field transformations that the “focused doughnut” pulse experiences under reflection at an interface, and the broadband modal excitation when incident on small particles. This includes the excitation of multiple, dominant toroidal dipolar resonances and dynamic anapole modes.

I have demonstrated that toroidal excitations contribute to optical activity. Using a chiral metamaterial structure, I observed a new microscopic mechanism for circular dichroism, underpinned by the resonant excitation of the toroidal dipole and the electric quadrupole. This toroidal circular dichroism supplements the well-established mechanism involving electric dipole and magnetic dipole transitions.

I have demonstrated the superior coupling of radially polarised vector beams to toroidal excitations in matter. The toroidal modes excited possess high quality factors of ~ 124 and radiate with an almost exclusively dipolar radiation pattern.

Contents

List of Figures

DECLARATION OF AUTHORSHIP

I, Timothy Andrew Raybould, declare that the thesis entitled "Toroidal excitations in free-Space and metamaterials" and the work presented in the thesis are both my own, and have been generated by me as the result of my own original research. I confirm that:

- this work was done wholly or mainly while in candidature for a research degree at this University;
- where any part of this thesis has previously been submitted for a degree or any other qualification at this University or any other institution, this has been clearly stated;
- where I have consulted the published work of others, this is always clearly attributed;
- where I have quoted from the work of others, the source is always given. With the exception of such quotations, this thesis is entirely my own work;
- I have acknowledged all main sources of help;
- where the thesis is based on work done by myself jointly with others, I have made clear exactly what was done by others and what I have contributed myself;
- parts of this work have been published as the journal papers and conference contributions listed in Appendix F.

Signed: ____________________

Date: ____________________

Acknowledgements

This PhD could not have been completed without the help and support of those around me. Here I would like to thank those people who have been instrumental in helping me reach this stage, in particular:

- My primary supervisor Prof. Nikolay I. Zheludev for his guidance, enthusiasm, and expertise; and for all the opportunities that have been provided to me over the course of my studies.
- My additional supervisors Dr. Vassili A. Fedotov and Dr. Nikitas Papasimakis, who have been constant sources of advice and expertise on all aspects of my research from day one.
- Prof. Ian J. Youngs and the Defence Science and Technology Laboratory (DSTL) for providing funding for my studentship and for continually supporting my research.
- Members of the Nanophotonics and Metamaterials group for all their help and advice. In particular, Dr. Vassili Savinov for enduring my constant querying and for providing a wealth of insight into toroidal electrodynamics; and Dr. Edward T. F. Rogers for his expertise on Fourier propagation methods.
- My external collaborators, without whom some of my research would not have been possible. My thanks go to Dr. Wei Ting Chen and Prof. Din Ping Tsai for fabrication of the chiral toroidal metamaterial; and to Dr. Ilya Kuprov for his insights into optical activity.
- Derek Evans, my high school physics teacher; and Dr. Thomas J. Constant, who inspired me to study physics at undergraduate and postgraduate levels respectively.
- My family, in particular my mother Suzanne Raybould, for their unwavering support throughout my PhD and in all the years before.
- And finally, Katie, for being a constant source of love, support, and sanity.

Chapter 1

Introduction

1.1 Motivation

The manipulation of light-matter interactions forms the core basis for a huge part of modern science and technology. The study of such interactions dates back over hundreds of years, and has resulted in a strong theoretical and experimental framework that has lead to a wide range of applications acrooss all of modern society. In recent years, new paradigms such as "metamaterials" [1–3] and "transformation optics" [4–6] have emerged, allowing new unprecedented of control of electromagnetic radiation and its interaction with media. One new paradigm which is of particular interest is that of toroidal electrodynamics, which has seen a rapid expansion over the past 6 years since the first explicit observation of dynamic toroidal excitations in 2010 [7].

As the name suggests, toroidal electrodynamics concerns electromagnetic configurations that topologically resemble a torus. Toroidal excitations can exist both as localised electromagnetic excitations in a medium, and as toroidal light pulses that propagate through free-space.

This thesis aims to add to the growing body of work on toroidal electrodynamics with a demonstration of a new chiral phenomena in metamaterials mediated by toroidal excitations (Chapter 3), exploiting structured light to drive toroidal modes (Chapter 4), and a thorough examination of propagating toroidal pulses in the context of their interactions with matter (Chapter 5) and potential generator schemes to synthesise these complex excitations (Chapter 6). It is expected that the results presented here could have a wide range of potential applications, particularly in terms of spectroscopy and sensing of molecules/structures with toroidal topology.

The remainder of this chapter [Section 1.2] shall provide a history of the field of toroidal electrodynamics, both in matter and free-space, to provide context for the research presented throughout the thesis. The chapter will conclude [Section 1.3] with an overview of the thesis structure.

1.2 Introduction to toroidal electrodynamics

The research in this thesis is concerned primarily with the field of toroidal electrodynamics, and demonstrating new related phenomena in both matter and free-space. As such, it is instructive to first give a suitable background to this field such that the reader is comfortable with the context and terminology which will be referred to throughout this thesis.

Light-matter interactions are of a fundamental importance to modern science and technology, with applications such as telecommunications, information processing, data storage, spectroscopy, imaging, and light-assisted manufacturing standing out as key examples. The multipole expansion serves as a ubiquitous tool for understanding such interactions [8–11], commonly understood as being composed of electric and magnetic multipole excitations, corresponding to charges and loop currents respectively. As such, interpretations of light matter interactions are largely framed in terms of these electric or magnetic multipoles.

Toroidal electrodynamics complete the multipole paradigm. Toroidal electrodynamics, as the name suggests, is a field concerned with electromagnetic excitations that are topologically connected to a torus, a topology distinct from the conventional electric and magnetic excitations. Toroidal multipoles, originally referred to as moments, first appeared in work by Zel'dovich in 1957 [12], who introduced toroidal current configurations in the context of nuclear physics to account for parity violating weak interactions. Since then toroidal moments have been studied in the context of nuclear [13], atomic [14], and molecular physics [15]; classical electrodynamics [16, 17], and solid state physics [18, 19].

For clarity, we divide the field of toroidal electrodynamics into three categories [Fig. 1.1]. The static toroidal moments, with the dipole term well known as an anapole, were the first to be established in the literature as a configuration of static currents flowing on the surface of a torus, equivalent to a ring a static magnetic dipoles aligned head to tail [Fig. 1.1(a)]. The dynamic toroidal moments represent a third independent family of dynamic electromagnetic multipoles (rather than an alternate expansion or higher order corrections) alongside the dynamic electric and magnetic multipoles. The dynamic toroidal dipole (the lowest order excitation) consists of currents oscillating on the meridians of a torus, leading to a closed loop of magnetic field confined within [Fig. 1.1(b)]. In addition to the static and dynamic toroidal excitations in matter, there exist localised toroidal waveforms that can propagate freely through free-space i.e. propagating toroidal excitations. These were first predicted in 1996 [20] and were termed "*focused doughnut*" (FD) pulses. Topologically, the FD pulses closely resemble the static and dynamic toroidal excitations in matter [Fig. 1.1(c)].

A large part of the motivation for the study of toroidal electrodynamics is derived from

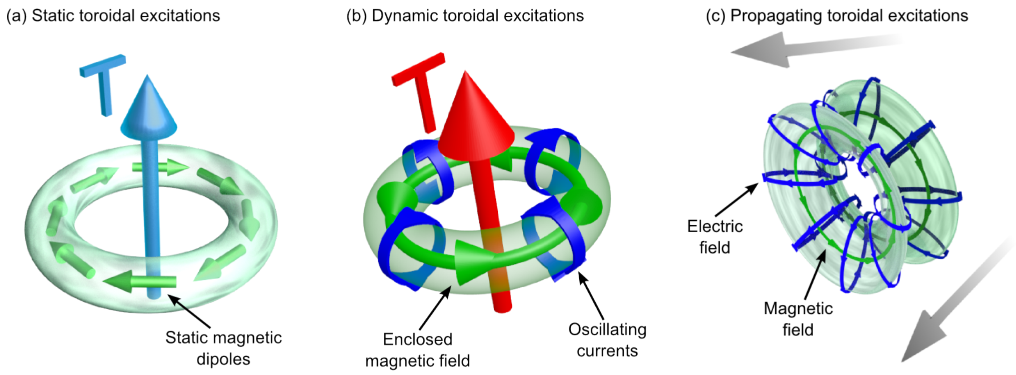

Figure 1.1: ***Static, dynamic and propagating toroidal excitations.*** *(a) shows a schematic of a static (magnetic) toroidal moment creating by a toroidal ordering of static currents and magnetic dipoles. (b) shows the lowest order dynamic toroidal multipole - the toroidal dipole - created by poloidal currents oscillating on the meridians of a torus, enclosing a confined magnetic field. (c) shows a localised toroidal electromagnetic waveform that can propagate through free-space. It is known as a "focused doughnut" pulse, illustrated here in a TM configuration.*

the ubiquity of toroidal structures in nature on a wide variety of scales [Fig. 1.2]. The existence of toroidal currents in atomic nuclei represents the smallest known existence of toroidal symmetry [Fig. 1.2(a)] [12] (though it is noted that anapole excitations have been suggested as a candidate for dark matter [25]). Hexa-aryl benzenes [Fig. 1.2(b)] and toroidal fullerenes [Fig. 1.2(b)] are two examples of chemical compounds that exhibit toroidal topology, with the toroidal fullerenes having been demonstrated as possessing toroidal moments [15]. Several important biological compounds, in particular those involved in DNA binding have been identified as possessing toroidal symmetry [Fig. 1.2(d)-(f)]. Aside from the well known toroidal red blood cells, on a larger biological scale, recent work has shown the existence of a doughnut-shaped region in the brains of fruit flies that acts as a form of compass [26].

The next three sections shall examine the development of toroidal electrodynamics from the early considerations of static toroidal moments in condensed matter, to the recent experimental and numerical works on dynamic toroidal multipoles and propagating toroidal excitations.

1.2.1 History of localised toroidal excitations

Static toroidal moments

Of the three types of toroidal excitation identified in the previous section, the first to be introduced were the static toroidal moments, presented as a configuration of static currents flowing on the surface of a torus [Fig. 1.1(a)]. We note that historically there have been two types of static toroidal moment considered in this context: electric (ax-

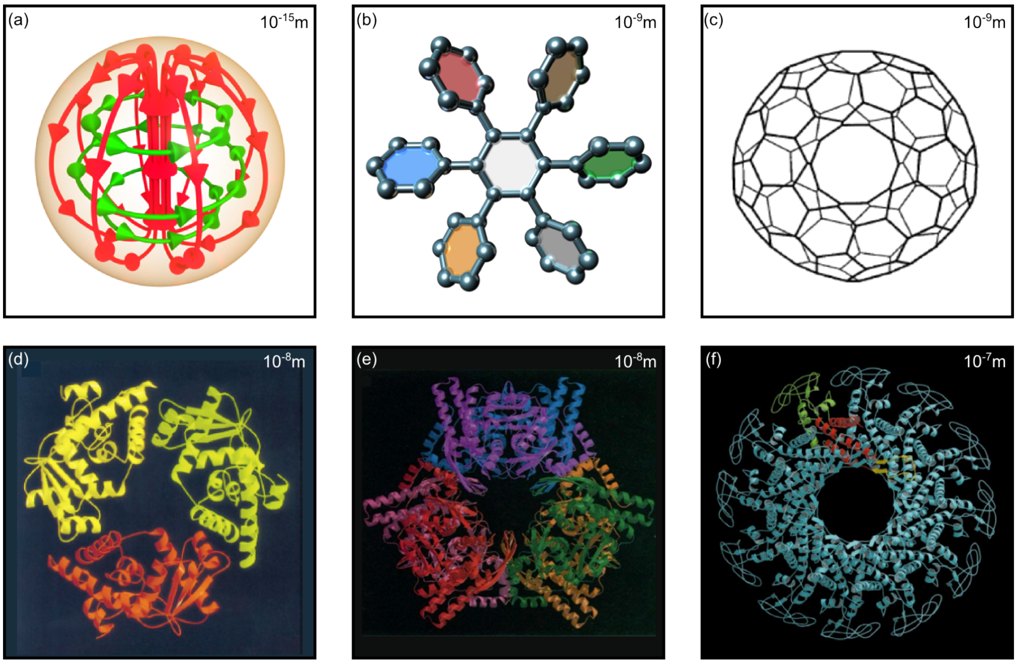

Figure 1.2: ***Toroidal structures in biology and chemistry.*** *This figure shows examples of structures in biology and chemistry that exhibit toroidal topology. The characteristic length scale of these structures is given in the upper right of each figure. (a) shows the anapole moment within the nuclei of atoms, whereby nuclear poloidal currents (red) enclose a closed loop of magnetic field. (b) shows the compound hexa-aryl benzene, composed to seven linked benzene rings [21]. (c) shows a carbon fullerene arranged in a toroidal configuration. Figure adapted from Ref. [15]. (d) shows the toroidal structure of the lambda-exonuclease. Figure adapted from Ref. [22]. (e) shows the DNA binding protease Bleomycin Hydrolase, Ga16. Figure adapted from Ref. [23]. (f) shows the structure of the bacteriophage phi29 DNA packaging motor. Figure adapted from Ref. [24].*

ial) and magnetic (polar). The first arises from vortex-like configurations of electric dipoles [18], whereas the second arises from the aforementioned current configuration. However, only the magnetic (polar) toroidal moments are generally considered, due to the absence of magnetic charge-currents in established electromagnetism [18]. Hereafter we shall refer only to the magnetic toroidal moments unless stated otherwise.

Historically, these excitations were also known as anapoles. A key distinction between static toroidal moments and the conventional static electric and magnetic moments concerns their interaction with an external field. In contrast to static electric and magnetic moments, the currents of the static toroidal moments create a magnetic field confined purely within the torus with zero field external to this. As such they do no interact directly with external electric and magnetic fields [12]. Initially, static toroidal moments were introduced as a mechanism in nuclear physics to explain parity-violating weak interaction [12,14]. However they have since become an established formalism in the study of condensed matter physics [19,27].

In terms of the nuclear toroidal moment, the first explicit experimental evidence of this came in 1997. Observation of parity non-conserving atomic transitions in caesium atoms allowed for explicitly determining how the nuclear anapole contributes through its interaction with the electron cloud [28].

Toroidal multipoles can be described within condensed matter physics by an order parameter, termed toroidization or toroidal polarisation, analogous to the macroscopic electric polarization and magnetization [29]. The toroidization represents the density of toroidal dipole moments. A macroscopic toroidization emerges from configurations of local toroidal moments that exhibit long-range order [30]. Materials that can exhibit macroscopic toroidization are known as ferrotoroids, analogous to ferroelectrics and ferromagnets, and are expected to exhibit unique forms of magnetic response [31–33] and non-reciprocal reflection and dichroism [27]. It has been suggested that ferrotoroids could be utilised for data storage applications [34, 35].

Toroidal ordering in the solid state was first discussed in 1946 by Kittel in his work on ferromagnetic domains of small particles [36]. Such toroidal ordering was confirmed to exist in 1974 in compounds known as boracites [37]. This was followed by as series of observations confirming static toroidal moments in pyroxines and olivines [38, 39].

Explicit observation of ferrotoroidal domains was made in 2007 in an olivine crystal ($LiCOPO_4$), with the domain orientations identified by second harmonic generation [40]. These findings were confirmed by a follow-up work that observed hysteretic effects characteristic of a ferroic state [41]. This has cemented ferrotoroidicity as the fourth form of ferroic order (including ferroelectricity, ferromagnetism and ferroelasticity).

Dynamic toroidal moments

Discussion of the dynamic toroidal multipoles began significantly after the introduction of the static toroidal moments. The 1990's saw a series of papers which examined the radiation properties of time-dependent toroidal current configurations of the form [16, 19, 42, 43]:

$$\mathbf{J}(t,\mathbf{r}) = \nabla \times \nabla \times \left(c\mathbf{T}(t)\delta^{(3)}(\mathbf{r}) \right). \tag{1.1}$$

Where $\mathbf{J}(t)$ represents a time dependent current density and $\mathbf{T}(t)$ represents a time dependent toroidization vector i.e. density of toroidal dipoles, with the delta function defining it as point-like as per the conventional multipole expansion.

Several works have now presented a full dynamic Cartesian multipole expansion which explicitly includes the dynamic toroidal multipoles as a separate family from the conventional electric and magnetic multipoles [44–46]. This has not been without controversy however, with the inclusion or omission of toroidal multipoles from the multipole expansion being a topic of ongoing discussion [47–49]. The inclusion of toroidal multipoles in equivalent descriptions such as Mie theory has also attracted attention [50,51]. The explicit inclusion of toroidal multipoles in the multipole expansion and reconciling this with the Mie expansion shall be discussed in detail in Sections 2.1.1 and 2.1.2. Specifically, it shall be shown that although both the charge-current multipole expansion and the vector spherical harmonic Mie expansion represent complete expansions, the toroidal multipoles appear explicitly in the charge-current multipole expansion and implicitly in the Mie expansion. The relevance of toroidal multipoles in light–matter interactions has direct implications for the interpretation of electromagnetic excitation spectra in media with elements of toroidal topology, and justifies the consideration of toroidal moments as a separate family of multipoles.

The observation of dynamic toroidal responses is complicated by contributions of electric and magnetic multipoles, which frequently mask the toroidal response of a medium. This is a consequence of the scattering of electromagnetic waves by electric, magnetic and toroidal dipoles scaling as $\sim (R/\lambda)$, $\sim (R/\lambda)^2$, and $\sim (R/\lambda)^3$ respectively, where R is the characteristic length scale of the molecule and λ is the free-space wavelength [42, 44, 52]. However, it can be expected that the dynamic toroidal excitations shall play an increasingly important role as the size of the molecule approaches the free-space wavelength i.e. $R \leq \lambda$. Thus the criteria for observing a toroidal response can be summarised as an electromagnetically large molecule with elements of toroidal symmetry. Furthermore, toroidal dipolar transitions are of the same order as experimentally observed magnetic quadrupole transitions [53], suggesting that toroidal transitions could be experimentally accessible.

The first explicit observation of a dynamic toroidal response was made using the metamaterial paradigm [7], which allows for engineering of a structure to enhance the toroidal response, whilst suppressing the lower-order electric and magnetic excitations through structural design. The history of these so-called toroidal metamaterials shall be discussed in the following section.

1.2.2 Localised toroidal excitations in metamaterials

Before proceeding, it is instructive to form a concrete definition of the term "metamaterial". We define metamaterial to be an artificial material designed to exhibit a specific response through structuring on a sub-wavelength scale [1, 2]. This has included thermal metamaterials [54, 55], mechanical metamaterials [56–58], acoustic metamaterials [59, 60], and electromagnetic metamaterials. In this body of work, only metamaterials designed to exhibit an electromagnetic response are considered, and so the term "metamaterial" shall refer exclusively to "electromagnetic metamaterial".

As such, metamaterials are composed of arrays of individual electromagnetic resonators known as meta-atoms or meta-molecules. The size and spacing of these building blocks

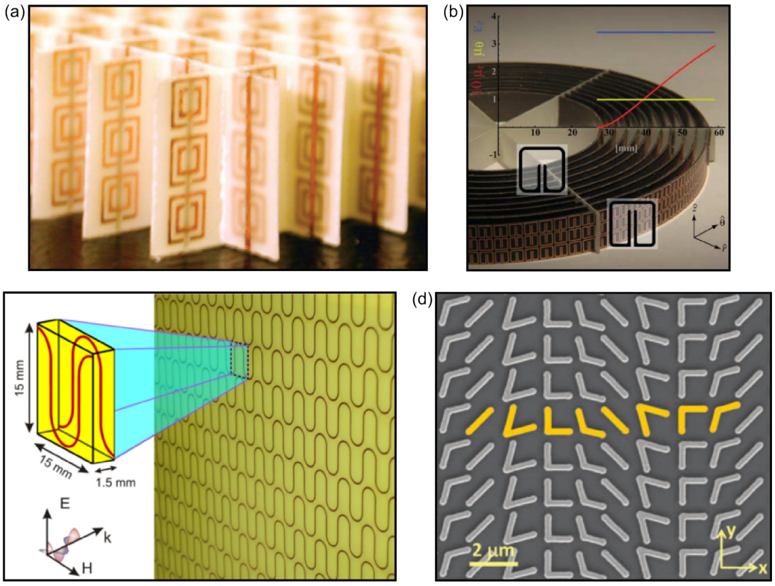

Figure 1.3: ***Examples of electromagnetic metamaterials.*** *(a) shows the first demonstration of a material with a negative refractive index. Figure adapted from Ref. [64]. (b) depicts a two dimensional metamaterial invisibility cloak for the microwave regime. Figure adapted from Ref. [65]. (c) shows a metamaterial exhibiting slow light and an analogue of electromagnetic induced transparency. Figure adapted from Ref. [66]. (d) gives a plasmonic metasurface for demonstration of anomalous reflection and refraction. Figure adapted from Ref. [67].*

is chosen to be smaller than the characteristic wavelength of the driving electromagnetic radiation i.e. sub-λ. This ensures that metamaterials respond as homogeneous media. Arrays in three and two dimensions are most common, with one dimensional structures being somewhat rarer [61]. Two dimensional arrays are also referred to as metasurfaces [62]. Additionally, these arrays can be both periodic and random in nature [63].

The concept of artificial sub-λ composites can be traced back to the work of J.C. Bose on millimeter-wave structures such as layered tin-foil and twisted jutes [68]. Although the exact beginning of metamaterials research in a modern sense is debatable, a large body of early research focused on the design of metamaterials with a simultaneous negative permeability and permittivity, and thus a negative refractive index [Fig. 1.3(a)] [64, 69, 70]. Additional key inital results which laid the foundation for future metamaterial research included artificial magnetism [71], electromagnetic cloaking [Fig. 1.3(b)] [4, 5, 65], and perfect [72] and hyper lenses [73, 74].

Since then, the field of metamaterials research has experienced rapid expansion as a platform to observe fundamental and novel electromagnetic phenomena and provide potential practical solutions for a variety of electromagnetic applications. Some important results have included plasmonic metamaterials [75], superconducting metamaterials [76–79], slow light [Fig. 1.3(c)] [66, 80], superconducting photonics [76–78], lasing spasers [81, 82], spatiotemporal light control [83], directed emission and metamaterial antennas [84, 85], reconfigurable metamaterials [86], beam steering and shaping [Fig. 1.3(d)] [62, 67, 87], perfect metamaterial absorbers [88, 89], and nonlinear metamaterials [90, 91]. Future directions for metamaterial research includes quantum metamaterials [92–94], and use of novel materials such as graphene [95,96], topological insulators [97], and phase change materials [98, 99].

The first example of a metamaterial designed to exhibit a toroidal response consisted of an periodic array of toroidal solenoids. It was predicted that such a metamaterial would exhibit a strong toroidal response, in sharp contrast to conventional materials, and would exhibit backwards propagating waves and negative refraction [100]. This was followed by the first experimental observation of a toroidal response in a metamaterial structure composed of a microwave-scale array of chiral toroidal solenoids [101]. Although the circular dichroism spectra of the metamaterial revealed a non-negligible contribution from the toroidal dipole, the feature was masked by stronger contributions from the conventional electric and magnetic multipoles.

The first observation of an unambiguous toroidal response was reported in 2010 in a metamaterial composed of four split-ring resonators arranged in a ring [7]. The presence of the toroidal dipole was confirmed through a multipole analysis of the sharp resonance feature in the transparency spectrum of the metamaterial, and through examination of the near-field topology of the metamolecule. When under resonant excitation the metamolecule supports a closed loop of magnetic field threading through the split rings - a field configuration that is typical of a toroidal dipole [Fig. 1.4(a)]. The design of the metamolecule formed a template for other structures seeking to enhance the toroidal response and suppress the conventional electric and magnetic multipoles [102, 103].

Since this first explicit demonstration, a wide variety of metamaterial structures have been demonstrated that exhibit strong toroidal responses. A key theme of further research was to simplify the design of toroidal metamaterials, thus allowing for simplified fabrication processes. Planar structures supporting toroidal moments are a key example of this theme [Fig. 1.4(b)] [104–106]. It can be noted however that these designs are not truly planar with respect to the propagation direction. It is demonstrated in Ref. [107] that toroidal dipoles excited in a truly planar structure would not contribute to scattering in the far-field.

The scaling down of the split-ring resonator design has extended the observation of toroidal responses to terahertz [114] and optical regimes [115, 116]. The challenges of manufacturing nano-scale split ring resonators in a toroidal configuration have been overcome by the use of simpler structures such as bars [Fig.1.4(d)] [109] and discs [117, 118]. Despite Ohmic losses damping toroidal responses in the optical part of the spectrum, numerous comparatively simple systems have been found to support toroidal responses. These include bas-relief patterns that support spoof plasmons [Fig. 1.4(e)] [119], ring shaped grooves under illumination at oblique incidence [110], and

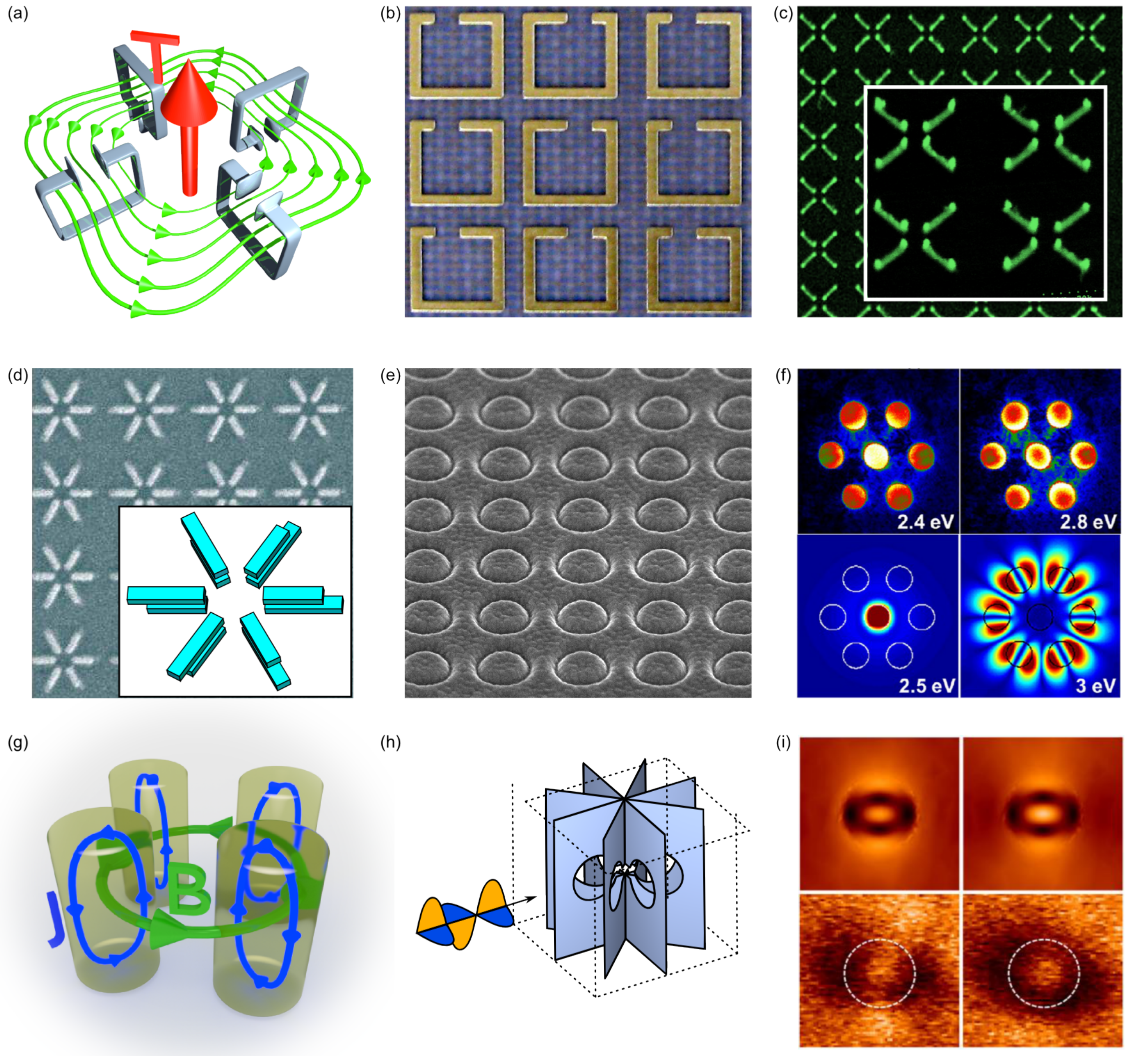

Figure 1.4: ***Toroidal metamaterials.*** *This figure shows examples of metamaterial structures exhibiting a toroidal response. (a) gives a schematic of the metamaterial unit cell used for the first demonstration of a toroidal dipolar resonance [7]. (b) shows a planar low-loss metamaterial based on split-ring resonators that supports a toroidal response. Figure adapted from Ref. [104]. (c) shows a structure exhibiting a plasmonic toroidal response at optical frequencies. Figure adapted from Ref. [108]. (d) also illustrates an optical-scale toroidal metamaterial, constructed using asymmetric bars. Figure adapted from Ref. [109]. (e) utilises spoof plasmons excited at oblique incidence to achieve a toroidal dipolar resonance. Figure adapted from Ref. [110]. (f) shows plasmonic oligomers consisting of voids in metallic films that exhibit a toroidal response when driven by a free-electron beam. Figure adapted from Ref. [111]. (g) illustrates a toroidal response in a purely dielectric structure of four cylinders without any metallic elements [112]. (h) shows a toroidal-void metamaterial that exhibits resonant transparency owing to destructive interference between electric and toroidal dipolar excitations [113]. (i) depicts the near-field topology of a toroidal excitation in a dielectric nanoparticle. Figure adapted from Ref. [51].*

plasmonic core-shell nanoparticles [120]. Furthermore a plasmonic oligomer structure under excitation with an electron beam has been shown to exhibit toroidal modes [Fig. 1.4(f)] [111]. More recent studies have been moving towards novel materials and applications for toroidal responses, including novel laser emitters [82], low-loss dielectrics [Fig. 1.4(g)] [112], superconducting structures [105], and excitation with structured vector beams [121].

In addition to studies concerning the optimisation of toroidal responses in various regimes, there have been key works on the interplay between toroidal modes and conventional multipoles in metamaterials. This has manifested primarily in the study of non-radiating configurations mediated by electric and toroidal dipole excitation. The first observation of a structure supporting destructive interference between electric and toroidal excitations was made in 2013 in a toroidal-void metamaterial under microwave illumination [Fig. 1.4(h)]. Similar resonances corresponding to non-radiating configurations have since been observed in the optical regime, with dielectric nanoparticles [Fig. 1.4(i)] [51], core-shell nanowires [122], and hybrid nanoparticles [120] supporting these modes.

Toroidal excitations have been studied further in the context of more esoteric applications, for example lasing spasers [81, 82] and qubits for quantum computations [123], which take advantage of the weak coupling of toroidal modes to the surrounding environment.

This thesis shall investigate new avenues of toroidal excitations in artificial structures and shall be reported on further in Chapters 3 and 4.

1.2.3 Propagating toroidal excitations

The field of toroidal electrodynamics has historically been concerned with localised toroidal excitations in matter, where the excitations are specifically charge-current in nature. However, there is now growing interest in expanding the field to include the existence of toroidal excitations that propagate through free-space. Here, rather than the ordering of charges and currents, the toroidal topology arises as a result of the confinement of electric and magnetic fields in free-space.

Beams with toroidal topology are ubiquitous throughout research in optics, and occurs for optical beams with radial or azimuthal polarisation which precludes the existence of a field on axis. The relationship between the topology of these toroidal beams and the toroidal excitations in matter has been identified and research has been conducted to exploit this similarity.

Particular interest however is directed at a peculiar set of electromagnetic pulses with toroidal topology known as “focused doughnut” pulses. These were first introduced as theoretical constructs by Hellwarth and Nouchi in 1996 [20] as part of

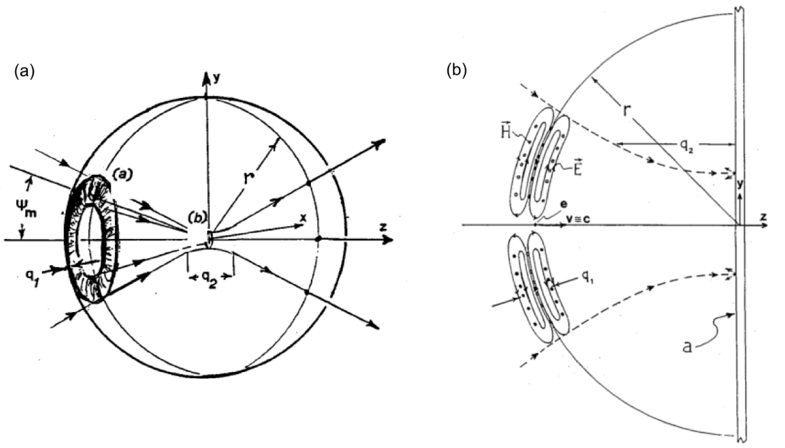

Figure 1.5: ***Schematics of "focused doughnut" pulses.*** *This figure gives artistic impressions of the fields, topology, and evolution of the "focused doughnut" pulse. (a) shows the original schematic provided by Hellwarth and Nouchi in their 1996 paper [20]. The characteristic parameters q_1 and q_2 are identified, as well as the far-field diffraction angle ϕ_m. The envelope of the pulse is traced as it propagates through focus. (b) shows the schematic of a "focused doughnut" pulse co-propagating with an electron, with the intent of imparting energy to the electron through interaction with the longitudinal field components. Figures are adapted from Ref. [20].*

Ziolkowski's EDEPT family of electromagnetic pulses [124]. In a similar way to how the toroidal multipoles in matter form part of a complete expansion of the inhomogeneous Maxwell's equations in matter, the "focused doughnut" pulses exists as exact, finite energy solutions to the homogeneous Maxwell's equations in free-space. They exist purely as few cycle pulses (either single or $1\frac{1}{2}$ cycle) in both *transverse electric* (TE) or *transverse magnetic* (TM) configurations, which broadly correspond to azimuthally and radially polarised forms respectively. Fig. 1.5(a) gives the original schematic from Hellwarth and Nouchi's 1996 paper [20], showing the topology of the FD pulse as it evolves through focus at $x, y, z = 0$.

A number of interesting properties have been identified for the FD pulses. A key property is that of space-time non-separability - a property which is not inherent in any of the conventional families of pulses (Gaussian, Bessel etc). In contrast to electromagnetic pulses where the governing equations can be explicitly separated into spatially and temporally dependent components, the spatial and temporal dependencies of an FD pulse are explicitly coupled and cannot be separated. This leads to interesting properties such as a frequency components varying as a function of pulse position.

A further property is that of strong longitudinal field components on axis, at the point where the radial and azimuthal field components are vanishing. Longitudinal fields aligned along the propagation direction of beams and pulses are well known in the optics community and have been utilised for applications such as particle trapping and acceleration. Indeed particle acceleration was amongst the first suggested applications of the FD pulse and the relevant mechanism has been verified in the terahertz regime using TM_{01} pulses. Fig. 1.5(b) shows a schematic from Hellwarth and Nouchi's 1996 paper illustrating a FD pulse co-propagating with an electron and imparting energy to the electron through its longitudinal field components.

Although the FD pulse has existed as an analytic pulse for two decades, there is yet to be a successful experimental realisation of this pulse. The creation of such a pulse is anticipated to be challenging owing to the complex topology, broadband nature and coupling of spatial and temporal components. However, there would be significant benefits to synthesising a FD, with potential applications including sensing, spectroscopy, particle trapping and acceleration, communication, and directed energy transfer. Research conducted in support of this aim shall be reported on in Chapters 5 and 6.

1.3 Thesis overview

This thesis is concerned with demonstrating new manifestations of toroidal excitations, both within matter and metamaterial structures, and propagating through free-space. The research reported on here has lead to the demonstration of a new type of circular dichroism through toroidal excitations, observation of toroidal resonances driven by radially polarised light, excitation of toroidal modes in particulate matter by propagating toroidal excitations, and demonstration of a methodology for synthesis of propagating toroidal excitations. The thesis is structured as follows:

Chapter 2 describes the main experimental and numerical methodology utilised in this thesis. This includes characterisation of metamaterial samples using GHz spectroscopy, and finite element simulation in both the harmonic and transient domains. In addition, this chapter also provides some key theory underpinning toroidal electrodynamics, which will be referred back to through the thesis.

Chapter 3 introduces the concept of toroidal circular dichroism and considers a chiral metamaterial designed to exhibit such an effect. The metamaterial is characterised experimentally and the origin of the observed dichroism is traced numerically to be the result of simultaneous excitation of toroidal dipole and electric quadrupole modes.

Chapter 4 presents radially polarised light as a mechanism to drive toroidal resonances. The design of a scatterer that supports such a toroidal response is shown and is characterised as having a high Q-factor toroidal dipolar response. The response and radiation pattern of the toroidal scatterer is contrasted with a simple electric dipole scatterer.

Chapter 5 gives the history and theory of localised electromagnetic pulses, with particular attention given to the "focused doughnut" pulse. The key properties of the FD pulse are analysed and finite element simulations of the pulse are conducted. The interactions of FD pulses with continuous and particulate matter are studied numerically, with unusual field configurations, and broadband excitation of toroidal modes being observed.

Chapter 6 studies numerically designs of a generator scheme for FD pulses, based on metamaterial arrays of dipole resonators. The evolution of pulses generated from such arrays is evaluated and compared to the analytic form of the FD pulse. The effect of limiting the frequency bandwidth available to the generator scheme is studied, as is the effect of applying a frequency comb methodology to the scheme to generate pulse trains.l

Chapter 7 summarizes the achieved results and proposes the future directions of research.

The Appendix contains technical details omitted from the preceding chapters in order to make the main text easier to follow. The list of publications related to the research reported on in this thesis can be found in Appendix F.

Chapter 2

Methodology

In this chapter, they key research methodologies utilised in this thesis shall be discussed. This includes an in-depth discussion of the multipole expansion, in particular the toroidal multipole family, which is referred to regularly in this body of work as an analytic tool to evaluate systems under electromagnetic excitation. Key experimental techniques and methodologies for numerical simulation of electromagnetic systems are also reported on here.

2.1 Toroidal electrodynamics

In this section, the theoretical framework for the dynamic toroidal multipoles shall be provided. This shall include their appearance in the dynamic multipole expansion alongside the conventional electric and magnetic families, and their implicit inclusion in the Mie expansion. The key properties of the toroidal dipole, including its interaction energy and its radiation pattern, shall also be discussed

2.1.1 Multipole expansion

The multipole expansion provides a useful methodology in electrostatics, magnetostatics, and electrodynamics to calculate the fields and potentials created by arbitrary distributions of charge and current. Conventionally, the expansion is given in terms of electric and magnetic multipole families, with distinct contributions to the fields and potentials [9]. Here the explicit appearance of the additional and distinct toroidal multipole family shall be demonstrated [46, 125].

The Maxwell's equations in CGS units assuming harmonic time dependence of the form $e^{-i\omega t}$ are given by:

$$\nabla \cdot \mathbf{E}\left(\mathbf{r}\right) = 4\pi\rho\left(\mathbf{r}\right), \tag{2.1}$$

$$\nabla \times \mathbf{E}\left(\mathbf{r}\right) = \frac{i\omega}{c}\mathbf{B}, \tag{2.2}$$

$$\nabla \cdot \mathbf{B}(\mathbf{r}) = 0, \tag{2.3}$$

$$\nabla \times \mathbf{B}(\mathbf{r}) = \frac{4\pi}{c}\mathbf{J} + \frac{i\omega}{c}\mathbf{E}. \tag{2.4}$$

By combining Eqs. 2.1 and 2.2 and Eqs. 2.3 and 2.4, and making use of the vector identity $\nabla \times \nabla \times \mathbf{A} = \nabla(\nabla \cdot \mathbf{A}) - \nabla^2\mathbf{A}$, the inhomogeneous wave equations for both the electric E and magnetic B fields can be written as:

$$\left[\nabla^2 + k^2\right]\mathbf{E}(\mathbf{r}) = 4\pi\left[\nabla\rho(\mathbf{r}) - \frac{ik}{c}\mathbf{J}(\mathbf{r})\right], \tag{2.5}$$

$$\left[\nabla^2 + k^2\right]\mathbf{B}(\mathbf{r}) = -\frac{4\pi}{c}\nabla \times \mathbf{J}(\mathbf{r}). \tag{2.6}$$

These can be solved using the Green's function of the Helmholtz equation:

$$\left[\nabla^2 + k^2\right]G\left(\mathbf{r}, \mathbf{r}'\right) = -4\pi\delta\left(\mathbf{r} - \mathbf{r}'\right), \tag{2.7}$$

$$G\left(\mathbf{r}, \mathbf{r}'\right) = \frac{e^{i\mathbf{k}|\mathbf{r}-\mathbf{r}'|}}{|\mathbf{r} - \mathbf{r}'|}. \tag{2.8}$$

Solutions for the electric and magnetic field are then given by integrating over the sources of Eqs. 2.5 and 2.6:

$$\mathbf{E}(\mathbf{r}) = -\int \nabla\rho\left(\mathbf{r}'\right)G\left(\mathbf{r}, \mathbf{r}'\right)d^3r' + \frac{ik}{c}\int \mathbf{J}\left(\mathbf{r}'\right)G\left(\mathbf{r}, \mathbf{r}'\right)dr'^3, \tag{2.9}$$

$$\mathbf{B}(\mathbf{r}) = \int \nabla \times \mathbf{J}\left(\mathbf{r}'\right)G\left(\mathbf{r}, \mathbf{r}'\right)dr'^3. \tag{2.10}$$

The Green's function can then be expanded as a series of spherical vector harmonics:

$$G\left(\mathbf{r}, \mathbf{r}'\right) = 4\pi ik\sum_{l=0}^{\infty}\sum_{m=-l}^{l} j_l\left(kr'\right)h_l(kr)Y_{l,m}(\theta, \phi)\,Y^*_{l,m}\left(\theta', \phi'\right), \tag{2.11}$$

Where $j_l(kr)$ and $h_l(kr)$ are the spherical Bessel and Hankel functions respectively, and $Y_{l,m}$ represents the spherical vector harmonics, with P_l^m as the associated Legendre polynomials:

$$Y_{l,m}(\theta, \phi) = \sqrt{\frac{(2l+1)(l-m)!}{4\pi(l+m)!}}P_l^m(cos\theta)\,e^{im\phi}, \tag{2.12}$$

$$P_l^m(\alpha) = \frac{(-1)^m}{2^l l!}\left(1-\alpha^2\right)^{m/2}\frac{d^{l+m}}{d\alpha^{l+m}}\left(\alpha^2-1\right)^l. \tag{2.13}$$

Substitution of the expanded Green's function [Eq. 2.11] into Eqs. 2.9 and 2.10 gives:

$$\mathbf{E}\left(\mathbf{r}\right) = \frac{4\pi k^2}{c}\sum_{l,m}\left[E_{l,m}\mathbf{\Psi}_{l,m} + M_{l,m}\mathbf{\Phi}_{l,m}\right], \tag{2.14}$$

$$\mathbf{B}\left(\mathbf{r}\right) = \frac{4\pi k^2}{c}\sum_{l,m}\left[E_{l,m}\mathbf{\Phi}_{l,m} - M_{l,m}\mathbf{\Psi}_{l,m}\right], \tag{2.15}$$

Where $\mathbf{\Phi}_{l,m}$ and $\mathbf{\Psi}_{l,m}$ represent vector spherical wave harmonics:

$$\mathbf{\Phi}_{l,m} = \mathbf{L}h_l\left(kr\right)Y_{l,m}\left(\theta,\phi\right), \tag{2.16}$$

$$\mathbf{\Psi}_{l,m} = \frac{i}{k}\nabla\times\mathbf{\Phi}_{l,m}, \tag{2.17}$$

Where the angular momentum operator $\mathbf{L} = -i\mathbf{r}\times\nabla$. The coefficients $E_{l,m}$ and $M_{l,m}$ are known as the dynamic electric and magnetic multipole moments and are defined as:

$$E_{l,m} = -\frac{i}{l\left(l+1\right)}\int j_l\left(kr'\right)Y^*_{l,m}\left(\theta',\phi'\right)\left[ik\mathbf{r}'\cdot\mathbf{J}\left(\mathbf{r}'\right) - c\left(2+\mathbf{r}'\cdot\nabla'\right)\rho\left(\mathbf{r}'\right)\right]dr'^3, \tag{2.18}$$

$$M_{l,m} = \frac{i}{l\left(l+1\right)}\int j_l\left(kr'\right)Y^*_{l,m}\left(\theta',\phi'\right)\left[\mathbf{r}'\cdot\nabla\times\mathbf{J}\left(\mathbf{r}'\right)\right]dr'^3. \tag{2.19}$$

The electric multipole coefficient can be split into two distinct terms: $Q_{l,m}$ and $T_{l,m}$:

$$E_{l,m} = Q_{l,m} + T_{l,m}, \tag{2.20}$$

$$Q_{l,m} = \frac{i}{l\left(l+1\right)}\int j_l\left(kr'\right)Y^*_{l,m}\left(\theta',\phi'\right)\left[c\left(2+\mathbf{r}'\cdot\nabla'\right)\rho\left(\mathbf{r}'\right)\right]dr'^3, \tag{2.21}$$

$$T_{l,m} = \frac{k}{l\left(l+1\right)}\int j_l\left(kr'\right)Y^*_{l,m}\left(\theta',\phi'\right)\left[\mathbf{r}'\cdot\mathbf{J}\left(\mathbf{r}'\right)\right]dr'^3. \tag{2.22}$$

This results in three multipole families - electric $Q_{l,m}$, magnetic $M_{l,m}$, and toroidal $T_{l,m}$ - that represent three distinct types of volumetric oscillations. The electric multipoles are dependent on charge oscillations. The magnetic multipoles are dependent on transverse current oscillations ($\mathbf{r}\times\mathbf{J}\neq 0$). The toroidal multipoles are dependent on radial current oscillations ($\mathbf{r}\cdot\mathbf{J}\neq 0$). Together these three multipole families provide a complete description of the scattered electric and magnetic fields of an arbitrary-charge current distribution:

$$\mathbf{E}\left(\mathbf{r}\right) = \frac{4\pi k^2}{c}\sum_{l,m}\left[Q_{l,m}\mathbf{\Psi}_{l,m} + M_{l,m}\mathbf{\Phi}_{l,m} + T_{l,m}\mathbf{\Psi}_{l,m}\right], \tag{2.23}$$

$$\mathbf{B}\left(\mathbf{r}\right) = \frac{4\pi k^2}{c}\sum_{l,m}\left[Q_{l,m}\mathbf{\Phi}_{l,m} - M_{l,m}\mathbf{\Psi}_{l,m} + T_{l,m}\mathbf{\Phi}_{l,m}\right]. \tag{2.24}$$

Though in general, all three multipole families are required to form a complete description of an arbitrary charge-current distribution, the toroidal multipole family $T_{l,m}$ is usually neglected in conventional descriptions of the multipole expansion. This can be attributed to the extra k-dependence in the definition of the $T_{l,m}$ coefficient. As such, in the long-wavelength limit, the toroidal terms are frequently omitted. This also reflects the fact that $T_{l,m}$ is dependent on oscillating radial currents of the form ($\mathbf{r} \cdot \mathbf{J} \neq 0$). To excite such currents necessarily requires an electrically large source beyond the long wavelength limit.

2.1.2 Toroidal multipoles in Mie theory

In Mie theory, in contrast to multipole theory, the spherical vector harmonic expansion is applied to scattered $\mathbf{E}_{sca}$, incident $\mathbf{E}_{inc}$, and internal (with respect to the scatterer) $\mathbf{E}_{int}$ fields. The expansion coefficients for the internal and scattered fields (Mie coefficients) are determined by enforcing the continuity of the fields across the scatterer's boundary. These boundary conditions are only respected for the transverse E and H field components:

$$(\mathbf{E}_{inc} + \mathbf{E}_{sca} - \mathbf{E}_{int}) \times \mathbf{r} = 0, \tag{2.25}$$

$$(\mathbf{H}_{inc} + \mathbf{H}_{sca} - \mathbf{H}_{int}) \times \mathbf{r} = 0. \tag{2.26}$$

This is due to the radial components of the scattered field vanishing in the far-field. Consequently, the Mie expansion of the scattered field possesses only two families of Mie scattering coefficients $a_{l,m}$ and $b_{l,m}$:

$$\mathbf{E}_{sca} = k^2 \sum_{l,m} \left(A_{l,m} a_{l,m} \mathbf{\Psi}_{l,m} + B_{l,m} b_{l,m} \mathbf{\Phi}_{l,m} \right), \tag{2.27}$$

Where $A_{l,m}$ and $B_{l,m}$ are the expansion coefficients for the incident field. Unlike the multipole expansion coefficients, $a_{l,m}$ and $b_{l,m}$ are not directly related to a particular charge current excitation, but instead are related to the shape of the scatterer and spatial structure of the scattered fields. Furthermore, there is no explicit term corresponding to a toroidal multipole family.

This can be understood to be the result of two factors. Firstly, the electric and toroidal multipole families radiate identically in the far-field. Secondly, their differences in near-field (due to non-vanishing radial field components) is not recognised by the imposed Mie boundary conditions. Consequently, the scattered field contributions from the electric and toroidal multipoles are mixed together in the $a_{l,m}$ coefficient and cannot be separated without exact knowledge of the charge current distribution.

2.1.3 Properties of the toroidal multipoles

It is instructive to begin our discussion in terms of the lowest order term of the toroidal multipoles - the toroidal dipole. Schematically, the ideal toroidal dipole consists of poloidal currents flowing on the surface of a torus. The poloidal currents enclose a loop of magnetic field that exists only within the confines of the torus. The resultant toroidal dipole is then orientated along the axis of the torus. In the same way that a dynamic magnetic dipole can be thought of as a closed loop of electric dipoles arranged head-to-tail, the toroidal dipole can be though of as a closed loop of magnetic dipoles orientated head-to-tail [Fig. 2.1].

There are several definitions of toroidal dipoles that are instructive to examine. The simplest definition of a macroscopic toroidal dipole consists of a wire solenoid bent into a closed loop, whereby the magnetic field is purely confined within the solenoid loop. Under this description, the macroscopic toroidal dipole can be defined as [19]:

$$T = \frac{I\pi d R^2}{2c} = \frac{IV}{4\pi c}, \tag{2.28}$$

Where I is the total poloidal current on the surface of the torus, and V is the total volume of the torus. In the frame of the multipole expansion, a definition of the toroidal dipole of an arbitrary charge-current distribution can be obtained through an expansion of the current density of a source and considering the radial currents of the form $\mathbf{r} \cdot \mathbf{J} \neq 0$ [19]. This yields the toroidal dipole $\mathbf{T}$ as [19,43,44]:

$$\mathbf{T} = \frac{1}{10c} \int \left[(\mathbf{r} \cdot \mathbf{j})\, \mathbf{r} - 2r^2 \mathbf{J} \right] d^3 r, \tag{2.29}$$

Where $\mathbf{r}$ is the general spherical coordinate. It can be shown that upon substituting the current definitions corresponding to electric and magnetic dipoles (see Appendix A) into Eq. 2.29, the resultant toroidal dipole shall be identically 0 [19]. However, substitution of the ideal point-like toroidal current distribution [16,19,42]:

$$\mathbf{J}(t, \mathbf{r}) = \nabla \times \nabla \times \left(c\mathbf{T}(t) \delta^{(3)}(\mathbf{r}) \right), \tag{2.30}$$

Shall lead to a non-zero toroidal moment.

Beyond the toroidal dipole, the toroidal multipoles expand to higher order terms in the same manner as the electric and magnetic multipoles, with the expressions for toroidal quadrupoles and octupoles given in Sec. 2.2.1. Toroidal quadrupoles (octupoles, etc) radiate in the same manner as electric quadrupoles (octupoles, etc). We note that a material where a toroidal multipole of higher order than dipole makes a significant contribution to the electromagnetic response has not yet been engineered.

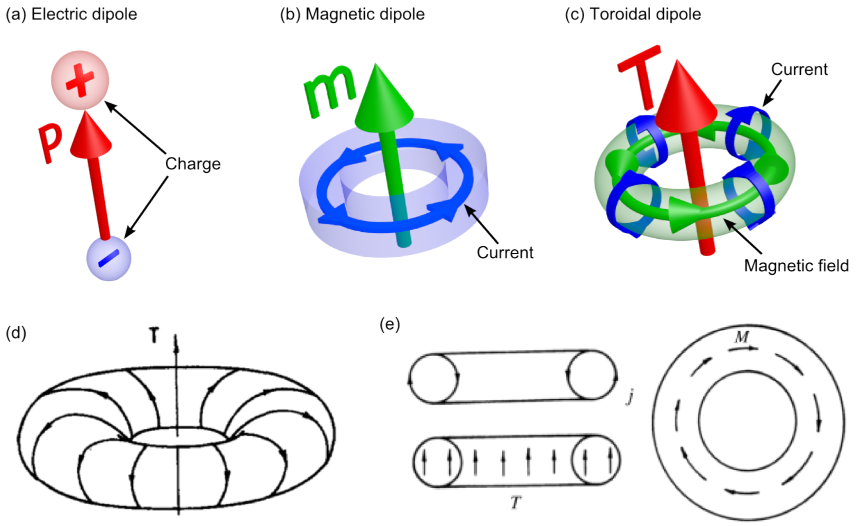

Figure 2.1: ***Toroidal multipoles in context.*** *(a)-(c) show artistic schematics of the lowest order excitations of each of the microscopic multipole families: (a) electric dipole* **p**, *(b) magnetic* **m**, *and (c) toroidal dipole* **T**. *The charge-current topology of each excitation is clearly indicated. (d) and (e) give some historical illustrations of the toroidal dipole provided in some of the early works on dynamic toroidal excitations, adapted from Refs. [19] and [16] respectively.*

Interaction energy

It can be shown that the toroidal dipole **T** interacts directly only with external currents **J** and the time derivative of the electric field $\partial\mathbf{E}/\partial t$ through evaluating the expression for its energy of interaction with electromagnetic fields W_T [19, 43]:

$$W_T = -\mathbf{T} \cdot \left[\frac{4\pi}{c}\mathbf{J} + \frac{1}{c}\frac{\partial \mathbf{E}}{\partial t}\right]. \tag{2.31}$$

This is equivalent to interaction with a vortex of magnetic field i.e $\nabla \times \mathbf{B}$. It can be noted that in the static case ($\partial\mathbf{E}/\partial t$=0), the toroidal dipole interacts only with currents and tends to align parallel to the current flow. It is noted that the interaction of the toroidal dipole with the time derivative of the E field will be suppressed for low frequency excitations, and has been suggested as a paradigm for engineering toroidal qubits that are protected from low-frequency noise [123].

We can contrast this with the interaction energy for electric **p** and magnetic **m** dipoles.

$$W_p = -\mathbf{p} \cdot \mathbf{E} - \frac{1}{c}\frac{\partial}{\partial t}(\mathbf{p} \cdot \mathbf{A}), \tag{2.32}$$

$$W_m = -\mathbf{m} \cdot \mathbf{B}. \tag{2.33}$$

From these, it can be seen that an electric dipole will interact with the electric field **E** and vector potential **A**. A magnetic dipole will interact with the magnetic field **B**.

The distinction here is clear: whilst the electric and magnetic dipoles interact directly with fields, the toroidal dipole interacts with currents and the temporal gradient of the E-field. A full derivation of all interaction energy expressions is given in Appendix A.

Radiation patterns

It is important to discuss the radiation properties of the toroidal multipoles. Although the toroidal multipoles represent distinct charge-current excitation from the electric multipoles, it is found that they emit radiation with identical angular momentum and parity properties [42,46]. This was highlighted in Section 2.1.1 for the general multipole expansion and is emphasised below in the expressions for the far-field electric field of the electric $\mathbf{p}$ and toroidal $\mathbf{T}$ dipoles:

$$\mathbf{E}_p(\mathbf{r}) = \frac{k^2 c}{4\pi}\sqrt{\frac{\mu_0}{\epsilon_0}}\left(\frac{e^{ikr}}{r}\right)(\hat{\mathbf{r}} \times \mathbf{p}) \times \hat{\mathbf{r}}, \tag{2.34}$$

$$\mathbf{E}_T(\mathbf{r}) = \frac{ik^3 c}{4\pi}\sqrt{\frac{\mu_0}{\epsilon_0}}\left(\frac{e^{ikr}}{r}\right)(\hat{\mathbf{r}} \times \mathbf{T}) \times \hat{\mathbf{r}}. \tag{2.35}$$

It can be seen that the only distinction between the two expressions is an extra factor of ik in the toroidal dipole field, which represents an additional phase difference and frequency dependence. This was also emphasised in Section 2.1.1. A full derivation of these expressions can be found in Appendix B. This implies that although the toroidal dipole could not be distinguished from the electric dipole by observing the far-field radiation pattern alone, they could be distinguished by their frequency dependence using a spectroscopic analysis [44, 46]. This shall be particularly relevant in Chapter 4.

Interestingly, although they exhibit identical radiation patterns, the vector potentials from an electric and a toroidal dipole are non-identical and the difference $\Delta\mathbf{A} = \mathbf{A}_T - \mathbf{A}_p$ cannot be removed through a gauge transformation [42]. This forms the basis for the intriguing charge-current distribution known as a non-radiating configuration, or dynamic anapole [42, 113, 126]. From the above expressions, it can be seen that co-located electric and toroidal dipoles with an appropriate phase difference will radiate fields that will destructively interfere in the far-field, whilst still maintaining a non-vanishing vector potential. Such a source of propagating electromagnetic potential has been suggested as a new channel for information transfer in time-dependent Aharonov-Bohm-like experiments, though this remains a controversial topic [127].

2.2 Multipole analysis of electromagnetic scattering

With the toroidal dipole identified as a potentially interesting and exploitable excitation for this work, it is necessary to be able to identify its presence amongst the excited current modes of a material, as well its relative intensity and other modes it may be coupling to. Though the concept of evaluating metamaterials in terms of their excited multipole modes is not a new one [128–131], only recently has the toroidal multipole family been considered in such calculations. A commercially available Maxwell's equation solver (COMSOL 3.5a) is used to model metamaterials and using methods established in Ref. [44] and [52], the dominant current modes in the material can be determined and the material's far field radiation response can be calculated.

2.2.1 Multipoles from simulated current distributions

The multipole moments of the metamaterial system were calculated with a numerical Maxwell's equations solver (COMSOL 3.5a) by integrating the current densities across the metamaterial unit cells. This was performed according to the integral representations of multipoles below [7, 44, 45]. These expressions can be obtained (with some algebraic effort) in Cartesian coordinates from the multipole expansion given in Section 2.1.1:

Dipole order - electric $\mathbf{p}$, magnetic $\mathbf{m}$, toroidal $\mathbf{T}$, and the mean-square radius of the magnetic dipole distribution $\langle \boldsymbol{R_m^2} \rangle$:

$$\mathbf{p} = \frac{1}{i\omega}\int d^3r\mathbf{J}, \tag{2.36}$$

$$\mathbf{m} = \frac{1}{2c}\int d^3r\left(\mathbf{r}\times\mathbf{J}\right), \tag{2.37}$$

$$\mathbf{T} = \frac{1}{10c}\int d^3r\left[\left(\mathbf{r}\cdot\mathbf{J}\right)\mathbf{r} - 2r^2\mathbf{J}\right], \tag{2.38}$$

$$\langle \boldsymbol{R_m^2} \rangle = \frac{1}{2c}\int d^3r\left(\mathbf{r}\times\mathbf{J}\right)r^2. \tag{2.39}$$

Quadrupole order - electric $Q_{\alpha\beta}$, magnetic $M_{\alpha\beta}$, and toroidal $T_{\alpha\beta}$:

$$Q_{\alpha\beta} = \frac{1}{2i\omega}\int d^3r\left[r_\alpha J_\beta + r_\beta J_\alpha - \frac{2}{3}\delta_{\alpha\beta}\left(\mathbf{r}\cdot\mathbf{J}\right)\right], \tag{2.40}$$

$$M_{\alpha\beta} = \frac{1}{3c}\int d^3r\left[\left(\mathbf{r}\times\mathbf{J}\right)_\alpha r_\beta + \left(\mathbf{r}\times\mathbf{J}\right)_\beta r_\alpha\right], \tag{2.41}$$

$$T_{\alpha\beta} = \frac{1}{28c}\int d^3r\left[4r_\alpha r_\beta\left(\mathbf{r}\cdot\mathbf{J}\right) - 5r^2\left(r_\alpha J_\beta + r_\beta J_\alpha\right) + 2r^2\left(\mathbf{r}\cdot\mathbf{j}\right)\delta_{\alpha\beta}\right]. \tag{2.42}$$

Octupole order - electric $Q_{\alpha\beta\gamma}$ and magnetic $M_{\alpha\beta\gamma}$:

$$\begin{aligned}Q_{\alpha\beta\gamma} =& \frac{1}{6i\omega}\int d^3r\left[J_\alpha\left(r_\beta r_\gamma - \frac{r^2}{5}\delta_{\beta\gamma}\right) + r_\alpha\left(J_\beta r_\gamma + r_\beta J_\gamma - \frac{2}{5}\left(\mathbf{r}\cdot\mathbf{J}\right)\right)\right] + \cdots \\ & \cdots + \{\alpha \leftrightarrow \beta, \gamma\} + \{\alpha \leftrightarrow \gamma, \beta\},\end{aligned} \tag{2.43}$$

$$M_{\alpha\beta\gamma} = \frac{15}{2c}\int d^3r\left(r_\alpha r_\beta - \frac{r^2}{5}\delta_{\alpha\beta}\right)\cdot\left[\mathbf{r}\times\mathbf{J}\right]_\gamma + \{\alpha \leftrightarrow \beta, \gamma\} + \{\alpha \leftrightarrow \gamma, \beta\}. \tag{2.44}$$

Where $\rho(\mathbf{r})$ is the charge density, $\mathbf{J}$ is the current density, and $\delta_{\alpha\beta}$ is the Kronecker delta function. We note that in some cases charge density has been replaced with current density using the continuity relation: $\nabla\cdot\mathbf{J} = -\partial\rho/\partial t$. In the octupole terms, a shorthand has been used to improve clarity. For example, $\{\alpha \leftrightarrow \beta, \gamma\}$ indicates that this term of the equation can be obtained by exchanging the α and β indicies of the first given term.

Higher order terms have not been given here as the metamolecules being considered in this work are not optimised to excite multipoles of higher order than the electric quadrupole. As such, no multipole modes greater than octupole order are calculated.

2.2.2 Scattering intensity of multipoles

The intensity radiated through a sphere surrounding the metamolecule by these multipoles can then be calculated from the above multipole definitions. Note that this is not an expansion, but merely a summation of the intensity terms derived from the multipoles given above. Further, the equation is given in CGS units, rendering the speed of light c dimensionless.

$$\begin{aligned}I = \frac{2\omega^4}{3c^3}\left|\mathbf{p}\right|^2 + \frac{2\omega^4}{3c^3}\left|\mathbf{m}\right|^2 + \frac{4\omega^5}{3c^4}\mathrm{Im}\left(\mathbf{p}^\dagger\cdot\mathbf{T}\right) + \frac{2\omega^6}{3c^5}\left|\mathbf{T}\right|^2 + \ldots \\ \ldots + \frac{\omega^6}{5c^5}Q_{\alpha\beta}Q_{\alpha\beta} + \frac{\omega^6}{20c^5}M_{\alpha\beta}M_{\alpha\beta} + \frac{2\omega^6}{15c^5}\mathrm{Re}\left(\mathbf{M}^\dagger\cdot\left\langle\mathbf{R^2_m}\right\rangle\right)\end{aligned} \tag{2.45}$$

The electric and magnetic octupole, and toroidal quadrupole terms have been omitted for brevity. Along with the expected radiation intensity terms characterised by the square of the respective multipoles, there also exist terms corresponding to interference effects [7, 44, 113]. The third term arises due to interference between the conventional electric dipole $\mathbf{p}$ and toroidal dipole $\mathbf{T}$, which is generally non-zero. The seventh term arises due to interference between the conventional magnetic dipole $\mathbf{m}$ and the first-order mean-square radius of the magnetic dipole distribution $\left\langle\mathbf{R^2_m}\right\rangle$. Higher order interference terms were neglected in calculations. It can be noted that the non-radiating configuration mentioned in Section 2.1.3, can be inferred from this prescription for scattered intensity, whereby the electric/toroidal dipole interference term

$\frac{4\omega^5}{3c^4}\mathrm{Im}\left(\mathbf{p}^\dagger \cdot \mathbf{t}\right)$ effectively cancels the individual electric and toroidal dipole intensity terms [113].

2.3 GHz spectroscopy

For the study of microwave metamaterials in this thesis, we utilise an anechoic chamber equipped with linearly-polarised horn antenna (Schwarzbeck BBHA 9120D) and a *vector network analyser* (VNA) (Agilent E8364B), which allows for simultaneous measurement of amplitude and phase of microwave radiation in the 1-18GHz range. This apparatus allowed for full characterisation of the reflection, transmission and polarisation response of a metamaterial sample. A photograph of the anechoic chamber and a schematic of the experimental setup are shown in Fig. 2.2. The antenna were equipped with collimating lenses to focus the emitted microwaves and ensure maximum power is focused on the sample. The antennae could be rotated to take measurements of arbitrary polarisations. The metamaterial under interrogation was supported by a wooden stand with an aperture to block rogue microwave radiation.

2.3.1 Vector network analyser

The VNA used for our experiments (Agilent E8364B) constitutes a two port network, with each port able to emit and receive electromagnetic radiation over a range of frequencies. A full characterisation of a metamaterial sample requires two measurements at each frequency - one using emission from port 1, and one using emission from port 2. The quantities that are measured by the VNA are complex amplitude (intensity and phase) of: the radiation emitted by port 1 (a_1), radiation emitted by port 2 (a_2), radiation received by port 1 (b_1), and radiation received by port 2 (b_2). The scattering matrix S can be used to relate these four quantities:

$$\begin{bmatrix} b_1 \\ b_2 \end{bmatrix} = \begin{bmatrix} S_{11} & S_{12} \\ S_{21} & S_{22} \end{bmatrix} \begin{bmatrix} a_1 \\ a_2 \end{bmatrix}, \tag{2.46}$$

Where components of S_{ij} are known as S-parameters and can be computed from the measured quantities in the following manner:

$$S_{11} = \frac{b_1}{a_1}, \text{ provided } a_2 = 0 \qquad S_{12} = \frac{b_1}{a_2}, \text{ provided } a_1 = 0$$

$$S_{21} = \frac{b_2}{a_1}, \text{ provided } a_2 = 0 \qquad S_{22} = \frac{b_2}{a_2}, \text{ provided } a_1 = 0$$

As such, it can be seen that S_{11} and S_{22} represent reflection from the metamaterial sample when it is illuminated from port 1 and 2 respectively. Similarly, S_{21} and S_{12} represent transmission through the metamaterial sample from port 1 → port 2 and

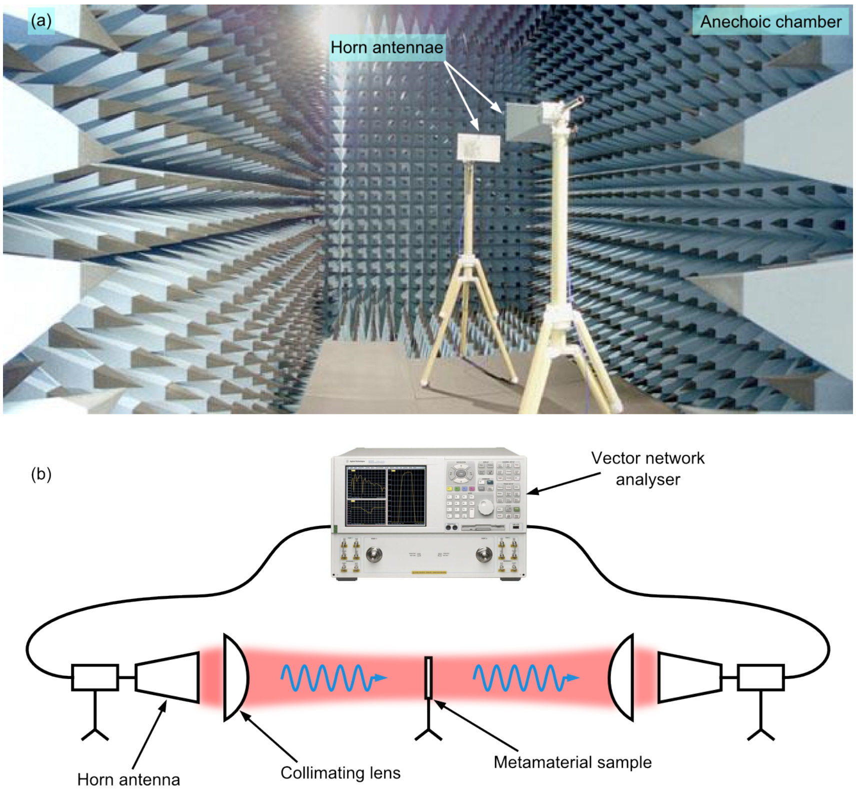

Figure 2.2: ***Experimental setup for GHz spectroscopy.*** *This figure shows the experimental setup used to analyse metamaterials in the microwave regime. (a) shows the anechoic chamber with microwave absorbing walls. The linearly polarised horn antenna are placed on wooden stands in the center of the chamber. (b) shows the schematic for a transmission measurement of a metamaterial sample. Linearly polarised radiation is generated by the horn antennae and collimated by dielectric lenses. The metamaterial under investigation is located equidistant between the two antennae.The emitted and received signals are analysed by the vector network analyser.*

port 2 → port 1 respectively. Given that the metamaterial samples used in this study are identical under 180^o rotation, the parameters $S_{11} = S_{22}$ and $S_{21} = S_{12}$, with any discrepancies arising due to misalignments and asymmetries in the experimental setup. Additionally, reflection measurements were not necessary for the experiments reported on in this thesis, and so we are concerned only with the S_{12} and S_{21} parameters.

2.3.2 Calibration

Prior to taking experimental data of a metamaterial sample, it is necessary to calibrate the VNA setup. In principle, the VNA should only measure the electromagnetic response of the metamaterial sample under interrogation. However, for a realistic experimental setup, the signal has to travel through multiple components e.g. connecting cables, waveguiding elements; before and after interaction with the metamaterial sample, thus leading to a combined response being measured by the VNA. Calibration is therefore required to isolate the electromagnetic response of the metamaterial sample from that of the other components in the setup.

This achieved using a two-port error correction process, that is built in as part of the VNA software. This procedure is based on measurement of reference samples and allows the VNA to remove systematic errors associated with parts of the setup from the final spectroscopic data. The reference cases utilised for our calibration procedures were a free-space S-parameter measurement, and a measurement using reflective plates of identical thickness to the metamaterial sample under investigation.

2.3.3 Gating of spectroscopic data

In addition to the antennae measuring reflected and transmitted signals from the metamaterial sample, the antenna will also detect spurious higher-order reflections between the antennae and the metamaterial, and reflections between the two antennae. These extra signals manifest as high frequency oscillations in the measured reflection and transmission spectra in the frequency domain.

This noise can be removed using the built-in gating functions of the VNA. This process involves Fourier transforming the spectra into the time domain and suppressing the echoes that arrive after the primary pulse. This done by introducing a maximum cut-off time for the data before Fourier transforming back to the frequency domain, resulting in significantly improved spectra.

2.4 Numerical modelling

This section briefly describes the method used to simulate the light-matter interactions reported on in this thesis. Interactions were simulated by solving the 3D Maxwell's equations using the *Finite Element Method* (FEM) [132]. The commercially available FEM software COMSOL 3.5a was utilised for this. Both harmonic and transient simulation modes were used, with the harmonic domain being used primarily for simulations of metamaterial structures under illumination by plane waves, whilst the simulated domain was used to study the propagation and interactions of electromagnetic pulses.

2.4.1 Simulations in the frequency domain

Simulations in the harmonic domain broadly consisted of simulating the response of metamaterial structures to incident electromagnetic radiation over a specified frequency range. A typical example of the geometry utilised for this is shown in Fig. 2.3. The geometry consists of an individual metamaterial unit cell located at the center of a tunnel of free-space in the z direction. The model is simplified by assuming the

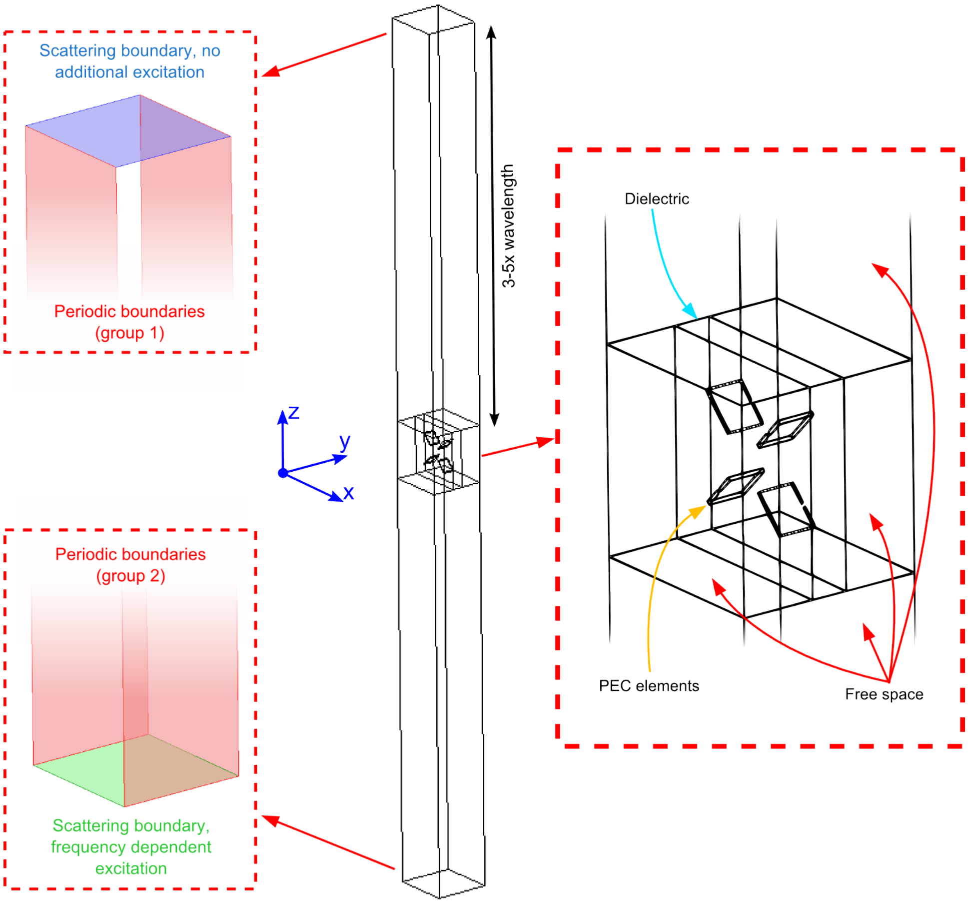

Figure 2.3: ***Numerical modeling in the frequency domain.*** *This figure shows a typical geometry in COMSOL 3.5a used to simulate the electromagnetic response of a metamaterial array. The size of the metamaterial array was assumed to be infinite in the x and y directions, and so a single unit cell with periodic boundary conditions could be simulated. The metamaterial unit cell was located in the center of a long free-space domain. Scattering boundaries at each end of the domain were used to generate plane wave incident light, and to simulate radiation scattering into free-space.*

metamaterial extends infinitely in the x and y directions, and the x and y boundaries are modeled as periodic boundaries to reflect this. It is noted that there are important distinctions between infinite and finite planar arrays in terms of electromagnetic scattering, principally the absence of edge effects and the cancellation via destructive interference of radiation components not parallel to the incident field. This can lead to discrepencies between simulated and experimental scattering results and shoould be accounted for during analysis.

At each end of the free-space tunnel, the boundaries are assigned as scattering boundaries which fulfil two functions. Firstly, electromagnetic waves representing incident radiation can be launched from the scattering boundary. Secondly, scattering boundaries allow incident radiation to pass through without reflection, simulating scattering into free-space. By integrating the Poynting vector over the scattering boundaries, the transmission and reflection of the metamaterial can be determined. The length of the free-space tunnel either side of the metamaterial is necessarily in the 3-5 wavelengths range. This ensures that they only interact with far-field radiation from the metamaterial. Different materials were modeled either through use of a complex-valued dielectric constant, or use of *perfect electrical conductor* (PEC) boundaries, which are good approximations to metals in the microwave regime.

Verification of simulation results could be achieved by one of two methods - comparison with experimental results, and by changing the number of finite elements in the model. In the latter case, if by increasing the number of finite elements did not change the results of the simulation, it could be concluded that the simulation was valid.

2.4.2 Obtaining macroscopic properties from multipole response

When simulating metamaterial structures, evaluating the multipoles excited in a metamaterial can give an excellent insight into the underlying cause of the metamaterial's macroscopic properties. However, in cases where the overall multipole response is complex, it can be difficult to directly trace resonant features to specific multipole excitations. An example of such a system will be given in Chapter 3, where the resonant circular dichroism features in the metamaterial transmission spectrum are attributed to pairs of multipoles. As such, it is beneficial to have a methodology that can directly relate the macroscopic properties of a metamaterial to the microscopic multipoles excited within its metamolecules.

Such a methodology has been provided by V. Savinov et al [52]. It follows broadly the procedure outlined below:

1. **Simulate metamaterial structure using the COMSOL simulation package.**

    Approximate a realistic metamaterial by simulating an infinite array i.e. simulate a single metamaterial unit cell with periodic boundary conditions under plane wave excitation at normal incidence, as described in Section 2.4.1. Simulation of an infinite array necessarily accounts for inter-metamolecule interactions in the metamaterial.

2. **Calculate the microscopic multipole response of a single unit cell using the formulae in Section 2.2.1.**

3. **Calculate the radiation of the individual multipole components of the unit cell excitation.**

4. **Sum contributions of whole array at the position of the observer to obtain the macroscopic, far-field properties of the metamaterial structure.**

The total field radiated by an infinitely large planar array of an arbitrary multipole is obtained by summing the contributions from all unit cells at the position of the observer:

$$\mathbf{E}_{scattered} = \sum_{\mathbf{r}} \mathbf{E}\left(\mathbf{r}\right) \approx \frac{1}{\Delta^2} \int d^2 r \mathbf{E}\left(\mathbf{r}\right), \tag{2.47}$$

Where Δ^2 is the unit cell area. Note that certain radiation components will not contribute to the far-field radiation of the metamaterial, for example radiation in the plane of the metamaterial. The reflected $\mathbf{E}_{reflected}$ and transmitted $\mathbf{E}_{transmitted}$ fields of this array will be given by:

$$\mathbf{E}_{reflected} = \left[\mathbf{E}_{scattered}\right]_{\hat{\mathbf{n}}=-\hat{\mathbf{k}}}, \tag{2.48}$$

$$\mathbf{E}_{transmitted} = \left[\mathbf{E}_{scattered}\right]_{\hat{\mathbf{n}}=\hat{\mathbf{k}}} + \mathbf{E}_{incident}. \tag{2.49}$$

This procedure yields a set of reflected and transmitted fields attributed to the microscopic multipoles excited in the metamaterial. The sum of these multipole radiation components gives the total radiation of the array, which can then be compared to the incident plane wave to give the macroscopic reflection (r, R) transmission (t, T) coefficients.

The benefit of this methodology is that by inclusion or exclusion of the radiating components of different multipoles, their contribution to the macroscopic properties of a metamaterial can be explicitly quantified. An example of such a procedure shall be given in Chapter 3.

2.4.3 Simulations in the time domain

Simulations in the transient domain were conducted to examine the propagation dynamics and interactions of electromagnetic pulses. A typical example of the geometry utilised for this is shown in Fig. 2.4. The geometry consists of cylindrical free-space domain with an arbitrary scatter located in the center. The boundaries of the cylinder are assigned to be scattering boundaries, which as previously mentioned, allows for simulation of an incident electromagnetic excitation and for radiation to pass through without reflection. The excitation of a scattering boundary is is chosen as a time dependent electric field $\mathbf{E}(t)$. The size of the cylindrical domain is chosen such that the full width of the pulse is confined within the cylinder, and that it will propagate over a distance of several effective wavelengths before exiting the domain. The width of the domain, and the well-collimated nature of the simulated pulses over the domain length, means the simulation can be conducted without the use of perfectly matched layers [133]. As in the harmonic case, different materials are simulated by use

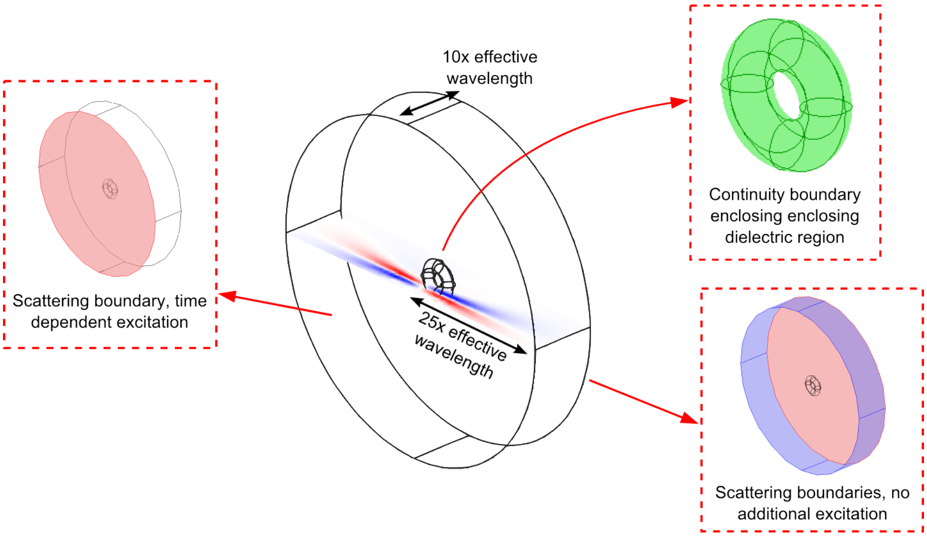

Figure 2.4: ***Numerical modeling in the time domain.*** *This figure shows a typical geometry in COMSOL 3.5a used to simulate time-dependent electromagnetic interactions. A scatterer is located at the center of a cylindrical domain. The domain is bordered by scattering boundaries which allows for generation of the time dependent excitation, and absorption of scattered fields.*

of a complex valued dielectric. Transient simulation precludes the use of a frequency-dependent dielectric constant, and so all simulations in the transient domain assumed non-dispersive media.

As in the case of harmonic simulations, the spatial meshing considerations are relevant to ensuring the accuracy of the simulation. However as the simulation is in the time domain, where the solution at the current time is dependent on the solution at previous times, the step size in the time domain is also important to ensure stability of the solutions [134]. Furthermore, an important consideration in the case of transient excitation is the size of the spatial finite elements relative to the step length in the time domain. Time steps were generally taken to be $t_{step} = \frac{1}{10}\left(\lambda_{eff}/c\right)$. Spatial steps were accordingly matched to this, with a size of $\approx \lambda_{eff}/10$, where λ_{eff} represents the effective wavelength of the transient excitation.

Chapter 3

Toroidal circular dichroism

3.1 Introduction

Chirality, i.e., the property by which an object cannot be superimposed with its mirror image [135], is a basic characteristic of matter at all scales from the cosmological to the molecular. It enters fundamental questions, such as the homochirality observed in life [136] and the parity violation within the standard model of physics [137, 138]. A ubiquitous manifestation of chirality is optical activity, which consists of two important electromagnetic phenomena: circular birefringence and circular dichroism. These are defined as:

Circular birefringence

- Real part of the refractive index of a medium is dependent on the handedness of incident circularly polarised light.
- Ability to rotate the plane of polarisation of incident electromagnetic waves.

Circular dichroism

- imaginary part of the refractive index of a medium i.e. the absorption coefficient, is dependent on the handedness of incident circularly polarised light.
- Ability to change the polarisation ellipticity of incident electromagnetic waves.

Observed more than 150 years ago by Pasteur on solutions of tartaric acid [139], optical activity occupies a central position in the diagnostic methodology of many scientific disciplines [140] where it provides the means for obtaining information about the microscopic structure and electromagnetic excitations of a medium from its far-field scattering properties. An examination of optical activity is invaluable, for example, in the biosciences where it enables deduction of the conformation of proteins in a dynamic fashion [141] or in the study of magnetic phenomena in strongly correlated electronic systems [142].

Optical activity is typically described within the dipole approximation of the dynamic

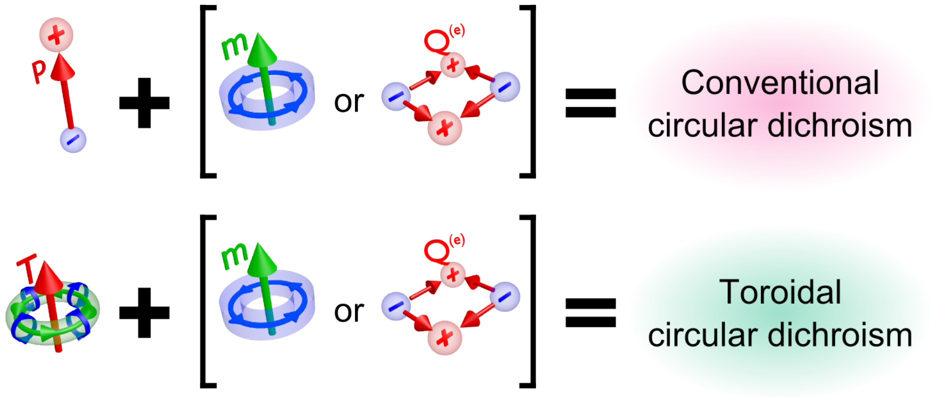

Figure 3.1: ***Multipole mechanisms for conventional and toroidal circular dichroism.*** *This figure illustrates the microscopic multipole mechanisms that result in the macroscopic phenomenon of circular dichroism. Conventional circular dichroism is understood to be caused by simultaneous excitation of electric p and magnetic m dipoles. In some cases, the electric quadrupole Q_e can replace the magnetic dipole in this mechanism. In the case of toroidal circular dichroism however, the toroidal dipole T assumes the role of the electric dipole.*

multipole expansion [6] where the interaction of an incident wave with induced collinear electric and magnetic dipoles affects the polarization state of the wave upon transmission. Indeed the conventional expression for the rotary power R of a medium (an indicator of optical activity) is dependent only on electric $\mathbf{p}$ and magnetic $\mathbf{m}$ dipole operators [143]:

$$R_{n,k} = \mathrm{Im}\left[\langle\psi_k\left|\mathbf{p}\right|\psi_n\rangle\langle\psi_n\left|\mathbf{m}\right|\psi_k\rangle\right], \tag{3.1}$$

Where ψ_k and ψ_n represent states of the electric and magnetic moments of a molecule. This expression is obtained using perturbation theory under the common (in chemical sciences) assumption that the size of a molecule is much smaller that the wavelength of light (i.e. $\mathbf{k}\cdot\mathbf{r} \ll 1$). Certain combinations of electric dipole and other higher-order multipoles, most notably the electrical quadrupole, can also contribute to optical activity [11, 144]. However, such contributions are usually considered negligible, especially in isotropic media [145, 146]. As such, we term the circular dichroism attributed to combinations of electric dipoles, magnetic dipoles, and electric quadrupoles as “conventional circular dichroism” [Fig. 3.1].

However, it has been suggested [101] that optical activity could arise even in the absence of an electric dipolar response due to the excitation of toroidal multipoles. This is attributed to the similarities in the radiation properties of the electric and toroidal multipoles (see Section 2.1.3). We term such a mechanism of circular dichroism as “toroidal circular dichroism” [Fig. 3.1] to contrast it with the conventional electric and magnetic mechanism. It is anticipated that toroidal circular dichroism could be

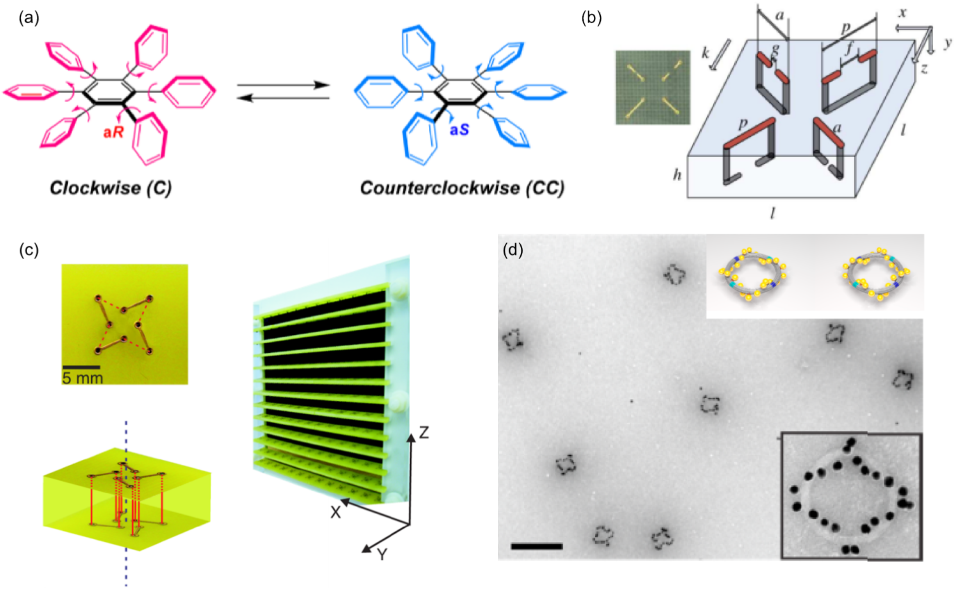

Figure 3.2: ***Prior art for the study chiral toroidal structures.*** *This figure shows example of toroidal structures which have been shown to exhibit chiral phenomena. (a) illustrates how chirality can arise in hexaarylbenzene compounds - so-called propeller chirality. Figure adapted from Ref. [147]. (b) shows a toroidal metamaterial polarisation-twister designed for the microwave regime. Figure adapted from Ref. [148]. (c) shows a metamaterial based on toroidal wire helices which exhibits strong dichroism in the microwave regime, in addition to a non-vanishing toroidal moment. Figure adapted from Ref. [101]. (d) shows plasmonic chiral toroidal metamolecules based on gold nanoparticles. The helical structures were constructed using a DNA origami method. Figure adapted from Ref. [149].*

a dominant mechanism in chiral structures with a toroidal topology that are of a comparable size to the wavelength (i.e. $\mathbf{k}\cdot\mathbf{r} \approx 1$) [101].

The study of toroidal structures exhibiting chiral phenomena has been reported on before in the literature, with many such structures across different size regimes having been identified [Fig. 3.2]. Indeed some of the toroidal structures introduced at the beginning of this thesis [Fig. 1.2] possess inherent chirality. Hexaryl-benzenes [21] are an example of such a compound, with recent studies having demonstrated that they can exhibit so-called propeller chirality, which arises due to the axial tilt of the peripheral benzene rings [147] [Fig. 3.2(a)]. Toroidal fullerenes can additionally be formed into enantiomeric structures by the choice of folding angle of the carbon sheets [15].

In terms of the metamaterial paradigm, the first presented concept of a toroidal metamaterial was inherently chiral owing to design being a closed toroidal solenoid [100]. Thus the chirality was a result of the winding angle of the solenoid. This was expanded on with a metamaterial that gave the first experimental signature of a toroidal response [101]. The chirality of this metamaterial was again a result of the solenoid winding number, which can be seen in Fig. 3.2(c). The circular dichroism observed from this metamaterial was analysed explicitly in terms of the excited microscopic multipoles, revealing the presence of a toroidal dipole. Although this could be considered the first indication of a form of toroidal circular dichroism, the toroidal response of the metamaterial was small compared to the conventional electric and magnetic multipoles, making at best a tertiary contribution to the observed dichroism.

Since this demonstration, several other artificial chiral toroidal systems have been investigated. The first unambiguous observation of a toroidal dipole [7], served as a template for a chiral polarisation twister for transforming between RCP and LCP light [Fig. 3.2(b)] [148]. Furthermore novel methods have been utilised to create chiral toroidal structures in the optical regime. DNA origami methods have been presented as a means of obtaining plasmonic toroidal metamolecules with a solenoid-like structure, thus giving them two enantiomeric forms and a strong circular dichroism response [149].

Despite this, the mechanism of toroidal circular dichroism had not been explicitly observed in these structures. In this chapter, a chiral toroidal metamaterial that exhibits toroidal circular dichroism shall be presented and evaluated both numerically and experimentally.

3.2 Theory

3.2.1 Linear and circularly polarised transmission matrices

We can describe the transmission through a metamaterial structure in terms of a complex transmission matrix t, which can be defined in an arbitrary polarisation basis. In a linearly polarised basis, the coefficients of t will take the form $t_{i,j}\,(i,j,=x,y)$, defined as:

$$t = \begin{bmatrix} t_{xx} & t_{xy} \\ t_{yx} & t_{yy} \end{bmatrix}. \tag{3.2}$$

Here, t_{xx} and t_{yy} represent direct x and y polarisation transmission coefficients, whereas t_{xy} and t_{yx} represent polarisation conversion from y to x and x to y respectively. We note that the components of t can be readily obtained form the S parameters in Section 2.3 for different incident polarisations. Equivalently, in a circularly polarised basis, the coefficients of t will take the form $t_{\alpha,\beta}\,(\alpha,\beta,=+,-)$, defined as:

$$t = \begin{bmatrix} t_{++} & t_{+-} \\ t_{-+} & t_{--} \end{bmatrix}. \tag{3.3}$$

Here, t_{++} and t_{--} represent direct RCP and LCP transmission coefficients, whereas t_{+-} and t_{-+} represent polarisation conversion from LCP to RCP and RCP to LCP respectively. The intensity of transmission T can be readily obtained from $T = |t|^2$. Circular dichroism Δ is then defined as:

$$\Delta = |t_{++}|^2 - |t_{--}|^2\,, \tag{3.4}$$

As outlined in Section 2.3, the vector network analyser and horn antennae utilised for the experimental study operate in a linearly polarised basis and so return $t_{i,j}$. One can move from a linear to a circularly polarised basis ($t_{i,j} \to t_{\alpha,\beta}$) using the transformations below:

$$\begin{bmatrix} t_{++} & t_{+-} \\ t_{-+} & t_{--} \end{bmatrix} = \frac{1}{2} \begin{bmatrix} t_{xx} + t_{yy} + i\,(t_{xy} - t_{yx}) & t_{xx} - t_{yy} - i\,(t_{xy} + t_{yx}) \\ t_{xx} - t_{yy} + i\,(t_{xy} + t_{yx}) & t_{xx} + t_{yy} - i\,(t_{xy} - t_{yx}) \end{bmatrix}, \tag{3.5}$$

Thus allowing for characterisation of a metamaterial's response to circularly polarised light from purely linearly polarised data.

3.2.2 Circular dichroism in a linear basis

When considering circular dichroism in terms of the microscopic excitations of the medium, it is more intuitive to work in a linearly polarised transmission basis, as this will directly relate to the microscopic multipole components excited in a linear basis. In this section, we will derive the equation for circular dichroism [Eq. 3.4] in a linear basis, and demonstrate the explicit dependence of circular dichroism on the linear polarisation conversion coefficients, t_{xy} and t_{yx}.

First we take the definitions of t_{++} and t_{--} from the linear-to-circular transformations in Eq. 3.5:

$$t_{++} = \frac{1}{2}\left[t_{xx} + t_{yy} + i\,(t_{xy} - t_{yx})\right] = a + ib, \tag{3.6}$$

$$t_{--} = \frac{1}{2}\left[t_{xx} + t_{yy} - i\,(t_{xy} - t_{yx})\right] = a - ib, \tag{3.7}$$

Where $a = \frac{t_{xx}+t_{yy}}{2}$ and $b = \frac{t_{xy}-t_{yx}}{2}$. Squaring these gives:

$$|t_{++}|^2 = (a + ib)\,(a^* - ib^*)\,, \tag{3.8}$$

$$|t_{--}|^2 = (a - ib)\,(a^* + ib^*)\,, \tag{3.9}$$

Where * indicates the complex conjugate. The circular dichroism [Eq. 3.4] can now be written as:

$$\Delta = |t_{++}|^2 - |t_{--}|^2 = (a + ib)\,(a^* - ib^*) - (a - ib)\,(a^* + ib^*)\,. \tag{3.10}$$

Expanding this and simplifying leads to:

$$\Delta = 2i\,(a^* b - a b^*)\,. \tag{3.11}$$

Using the identity $\mathrm{Im}(z) = \frac{z-z^*}{2i}$, this can be rewritten as:

$$\Delta = -4\mathrm{Im}\left(a^* b\right). \tag{3.12}$$

Finally, subbing back in for a and b yields:

$$\Delta = -\mathrm{Im}\left[\left(t^*_{xx} + t^*_{yy}\right)\left(t_{xy} - t_{yx}\right)\right]. \tag{3.13}$$

Therefore $\Delta \propto t_{xy} - t_{yx}$, i.e. the difference in either amplitude or phase between the linear poalrisation conversion terms.

3.2.3 Mechanism for conventional circular dichroism

In the previous section, we established from Eq. 3.13 that circular dichroism is proportional to a difference between the linear conversion terms in the transmission matrix. Here we will relate this equation to the microscopic mechanism for conventional circular dichroism established in Fig. 3.1.

The simplest microscopic multipole combination that can lead to circular dichroism is a combination of co-aligned electric and magnetic dipoles. It is well established that electric dipoles and magnetic dipoles have an identical far-field radiation pattern. However, an electric dipole radiates electric field parallel to the dipole axis, whereas a magnetic dipole radiates electric field orthogonal to its axis. Consequently, co-aligned and co-located electric and magnetic dipoles will in general radiate elliptical polarisation.

Such a situation is illustrated in Fig. 3.3, which illustrates a metamaterial structure designed to support co-aligned electric and magnetic dipoles. The structure is composed of metal wires in spiral shapes embedded in a dielectric substrate. The spiral shape of the wires gives this structure intrinsic 3D chirality, with two enantiomers. The metamaterial is embedded in the xy plane and driven by a plane wave incident along ther z-axis with linear y-polarisation i.e. along the axis of the metal spirals. The incident light will excite charge-current multipoles in the metal spirals which will contribute to the transmission coefficients of the metamaterial. Similar chiral structures have been described in Refs. [150, 151].

The primary charge current configurations excited on an individual metamolecule are shown in the insets to Fig. 3.3. Initially the incident y-polarised light will drive charge separation between the top and bottom of the spiral, resulting in an electric dipole $\mathbf{p_1}$ aligned along the y-direction. This dipole will radiate y-polarised radiation into the far-field and so we can write the t_{yy} transmission component of the metamaterial in terms of the incident E-field E_y^{inc} and the contribution from the electric dipole radiation $E_y^{rad}(\mathbf{p_1})$.

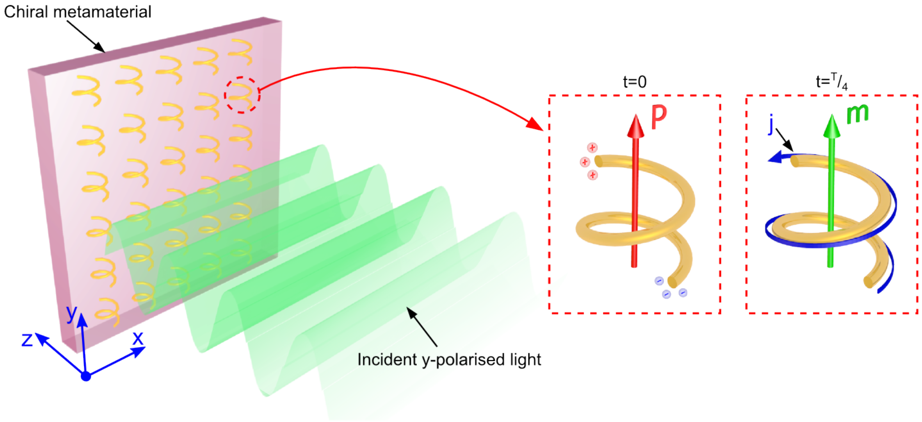

Figure 3.3: ***Co-aligned electric and magnetic dipoles in a chiral metamaterial.*** *This figure illustrates how a chiral metamaterial structure can support the co-aligned electric and magnetic dipoles required for circular dichroism. The metamaterial consists of metal spirals embedded in a dielectric substrate, with a y-polarised plane wave incident along the z-axis. The insets show the charge-current distributions on a single metamolecule at two points in time - $t = 0$ and $t = T/4$, where T represents the period of the plane wave.*

$$t_{yy} \propto E_y^{inc} + E_y^{rad}(\mathbf{p_1}). \tag{3.14}$$

We note that in this configuration, there is also a separation of charges in the $z-direction$ due to the 1.5 turns of the helical wire, causing a z-aligned electric dipole component. However, this component will primarily radiate in the plane of the array, and so will not contribute to the far-field scattering of the metamaterial.

A quarter of an optical cycle after the excitation of the electric dipole, the charge separation gives way to currents as the electrons are driven from one end of the spiral to the other. These circulating currents result in a magnetic dipole $\mathbf{m_1}$ aligned along the y-direction. This dipole will radiate E-field orthogonal to its axis $E_x^{rad}(\mathbf{m_1})$ and so can be used to define the t_{xy} transmission matrix component:

$$t_{xy} \propto E_x^{rad}(\mathbf{m_1}). \tag{3.15}$$

We can now consider the analogous situation where the metamaterial is illuminated with x-polarised light. As the incident light is no-longer polarised along the axis of the metal spiral, the excitations of electric and magnetic dipoles will be accordingly weaker than in the y-polarised incidence case. Nonetheless, we can write the remaining components of the transmission matrix in terms of the excited electric $\mathbf{p_2}$ and magnetic $\mathbf{m_2}$ dipoles:

$$t_{xx} \propto E_x^{inc} + E_x^{rad}(\mathbf{m_2}), \tag{3.16}$$

$$t_{yx} \propto E_y^{rad}(\mathbf{p_2}). \tag{3.17}$$

We now refer to Eq. 3.13, which gives our definition for circular dichroism Δ in terms of the linear transmission components. We note that $\Delta \propto t_{xy} - t_{yx}$. We can sub our expressions for t_{xy} [Eq. 3.15] and t_{yx} [Eq. 3.17] into this to obtain:

$$\Delta \propto t_{xy} - t_{yx} = E_x^{rad}(\mathbf{m_1}) - E_y^{rad}(\mathbf{p_2}). \tag{3.18}$$

From this we can see that provided there is a difference in amplitude or phase between $\mathbf{m_2}$ (excited by y-polarised light) and $\mathbf{p_1}$ (excited by x-polarised light), the metamaterial will exhibit non-zero circular dichroism. We note from Fig. 3.3, there will necessarily be a phase difference between the electric and magnetic dipoles, thus resulting in circular dichroism independent of the amplitude of the multipoles.

3.3 Chiral toroidal metamaterial

The metamaterial used for this study has been derived from the structure previously shown to support a strong toroidal dipolar response under linearly polarized excitation. Its metamolecule consists of a cluster of four rectangular metallic wire loops embedded in a dielectric slab [Fig. 3.4(a)]. The loops are arranged about the axis of the metamolecule (y-axis) at separations of 90^o to give a fourfold symmetric structure, where opposite facing loops are separated by a distance r. The symmetry is then broken by introducing identical splits to the loops, located on either the top or the bottom sides of the slab and alternating between adjacent loops. The metamaterial is formed by translating the metamolecule along the x and y axes, resulting in a one-metamolecule thick metamaterial slab with a rectangular unit cell, as shown in Fig. 3.4(a). Although the individual metamolecules are achiral, the resulting metamaterial crystal is chiral due to the regular arrangement of its metamolecules (structural chirality) and is available in two enantiomeric forms interconnected by a mirror reflection [Fig. 3.4(b)].

The metamaterial sample was fabricated by etching a 35μm thick copper foil on both sides of a low-loss dielectric PCB laminate Rogers TMM® 3 [152] using high-resolution photolithography[1] [Fig. 3.4(c)]. The top and bottom patterns were electrically connected through narrow electroplated holes. All copper tracks were coated with a 2μm thick layer of gold to prevent oxidization and staining of copper, as well as to reduce Ohmic losses. The assembled metamaterial sample consisted of 24×24 metamolecules.

---

[1] Fabrication of the metamaterial was conducted by Dr. Wei Ting Chen and Prof. Din Ping Tsai at the National Taiwan University, Taipei, Taiwan.

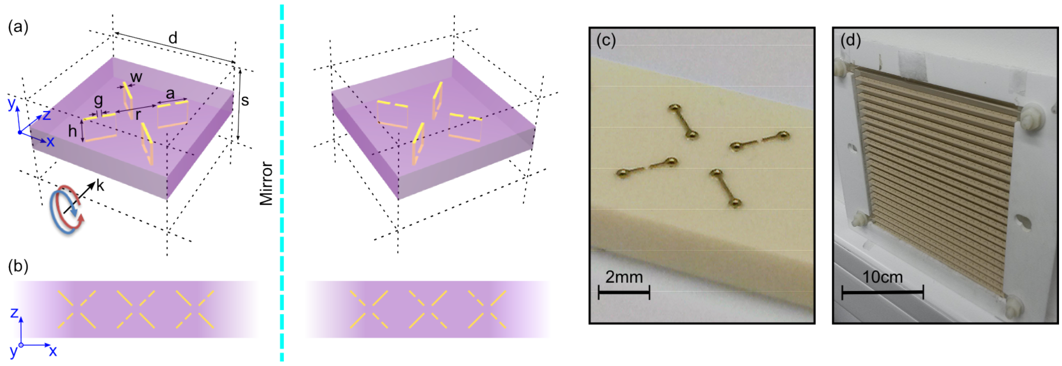

Figure 3.4: ***Schematic of the chiral toroidal metamaterial and fabricated structure.*** *This figure shows the metamaterial structure used to observe toroidal circular dichroism. (a) gives a schematic of the toroidal metamolecule and its orientation with respect to the metamaterial crystal lattice (indicated by dashed lines). The dimensions are* $d = 8$*mm,* $s = 7.5$*mm,* $h = 1.5$*mm,* $r = 2.44$*mm,* $g = w = 0.15$*mm and* $a = 1.8$*mm. RCP (red) and LCP (blue) light propagates along the* z *axis. The individual metamolecules are achiral, as indicated by the mirror image. (b) shows the bulk metamaterial formed by translating the unit cell along the* x *and* y *axes, which imposes structural chirality on the sample. The mirror image shows the enantiomeric form of the metamaterial crystal. (c) shows a close-up photograph of a fabricated toroidal metamolecule, whilst (d) shows the whole metamaterial sample after assembly.*

3.4 Results

Here, we shall present a set of experimental and numerical results in support of the hypothesis that the aforementioned chiral metamaterial structure exhibits toroidal circular dichroism as a dominant scattering mechanism.

3.4.1 Metamaterial transmission

To fully characterise the chiral toroidal metamaterial structure, we begin by evaluating the experimental transmission matrix in a linear basis $t_{i,j}$ [Eq. 3.2] where $i, j = x, y$. This experimental characterisation was conducted using the methodology described in Section 2.3 in a microwave anechoic chamber. Measurements of amplitude and phase were taken for all polarisation components of metamaterial transmission over a frequency range of 12.5-16.5GHz (wavelength range of 1.82-2.4cm), and were gated to remove spurious reflections as per Section 2.3.3. The linearly polarised transmission matrix $t_{i,j}$ was converted to a circularly polarised basis $t_{\alpha,\beta}$ [Eq. 3.3] where $\alpha, \beta = +, -$ using established transformations [Eq. 3.5].

To complement our experimental characterisation of the chiral toroidal metamaterial, a full-wave simulation of the metamaterial response using a three-dimensional finite-element solver (COMSOL 3.5a) in the harmonic domain. The full methodology is described in Section 2.4.1. The simulations were conducted over a frequency range

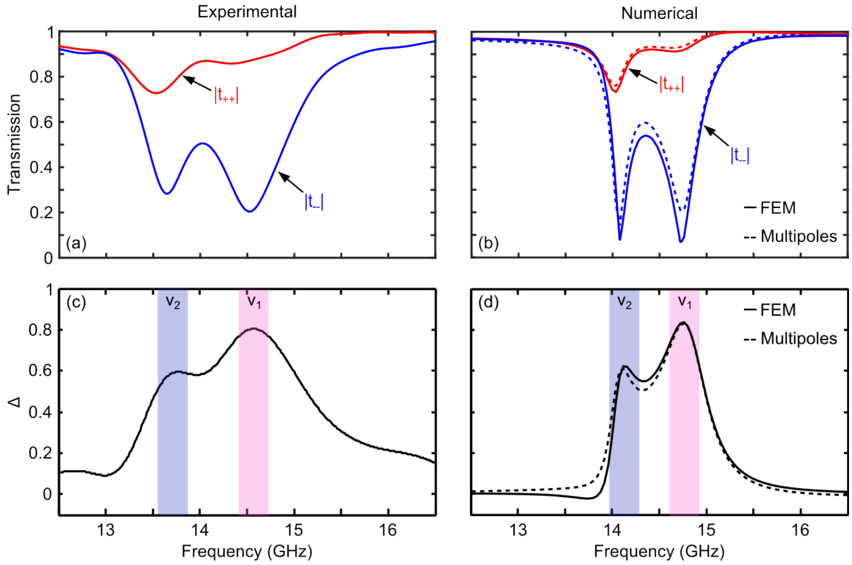

Figure 3.5: ***Transmission and dichroism of a chiral toroidal metamaterial.*** *This figure shows the experimentally measured (left column) and numerically calculated circular transmission response of the toroidal metamaterial. (a-b) show the amplitudes of the circularly polarised transmission t_{++} and t_{--}, while panels (c-d) show circular dichroism Δ. Results are calculated using two different methods - finite-element simulation and multipole decomposition of currents are shown by solid and dashed curves, respectively. Pink and navy bands mark the resonances of corresponding conventional (ν_1) and toroidal (ν_2) circular dichroism, respectively.*

of 12.5-16.5 GHz and utilised periodic boundary conditions to simulate an infinite metamolcule array. The wires of the metallic loops were assumed to be infinitely thin strips of perfect electric conductors. The permittivity of the dielectric medium was set to $\varepsilon_r = 3.45 - 0.007i$, which corresponds to the Rogers TMM® 3 dielectric laminate used in fabrication of the sample [152]. From this analysis, the circularly polarised transmission matrix $t_{\alpha,\beta}$ for the simulated metamaterial can be obtained.

Circular dichroism Δ is determined by the difference between direct circularly polarised transmission coefficients i.e $|t_{++}|^2 - |t_{--}|^2$ [Eq. 3.4]. As such, Fig. 3.5(a) and (b) compares the amplitudes of the direct circular polarisation transmission coefficients $|t_{++}|$ and $|t_{--}|$ of the (a) experimental and (b) numerical transmission matrices. The presence of circular dichroism is immediately clear from observing the difference between the plots of $|t_{++}|$ and $|t_{--}|$. This is reinforced in Fig. 3.5(c) and (d) which explicitly plots the circular dichroism from the experimental and numerical data respectively. Good agreement is obtained between the experimental and numerical data, with discrepancies arising due to fabrication tolerances, uncertainty in the permittivity of the dielectric laminate, and use of infinitely thin PEC strips in the simulations.

Two clear resonances in the circular dichroism spectra are identified in both cases, identified by the purple and pink bands. In the experimental data, these resonances occur at $\nu_1 = 14.6$GHz and $\nu_2 = 13.6$GHz. In the numerical data, they occur at

$\nu_1 = 14.7$GHz and $\nu_2 = 14.1$GHz. The magnitude of circular dichroism at ν_1 and ν_2 approaches ~ 0.8 and ~ 0.6 respectively.

3.4.2 Multipole analysis

Having confirmed that the chiral toroidal metamaterial exhibits circular dichroism in both its experimental and numerical transmission response, it is now necessary to evaluate the microscopic origin of this observed phenomenon in terms of the multipolar charge-current excitations supported by the metamolecule. This will confirm if the observed phenomenon can be considered conventional circular dichroism, or if the mechanism of toroidal circular dichroism plays a role [Fig. 3.1].

The multipole moments were computed based on spatial distributions of the induced conduction and displacement current densities extracted from the simulated metamolecule. These were evaluated up to octupole order for conventional multipoles and the quadrupole order for toroidal multipoles from the integrals described in Section 2.2.1. Furthermore, following the methodology described in Section 2.4.2 we can directly link the multipolar excitations of the individual metamolecules to the far-field response of the whole metamaterial array.

This yields a new transmission matrix $\tilde{t}_{i,j}$, in which the individual matrix terms are reconstructed from the the incident field and the far-field radiation of the excited multipoles.

$$\tilde{t}_{i,j} = \begin{bmatrix} \tilde{t}_{xx} & \tilde{t}_{xy} \\ \tilde{t}_{yx} & \tilde{t}_{yy} \end{bmatrix}. \tag{3.19}$$

This matrix can then be converted from linear to circular polarisation using Eq. 3.5. The accuracy of this approach can be seen in Fig. 3.5, which compares the metamaterial transmission obtained directly from finite element simulations (solid curves), with transmission calculated from multipole composition and the reconstructed transmission matrix $\tilde{t}_{i,j}$. A good match is achieved between the two methods, with discrepancies likely arising due to the complexities of evaluating currents on infinitely thin PEC strips

In Section 3.2.2 it was shown that the linear transmission matrix components t_{xy} and t_{yx} i.e. the linear conversion terms, can be regarded as a manifestation of the observed circular dichroism in a linear basis. From Eq. 3.13 it can be seen that circular dichroism will only exist for nonzero and nonidentical polarisation conversion terms. We note that necessarily $|t_{xy}| = |t_{yx}|$, as dictated by the symmetry of the metamaterial with respect to the propagation direction (z-axis). As such we consider the linear conversion terms of the reconstructed transmission matrix $\tilde{t}_{xy}$ and $\tilde{t}_{yx}$ and examine the microscopic multipoles that contribute to these terms.

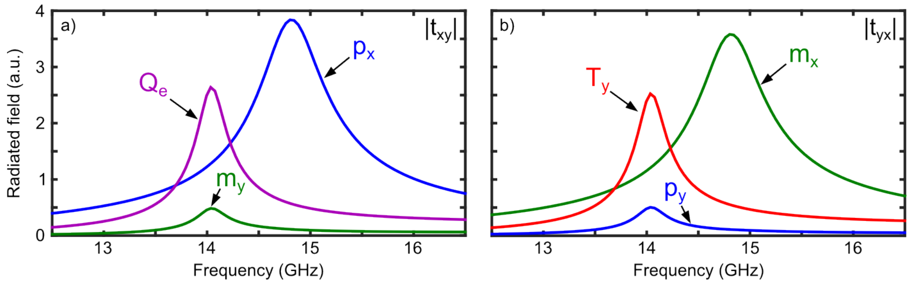

Figure 3.6: ***Multipole transmission coefficients of chiral toroidal metamaterial.*** *This figure shows the amplitudes of the fields radiated by the four most dominant multipole components (electric dipole* $\mathbf{p}$*, magnetic dipole* $\mathbf{m}$*, toroidal dipole* $\mathbf{T}$*, and electric quadrupole* $\mathbf{Q_e}$*) that contribute to the polarisation conversion response of the chiral toroidal metamaterial. (a) shows the* $|t_{xy}|$ *field amplitudes, and (b) shows the* t_{yx} *field amplitudes.*

Fig. 3.6 shows the multipole terms that contribute to $\tilde{t}_{xy}$ and $\tilde{t}_{yx}$ scattering from the metamaterial. For clarity, only six multipole components have been displayed, these being x components of electric $\mathbf{p}$ and magnetic $\mathbf{m}$ dipoles at ν_1 and electric quadrupole $\mathbf{Q_e}$ and y components of electric, magnetic, and toroidal $\mathbf{T}$ dipoles at ν_2. Other multipole components are at least one order of magnitude smaller than these dominant ones.

In agreement with the modeled circular dichroism data [Fig. 3.5], the resonances in the multipole scattering occur at frequencies ν_1 and ν_2. Fig. 3.6 indicates a symmetry to the linear conversion response as expected from the aforementioned $|t_{xy}| = |t_{yx}|$ condition. However, the multipoles contributing to the same resonant features in t_{xy} and t_{yx} are different. This indicates that the observed circular dichroism can be attributed to the simultaneous excitation of pairs of different multipoles. In particular, at ν_1 the dominant pair comprises electric and magnetic dipoles with collinear moments - p_x and m_x . Such a combination corresponds to the conventional mechanism of optical activity and hence is considered as a reference case in our further analysis. At ν_2, however, the contributions of p_x and m_x become only secondary, whereas the circular dichroism appears to be underpinned by the previously unexplored combination of the toroidal dipole T_y and electric quadrupole Q_e. We also note a tertiary contribution at ν_2 from the p_y and m_y multipole pair.

The presence of these multipole pairs can be visually detected in the near-field distributions of electric and magnetic field inside the metamolecule when driven by circularly polarised light. This can be examined using the finite-element simulations of the metamolecule, which provides specifically the near-field topology of the excitation. Fig. 3.7 illustrates the electric and magnetic fields in the near field of the simulated metamolecule when under excitation with LCP light. It si noted that as the cross-sections are taken through the centre of the metamolecule wire loops, strong localised fields within the splits in the wire loops are not visible.

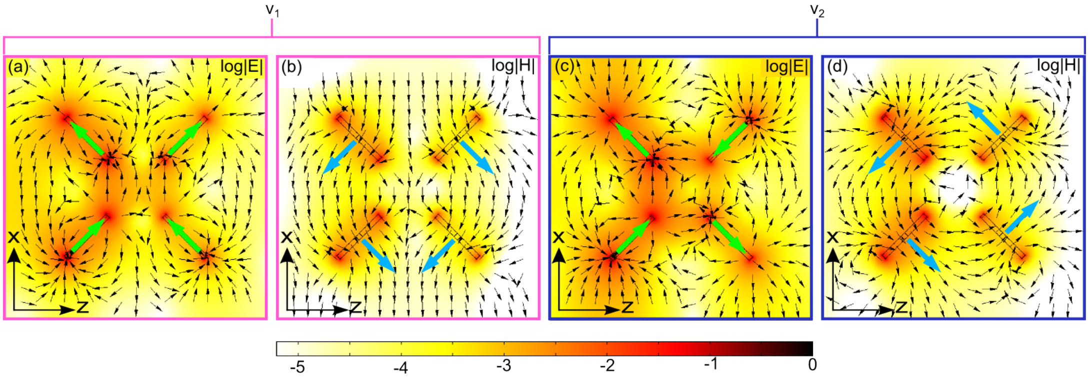

Figure 3.7: ***Near-field distributions of the chiral toroidal metamaterial at resonance.*** *This figure gives the near-field distributions of* $\log|E|$ *and* $\log|H|$ *around the simulated metamolecule when excited by LCP light at (a-b)* ν_1 *and (c-d)* ν_2*. The black arrows give the corresponding E and H field direction. The green (blue) arrows show the orientation of the induced electric (magnetic) dipoles for the individual rings.*

At ν_1 the field lines of both electric and magnetic fields are seen to align parallel to the x axis, which indicates the presence of electric and magnetic dipolar excitations in the metamolecule with the net dipole moments being collinear and oriented along the x axis[Fig. 3.7(a)-(b)]. At ν_2 the distribution of the electric field features a pattern similar to that in Fig. 3.7(a) but with the field lines on the opposite sides of the metamolecule aligned anti-parallel to each other [Fig. 3.7(f)], which represents the anti-parallel electric dipoles indicative of an electric quadrupole excitation. The magnetic field is confined within a well-defined ring-like area where the field lines form a closed loop, threading through all individual resonators of the metamolecule [Fig. 3.7(c)]. The magnetic field is rapidly vanishing outside of this region. Such a magnetic-field configuration is unique to the toroidal dipolar excitation with a net dipole moment aligned parallel to the axis of the metamolecule (y axis) and is formed by poloidal currents flowing in the individual wire loops of the metamolecules.

3.4.3 Transmission matrix under rotation transformation

In the previous section we have identified the multipoles that are anticipated to be key contributors to the circular dichroism of the metamaterial, which appear in symmetric pairs in the linear conversion coefficients of the metamaterial transmission matrix [Fig. 3.6]. It is important to determine whether this mechanism is independent of the coordinate system chosen for the analysis.

To evaluate this we can apply a rotation transformation to the linear scattering matrix [Eq. 3.2]:

$$R\begin{bmatrix} t_{xx} & t_{xy} \\ t_{yx} & t_{yy} \end{bmatrix} R^T = t', \tag{3.20}$$

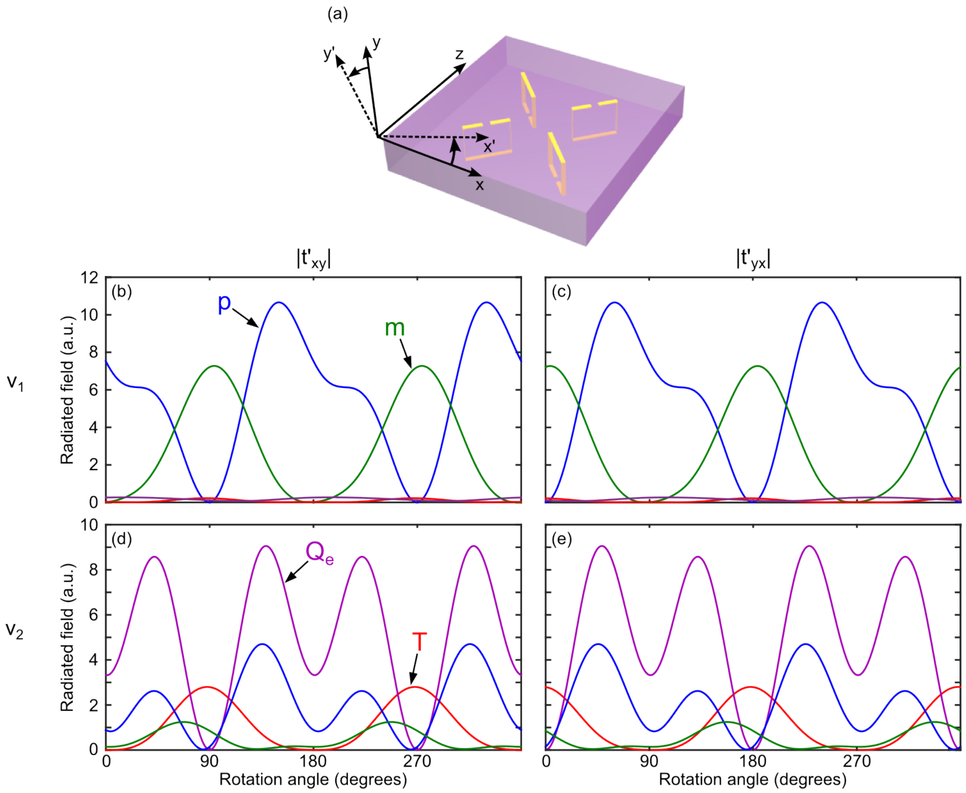

Figure 3.8: ***Multipole transmission coefficients of the chiral toroidal metamaterial under rotation.*** *(a) shows the formation of the new coordinate system* (x', y', z) *through a rotation about the z-axis of the metamaterial structure. (b)-(e) show the amplitudes of the fields radiated by the four most dominant multipole components (electric dipole* $\mathbf{p}$*, magnetic dipole* $\mathbf{m}$*, toroidal dipole* $\mathbf{T}$*, and electric quadrupole* $\mathbf{Q_e}$*) that contribute to the polarisation conversion response as a function of rotation angle* $(0 \rightarrow 360^o)$*. b) and c) show respectively* $|t_{xy}|$ *and* $|t_{yx}|$ *at* $\nu_1 = 14.7GHz$*. d) and e) show respectively* $|t_{xy}|$ *and* $|t_{yx}|$ *at* $\nu_2 = 14GHz$*.*

Where R represents the rotation matrix:

$$R = \begin{bmatrix} cos\,(\theta) & sin\,(\theta) \\ -sin\,(\theta) & cos\,(\theta) \end{bmatrix}, \tag{3.21}$$

Where θ is the angle of rotation. This gives a transmission matrix t' in a new coordinate system, defined by two orthogonal vectors offset from the original x and y-axes: (x', y'). This procedure is analogous to physically rotating the metamaterial in space i.e. a rotation about the z-axis in Fig. 3.8(a). We note that under rotation of 90^o, $|t'_{yx}| = |t_{xy}|$ and $|t'_{xy}| = |t_{yx}|$. Similarly, under rotations of 180^o, $|t'_{yx}| = |t_{yx}|$ and $|t'_{xy}| = |t_{xy}|$.

We apply this rotation scheme to our reconstructed transmission matrix [Eq. 3.19] at the identified resonant frequencies ν_1 and ν_2. This yields the contributions of different multipoles to the rotated linear conversion components t'_{xy} and t'_{yx} at resonance for rotation angles of $\theta = 0 \rightarrow 360^o$.

From Fig. 3.6, we have identified the key multipole contributors to t_{xy} and t_{yx} radiation, these being the electric p_x and magnetic dipole m_x components at the ν_1 resonance, and the toroidal dipole T_y and electric quadrupole Q_e components at the ν_2 resonance. It is anticipated that the dominance of these multipoles should be unchanged under rotation of the coordinate system.

We first consider the effect of rotation at the ν_1 resonance, illustrated in Fig. 3.8(b) and (c). Necessarily for $\theta = 0^o$, $t'_{xy} = t_{xy}$ and $t'_{yx} = t_{yx}$, with the amplitude of the multipole radiation being identical to that in Fig. 3.6. It can be seen that the electric and magnetic dipole components are dominant across a full 360^o rotation of the transmission matrix. It can be seen that the traces in Fig. 3.8(b) and (c) are identical except for a 90^o phase shift between them, which reflects the fact that x and y are orthogonal.

Under rotations where θ is a multiple of 90^o, we find that t'_{xy} and t'_{yx} are dominated by either electric or magnetic dipole radiation components, thus preserving the mechanism for circular dichroism identified from Fig. 3.6 for these rotation angles. The situation for other angles becomes more complex. This is a consequence of the principle axes of the structure being aligned along the x and y directions and so for any coordinate system not aligned with these, the role of anisotropy in the electromagnetic response will increase. This can be seen in Fig. 3.8(b) at $\approx 150^o$ where the electric dipole response is strongest for t'_{xy}, corresponding to the angle of greatest anisotropy.

A similar situation is observed at the ν_2 resonance in Fig. 3.8(d) and (e). At 90^o intervals, t'_{xy} and t'_{yx} are dominated by either the electric quadrupole or toroidal dipole, as anticipated from Fig. 3.6, but for other angles the increase in anisotropy complicates the multipole response. Nonetheless, for coordinate systems aligned with the principle axes of structure where anisotropy is minimised, it is clear that the multipole contributions to t'_{xy} and t'_{yx} are invariant under rotation.

3.4.4 Eigenstate analysis

In the previous sections, we have provided qualitative evidence for the role of the toroidal dipole-electric quadrupole mechanism in the circular dichroism of the chiral metamaterial. Here we will seek to give a more quantitative description by analysis of the elliptical eigenstates of the metamaterial. This approach will also address the issue with separating circular dichroism from linear birefringence due to anisotropy identified in the previous section.

In general, a metamaterial structure with a transmission matrix described by Eq. 3.3 will have two counter-rotating elliptical eigenstates, which satisfy the following relation:

$$\begin{bmatrix} t_{++} & t_{+-} \\ t_{-+} & t_{--} \end{bmatrix} \begin{bmatrix} A_{+}\mathbf{e}_{+} \\ A_{-}\mathbf{e}_{-} \end{bmatrix} = \lambda \begin{bmatrix} A_{+}\mathbf{e}_{+} \\ A_{-}\mathbf{e}_{-} \end{bmatrix}, \tag{3.22}$$

Where $A_{+}\mathbf{e}_{+}$ and $A_{-}\mathbf{e}_{-}$ represent respectively the right and left handed components of the eigenvectors, and λ represents the associated eigenvalue. The two eigenvectors represent incident electromagnetic waves that can propagate through the metamaterial without a change to their polarisation state. The polarization eigenstates can be characterised in terms of their ellipticity angle ϵ using the following relation:

$$\epsilon = \frac{1}{2} arcsin \left(\frac{|A_{+}|^2 - |A_{-}|^2}{|A_{+}|^2 + |A_{-}|^2} \right), \tag{3.23}$$

Where $|\epsilon|$ takes values between $\pi/4$ (circular polarization) and 0 (linear polarization). A positive ellipticity angle defines right handed rotation, whilst a negative defines left handed rotation.

We can identify two limiting cases. The first is where the ellipticity takes the maximum value of $\epsilon = \pm\pi/4$. This corresponds to an optically active (chiral) medium with a purely circularly polarised eigenstate. The second is when the ellipticity tends to 0, represents a linearly birefringent (achiral) anisotropic media with a purely linearly polarised eigenstate.

As demonstrated in the previous section, we can reconstruct the transmission matrix of the chiral toroidal metamaterial entirely based on the radiated fields of the excited microscopic multipoles [Eq. 3.19]. The eigenstate ellipticities obtained from this multipole transmission matrix are shown in Fig. 3.9(a), in addition to traces of the eigenstates at resonance. It can be seen that at both resonances ν_1 and ν_2 the metamaterial eigenstates are counter-rotating polarisation ellipses, indicating the presence of both optical activity (circular dichroism) and linear birefringence (owing to metamaterial anisotropy) phenomena in the structure.

Obtaining a multipole transmission matrix makes it possible to directly trace the source of eigenstate ellipticity, and thus circular dichroism, to the independent multipoles. This is achieved by subtracting the multipole contributions from the transmission matrix coefficients and recalculating the ellipticity angles of the resultant eigenstates. We note that from Eq. 3.13, circular dichroism is dependent on the difference between the linear conversion terms of the transmission matrix, t_{xy} and t_{yx}, and as such we subtract multipole contributions from these components.

From Fig. 3.6, we have identified the key multipole contributors to t_{xy} and t_{yx} radiation, these being the electric p_x and magnetic dipole m_x components at the ν_1 resonance, and the toroidal dipole T_y and electric quadrupole Q_e components at the

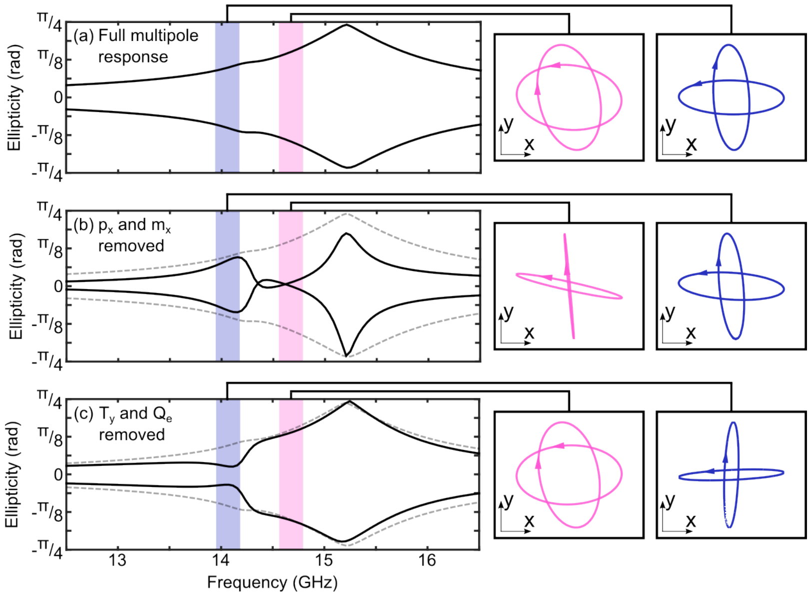

Figure 3.9: ***Eigenstate ellipticities of the chiral toroidal metamaterial.*** *This figure shows the ellipticity angles of the metamaterial eigenstates and the associated polarization ellipses at* ν_1 *and* ν_2*, calculated based on the multipole expansion of microscopic charge-current excitations supported by toroidal metamolecules. (a) shows the results obtained using the complete multipole set. (b) and(c) show the results corresponding to pairs* p_x*-*m_x *and* T_y *-*Q_e *being removed from the microscopic response of the metamaterial (solid curves) and compared to the complete multipole response from (a) (dashed curves).*

ν_2 resonance. As such it it anticipated that these pairs of multipoles will be the primary contributors to the circular dichroism at these resonances. Subtraction of these multipole pairs from the multipole transmission matrix should result in the term in Eq. 3.13 $(t_{xy} - t_{yx}) \to 0$, and so the circular dichroism $\Delta \to 0$.

This subtraction of multipole pairs can be expected to be visible in the ellipticities of the metamaterial's polarisation eigenstates. In the absence of the multipole contributors to t_{xy} and t_{yx}, it is anticipated that the ellipticities of the eigenstates will tend towards zero, corresponding to an achiral material, indicating explicitly the contribution of the multipoles to circular dichroism.

We first examine the case of the ν_1 resonance by removing the contributions of p_x and m_x from the transmission matrix and evaluating the modified polarisation eigenstates. The ellipticities of the new eigenstates are shown in Fig. 3.9(b). It can be immediately seen that this leads to a decrease in $|\epsilon|$ to approximately $\pi/60$ for both eigenstates. This is reinforced by the eigenstate traces which depict how the elliptical polarisations collapse to an almost linear state in the region of ν_1. This significant transition towards a purely anisotropic response confirms that on the microscopic level the observed circular dichroism at ν_1 results from electric and magnetic dipole scattering induced in the metamolecules.

We now utilise the same approach for the ν_2 resonance, subtracting the contributions of T_y and Q_e. The ellipticities of the new eigenstates are shown in Fig. 3.9(c). A similar effect is observed, with $|\epsilon|$ decreasing to approximately $\pi/30$, with the eigenstate traces showing a collapse towards a linear state in the region of ν_2. This supports our hypothesis that the circular dichroism observed at ν_2 is underpinned primarily by the resonant combination of the toroidal dipole and the electric quadrupole.

We note that magnitude of ellipticity change in Fig. 3.9(c) is smaller than in Fig. 3.9(b). This can be attributed to contributions from p_x and m_x which, whilst only dominant at ν_1, are non-negligible at ν_2 [Fig. 3.6]. It can be seen that the y-aligned components p_y and m_y also play a non-negligible role. Nonetheless, it is clear that the combination of the toroidal dipole and electric quadrupole represents the dominant mechanism.

3.5 Summary

In this chapter, experimental and numerical investigations of a structurally-chiral metamaterial have been conducted. The metamaterial is observed to exhibit strong circular dichroism and a resonant toroidal dipolar response. Analysis of the fields scattered by the charge-current multipoles induced in the metamolecules and the polarization eigenstates of the system reveals that the metamaterial exhibits both the conventional mechanism of circular dichroism by way of electric and magnetic dipole transitions and a previously unobserved form of circular dichroism, underpinned by the resonant excitation of the toroidal dipole and electric quadrupole.

We note that metamaterial structures have been utilized to replicate many phenomena which occur in natural media with metamolecules being analogous to molecules and conduction currents being analogous to displacement currents and polarization. Hence, this observed multipole combination is anticipated to be the cause of (or at least strongly contribute to) circular dichroism in many other material systems with toroidal topology, such as large molecules commonly encountered in chemistry and biology where optical activity is directly linked to the topology of the whole molecule. Examples of such structures include the hexa-arylbenzenes and chiral gold nanoparticles shown in Fig. 3.2 which have been shown to exhibit circular dichroism, but have not had the microscopic origin confirmed.

It is important to note that the new form of circular dichroism identified here is underpinned by toroidal dipole and electric quadrupole excitations. It is anticipated that simultaneous excitation of the toroidal dipole and magnetic dipole will also lead to a form of toroidal circular dichroism, that would be directly analogous to the conventional mechanism of electric and magnetic dipoles [Fig. 3.1]. Although this mechanism of toroidal circular dichroism is yet to be observed, there is potential for it to be observed in helical molecules which would support co-aligned magnetic and toroidal dipoles.

Chapter 4

Interaction of toroidal scatterers with structured beams

4.1 Introduction

In the context of the previous chapter, and in general the observations of dynamic toroidal excitations as a whole, the dominant approach has been to consider careful engineering of the structure in order to suppress electric and magnetic modes whilst enhancing the toroidal response. Whilst this has led to the successful observation of toroidal responses in a variety of regimes (see Chapter 1), fabrication of structures that support such responses becomes more difficult to achieve at smaller scales. As such, there has been recent interest in obtaining toroidal responses from more structurally-simple systems, for example simple core-shell nanoparticles [120], nanowires [122], and dielectric discs [51].

Here an alternative approach is considered - in contrast to engineering of the meta-molecules with a complex design, structured light is utilised to excite a toroidal response, relying on more complex topologies of the incident light field to drive toroidal dipoles.

Our interest lies with radially polarised beams, in which the E-field polarisation is directed along the $\hat{\rho}$ unit vector. This polarisation distribution E_ρ can be readily obtained by the superposition of two orthogonally polarised TEM_{01} Laguerre-Gaussian modes [153]. Radially polarised beams are subset of the larger family of cylindrical vector beams, which also includes azimuthally polarised light and more complex beam arrangements such as those with orbital angular momentum. Destructive interference between anti-parallel E components as $\rho \to 0$ results in the E_ρ-field vanishing in the center of the beam. This drop in beam intensity as $\rho \to 0$ gives the beam's transverse cross-section a "doughnut" profile. Although the radial fields vanish as $\rho \to 0$, there still exists on-axis E-field components aligned along the direction of propagation.

Cylindrical vector beams have been the subject of increasing research owing to their polarisation properties and small focal spot size [154, 155], which has led to a variety of applications in nanophotonics and plasmonics [156, 157]. The potential applications of cylindrical vector beams makes a means of interacting with and controlling them highly desirable. Metamaterial structures provide a platform for engineering such an interaction, with several structures having been suggested in the literature [158, 159]. However, little attention has been given to the response of individual metamolecules to incident radially polarised light, and consequently, what the optimum microscopic excitation is for interaction.

The toroidal dipole appears to be a prime candidate for optimum interaction. The current distribution of a toroidal dipole necessarily requires radial currents i.e. $\mathbf{J}\cdot\hat{\rho} \neq 0$, which would be readily excited by E_ρ of a radially polarised beam. Furthermore, a radially polarised beam possesses an azimuthal H-field, which is analogous to the near-field magnetic field distribution of a toroidal dipole. Recent work by Bao et al has demonstrated the viability of using radially polarised light to excite toroidal dipole responses in a simple metal-dielectric-metal sandwich nanostructure [121].

Here, we seek to explicitly demonstrate that the toroidal dipole provides a superior means of interacting with radially polarised light when compared to the conventional multipoles. The theme here of driving toroidal resonances with structured light shall form the basis for discussions in later chapters of this thesis. As radial electric fields are not conducive to magnetic excitations, we neglect comparison with the magnetic multipole family and focus on the electric dipole, which shares an identical far-field radiation pattern to the toroidal dipole (see Appendix B) [44, 52].

4.2 Simulations

4.2.1 Defining a radially polarised incident beam

We can begin by considering the scalar field distribution of two TEM_{01} Laguerre-Gaussian modes, with orientation along the x and y axes respectively. The scalar field distributions are given by:

$$E_x(r,\phi) = E_0 \frac{r}{w} exp\left(\frac{-r^2}{w^2}\right) cos(\phi), \tag{4.1}$$

$$E_y(r,\phi) = E_0 \frac{r}{w} exp\left(\frac{-r^2}{w^2}\right) sin(\phi), \tag{4.2}$$

Where r and ϕ represent the cylindrical coordinates, and w represents the width of the beam waist. The summation of these two scalar fields when given orthogonal vector

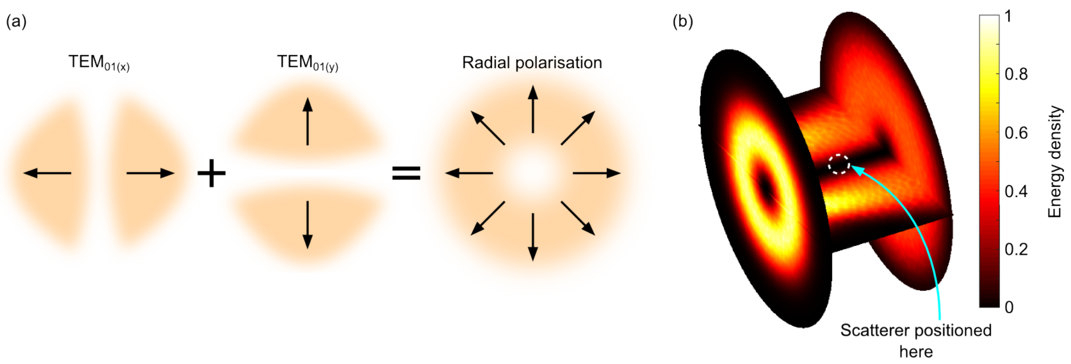

Figure 4.1: ***Simulation of a radially polarised beam.*** *(a) illustrates the construction of a radially polarised beam from TEM$_{01}$ Laguerre-Gaussian modes. The arrows indicate the E-field orientation. (b) shows the energy density of a radially polarised beam for different slices through the simulation domain. The beam propagates from left to right and takes the characteristic doughnut topology of radially polarised light. The scatterers under investigation are placed in the center of the simulation domain.*

orientations leads to the formation of either azimuthally or radially polarised light. The summation required for radially polarised light is given below:

$$E_r(r,\phi)\hat{r} = E_x(r,\phi)\hat{x} + E_y(r,\phi)\hat{y}. \tag{4.3}$$

This procedure is illustrated in Fig. 4.1(a) which illustrates the formation of a radial polarisation distribution from the addition of TEM$_{01}$ modes. Fig. 4.1 illustrates the subsequent generation of a radially polarised beam ($\nu = 26$GHz) in a full 3D COMSOL simulation, propagating through a cylindrical domain 3cm in length. The beam is well confined within the doughnut-shaped region and undergoes diffraction in the expected manner for a Laguerre-Gaussian beam. The scatterer under interrogation shall be placed in the center of the simulation domain. We note that in general, radially polarised beams also possess a longitudinal field component, that has a magnitude dependent on how well collimated the beam is. We do not define this longitudinal field in the boundary specifications of the model, but instead allow it to arise as a necessary consequence of Maxwell's equations in the solver.

4.2.2 Design and optimisation of toroidal scatterer

The design for the T-scatterer consists of two perfect electrical conductor (PEC) '+' elements with bar length s and width w, with $s \gg w$ [Fig. 4.2]. The width w is chosen to be 0.5mm length s is chosen to be 1cm, which should support $\lambda/2$ resonances in each spoke of the '+' element in the ~30GHz regime i.e. $\nu_0 = 30$GHz, $\lambda_0 = 1$cm. The two '+' elements are separated by a dielectric spacer of thickness d and refractive index $n = 1.73 + 0.0011i$ corresponding to a circuit board laminate typically used for fabri-

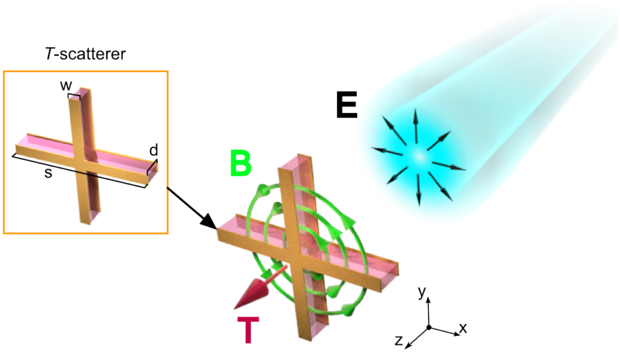

Figure 4.2: ***Schematic of the T-scatterer design.*** *This figure gives a schematic of a radially polarised beam propagating along the z axis interacting with a T-scatterer. The expected B field and resultant toroidal dipole T excited on the scatterer are illustrated. The inset gives the characteristic parameters of the T-scatterer: the length s and width w of the '+'-shaped bars, and the dielectric thickness d.*

cation of GHz-scale metamaterials. The dielectric layer acts to facilitate displacement currents between the two '+' shaped elements, which complete the poloidal current configuration necessary for toroidal dipolar excitation. It is orientated such that the '+' lies perpendicular to the propagation axis (z-axis) of an incident radially polarised beam and centered at $xy = 0$.

This configuration should allow for maximum coupling of the scatterer to incident radially polarised light, leading to a toroidal dipole orientated along the z-axis [Fig. 4.2]. It is anticipated that two other multipole components shall be prevalent in the excitation spectrum of this scatterer. It is expected that there will be accumulations of charge at the center of each '+' shaped element, due to the convergence and divergence of radially-orientated currents. At resonance, these accumulations of charge will be opposite and as such will result in a z-aligned electric dipole at the center of the T-scatterer. This will also be facilitated by z-aligned displacement currents across the center of the T-scatterer, driven by the longitudinal field component of the radially polarised beam. This electric dipole can be expected to occur simultaneously with a toroidal dipole resonance.

It is not anticipated that the magnetic multipoles will play a significant role in the excitation of the T-scatterer. This is due to the radial E-fields of the incident light and the geometry of the scatterer, which shall not facilitate the transverse currents ($\mathbf{r} \times \mathbf{J} \neq 0$) required for magnetic multipole excitation.

The characteristic dimensions of the T-scatterer (w, s and d) gives a broad parameter space to evaluate for the optimum T-scatterer configuration. Providing $s \gg w$, varying s will essentially only affect the resonant frequency of the T-scatterer. This leaves the dielectric thickness ('+' element separation) d as the most influential parameter in optimising the response scatterer.

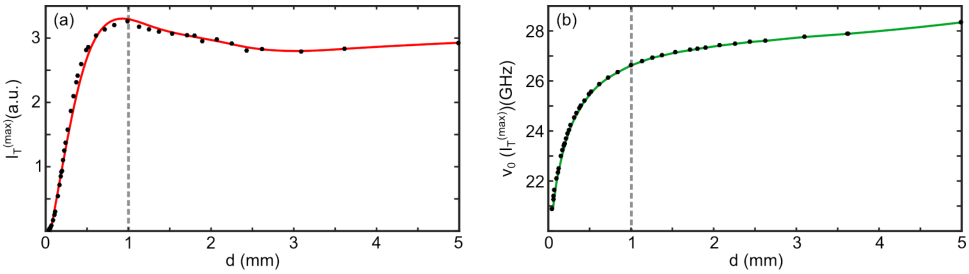

Figure 4.3: ***Optimisation of the*** T***-scatterer.*** *(a) shows the dependence of the peak scattering intensity of the toroidal dipole ($I_T^{(max)}$) excited in the T-scatterer on the thickness of the dielectric layer d. (b) shows the equivalent dependence of the resonant frequency of the toroidal dipole $\nu_0(I_T^{(max)})$. The dots indicate data points whilst the lines serve as eye guides. The d value for which the maximum toroidal dipole scattering is attained is indicated by the dotted line.*

Optimising is conducted over a range of d values: $d = \lambda/100 \rightarrow \lambda/2$ i.e. $d = 0.1 \rightarrow$ 5mm. T-scatterers with different d values are evaluated in COMSOL Multiphysics under excitation from radially-polarised light over a frequency range of $\nu = 20 \rightarrow$ 32GHz. Using the integral formulation described in Section 2.2.1, the microscopic multipoles excited in the T-scatterer can be evaluated. As a metric for the optimisation of the scatterer, the scattering power of the toroidal dipole at resonance $I_T^{(max)}$ is chosen [see Eq. 2.2.2], which we aim to maximise through varying d. This scattering intensity is normalised to the power incident on the scatterer from the incident radially polarised beam. The effect of varying d on the resonant frequency of the toroidal dipole $\nu_0(I_T^{(max)})$ is also evaluated.

The effect of d on the maximum value of the toroidal dipole scattering intensity $I_T^{(max)}$ and the resonant frequency are shown in Fig. 4.3(a) and (b) respectively. $I_T^{(max)}$ does not vary significantly as d is decreased from 5 to 1mm, approaching a maximum value for $d =$ 1mm i.e. $d = \lambda/10$. For smaller d values, $I_T^{(max)}$ drops off rapidly with decreasing separation. This can be attributed to a combination of the T-scatterer becoming two dimensional in the xy plane as $d \rightarrow 0$ [107], dissipation loss in the substrate, and the finite width of the wires [160].

The peak frequency of the toroidal dipole resonance $\nu_0(I_T^{(max)})$ on the other hand gradually decreases as d is decreased from 5 to 1mm, before decreasing rapidly as $d \rightarrow 0$. The observations presented here are in good agreement with previous results on the effect of plane separation on the toroidal dipole resonance in similar structures [161].

4.2.3 Design of electric dipole scatterer

For comparison with the toroidal T-scatterer, we construct a p-scatterer optimised for an electric dipole response when excited by radially polarised light. The p-scatterer is constructed from the elements used to create the T-scatterer. A PEC bar of length $s/2$

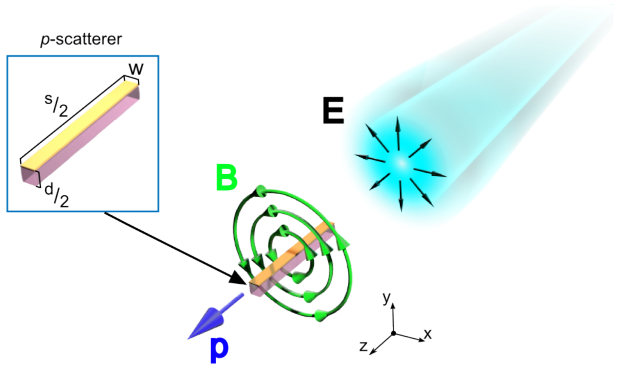

Figure 4.4: ***Schematic of the*** p***-scatterer design.*** *This figure gives a schematic of a radially polarised beam propagating along the* z *axis interacting with a p-scatterer. The expected* B *field and resultant electric dipole* p *excited on the scatterer are illustrated. The inset gives the characteristic parameters of the p-scatterer: the length* $s/2$ *and width* w *of the bar, and the dielectric thickness* $d/2$*. These parameters are given relative to those of the* T*-scatterer in Fig. 4.2.*

and width w forms the main component of the scatterer, with this corresponding to one arm of the T-scatterer. This bar should support a $\lambda/2$ resonances in the $\sim$30GHz regime i.e. $\nu_0 = 30$GHz, $\lambda_0 = 1$cm. It can be noted that in the limit of $s \gg w$, w shall not have a significant effect on the resonant frequency of the structure. The PEC bar is backed by a layer of dielectric with a thickness $d/2$. Parameters used here w, s, and d are identical to those used in the previous section for the T-scatterer, with d being chosen as 1mm, representing the optimised d value for the T-scatterer.

The p-scatterer is orientated such that its primary axis lies along the propagation direction of the radially polarised beam [Fig. 4.4]. In this orientation, the p-scatterer is not expected to couple strongly to the radially polarised component of the incident light, which is necessarily zero on-axis [Fig. 4.1]. However, radially polarised light also supports on-axis polarisation components aligned along the beam propagation axis. It is anticipated that these longitudinal polarisation components should couple strongly to the p-scatterer in this orientation, resulting in an electric dipole along the z-axis [Fig. 4.4].

This excited electric dipole shall be co-aligned with the toroidal dipole excited in the T-scatterer when under the same illumination. As such, in the ideal case both T and p-scatterers will possess an identical far-field radiation pattern, due to the identical nature of the electric and toroidal dipole radiation. This would make the two scatterers indistinguishable from an examination of the far-field radiation alone. However, it is expected that differences in the near-field coupling could manifest as differences in the frequency response of the scatterers.

The response of the p-scatterer is examined in the same manner as the T-scatterer in the previous section, across a frequency range of of $\nu = 20 \rightarrow 32$GHz.

4.3 Comparison of scatterers

Here, the T-scatterer and the p-scatterer shall be directly compared to evaluate the differences in their coupling to incident radial polarisation. This shall be done in terms of evaluation of the excited microscopic multipoles, and the far-field radiation distributions of the scatterers.

4.3.1 Multipole scattering

The multipoles excited in the optimised T and p-scatterers are computed using the integrals in Section 2.2.1 and the scattering intensity of the multipoles is evaluated from these using Eq. 2.2.2 in the same section. The multipole scattering intensities up to quadrupole order are shown in Fig. 4.5(a) and (b) for the T and p-scatterers respectively, with higher order multipoles being omitted due to their negligible contribution to the scattering. The presented scattering intensities are normalised to the power incident on the scatterers.

It is immediately clear from 4.5(a) and (b) that the resonance characteristics of the two scatterers are very different. The T-scatterer supports a sharp, narrow toroidal dipole resonance with a Q-factor of 124 at $\nu = 26.6$GHz. In contrast, the electric dipole resonance of the p-scatterer is much broader with a Q-factor of 5.

In the case of the T-scatterer [Fig. 4.5(a)], it can be seen that the toroidal dipole accounts for $\sim 96\%$ of the multipole scattering with the next most significant contributor being a non-resonant electric quadrupole. An electric dipole, aligned primarily along the z-axis of the structure is also excited at the same frequency as the toroidal dipole resonance. This can be attributed to accumulations of opposing charge at the centers of the two '+' elements and displacement currents in the dielectric. In the p-scatterer [Fig. 4.5(b)], the electric dipole accounts for $> 99\%$ of the multipole scattering. The next most dominant multipole scatterer at this resonance is the toroidal dipole. Whilst this may seem counter-intuitive considering the geometry of the scatterer, the relevance of toroidal dipoles to structures with non-toroidal geometry, such as simple wires, has been discussed in the literature [122].

The dominant toroidal dipole of the T-scatterer and dominant electric dipole of the p-scatterer are directly compared in Fig. 4.5(c). This emphasises the difference in Q-factor of the two resonances. Furthermore, at their respective resonances, the toroidal dipole scattering from the T-scatterer is ~ 4 times greater than the electric dipole scattering from the p-scatterer. This indicates that radially polarised light couples significantly more strongly to a T-scatterer than a p-scatterer.

The dominance of the multipoles excited in the respective scatterers can be further emphasised by considering the field distributions in the near-field of the scatterers

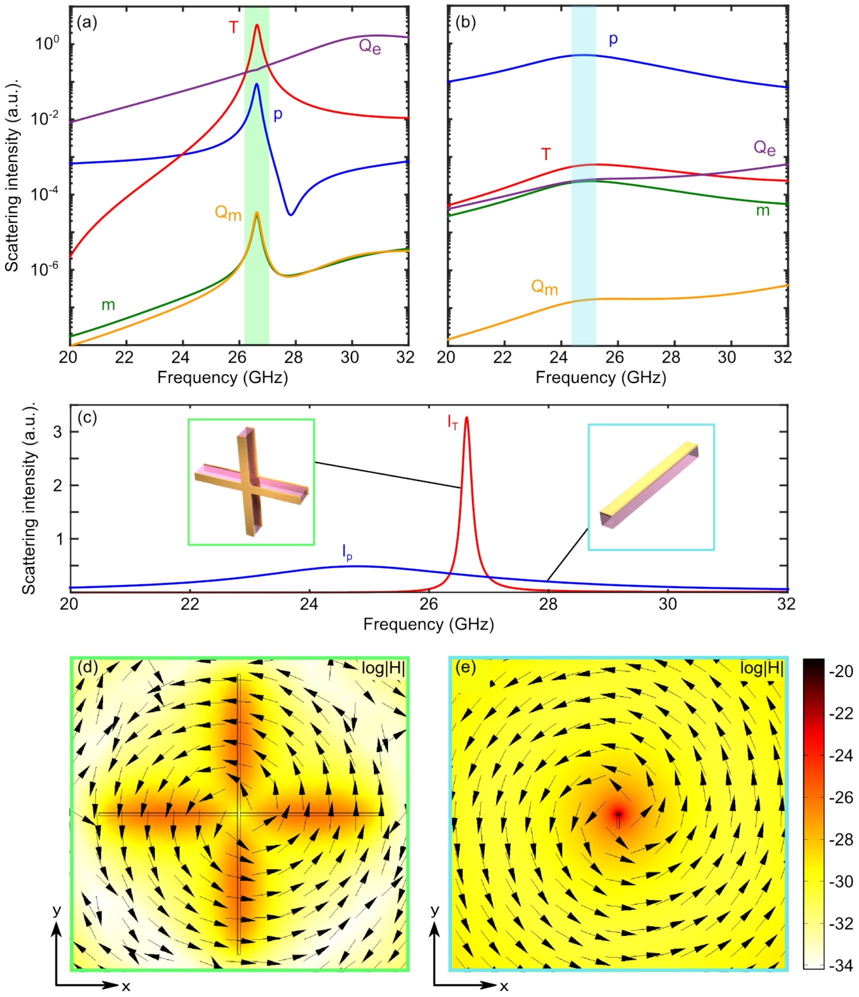

Figure 4.5: ***Excited multipoles and near-field of the*** T ***and*** p***-scatterers.*** *(a) and (b) show the multipole scattering intensities up to quadrupole order for the* T *and p-scatterers respectively for a dielectric thickness d of 1mm. The green and blue boxes indicate the resonant positions of the toroidal and electric dipole respectively. (c) directly compares the dominant multipole resonances excited on each scatterer, these being the toroidal dipole for the* T *scatterer and the electric dipole for the p-scatterer. (d) and (e) show the near-field distribution of the magnetic field around the* T *and p-scatterers respectively, with the arrows giving the vector orientation of the field.*

[Fig. 4.5(d) and (e)]. Both T and p-scatterers show a magnetic field distribution in teh azimuthal direction around the scatterer, as expected for an electric or toroidal dipole excitation. However, it can be seen that in Fig. 4.5(d), the intensity of the magnetic field decays rapidly outside the confines of the T-scatterer, which illustrating the weak coupling to the environment suggested by the high Q-factor resonance. Such confinement of the azimuthal magnetic field is a clear indicator of a toroidal dipole excitation, supporting the multipole scattering intensity analysis in Fig 4.5(a). In contrast, in Fig. 4.5(e) the magnetic field extends far from the p-scatterer, corroborating the evidence for a dominant electric dipole excitation.

4.3.2 Far-field radiation

As already noted in Section 2.1.3, the far-field radiation patterns of the electric and toroidal dipoles are identical. Therefore, we anticipate that the far-field radiation patterns of the T and p-scatterers at resonance should be near identical, despite the microscopic origin of this radiation being two fundamentally different excitations. To verify this, we use the excited currents to reconstruct the radiated E and B-fields, and Poynting vector $\mathbf{S}$ of the p and T-scatterers at their respective resonances.

From Fig. 4.5(a) and (b), the key excitation components of the T-scatterer are the toroidal dipole T, electric dipole p, and electric quadrupole Q. The p-scatterer additionally has a non-negligible magnetic dipole m component. As such, these multipole components are used to reconstruct the radiation patterns of the scatterers in order to characterise the perturbing effects of the non-dominant multipoles on the dominant dipole radiation.

In the far-field, the radiated electric fields for p, m, T, and Q in the far-field are given by the following equations:

$$\mathbf{E}_p(\mathbf{r}) = \frac{k^2 c}{4\pi}\sqrt{\frac{\mu_0}{\epsilon_0}}\left(\frac{e^{ikr}}{r}\right)(\hat{\mathbf{r}}\times\mathbf{p})\times\hat{\mathbf{r}}, \tag{4.4}$$

$$\mathbf{E}_m(\mathbf{r}) = -\frac{k^2 c}{4\pi}\sqrt{\frac{\mu_0}{\epsilon_0}}\left(\frac{e^{ikr}}{r}\right)(\hat{\mathbf{r}}\times\mathbf{m}), \tag{4.5}$$

$$\mathbf{E}_T(\mathbf{r}) = \frac{ik^3 c}{4\pi}\sqrt{\frac{\mu_0}{\epsilon_0}}\left(\frac{e^{ikr}}{r}\right)(\hat{\mathbf{r}}\times\mathbf{T})\times\hat{\mathbf{r}}, \tag{4.6}$$

$$\mathbf{E}_Q(\mathbf{r}) = \frac{-ik^3 c}{24\pi}\sqrt{\frac{\mu_0}{\epsilon_0}}\left(\frac{e^{ikr}}{r}\right)(\hat{\mathbf{r}}\times\mathbf{Q})\times\hat{\mathbf{r}}. \tag{4.7}$$

A full derivation of these radiated fields is given in Appendix B. The radiated magnetic fields can be readily obtained from these using [9]:

$$\mathbf{H} = \sqrt{\frac{\epsilon_0}{\mu_0}}\hat{\mathbf{r}}\times\mathbf{E}. \tag{4.8}$$

The radiation pattern can be evaluated from the radial component of the time-averaged Poynting vector $\mathbf{S}$ [9]:

$$S_r = \frac{1}{2}\left(\mathbf{E}\times\mathbf{H}^*\right)_r, \tag{4.9}$$

Where $\mathbf{E}$ and $\mathbf{H}$ are summations of the individual multipole electric and magnetic fields.

The Poynting vector is evaluated for both T and p scatterers at a on a sphere of radius $r = 1$m, which can be considered the far-field given the mm-scale of the scatterers.

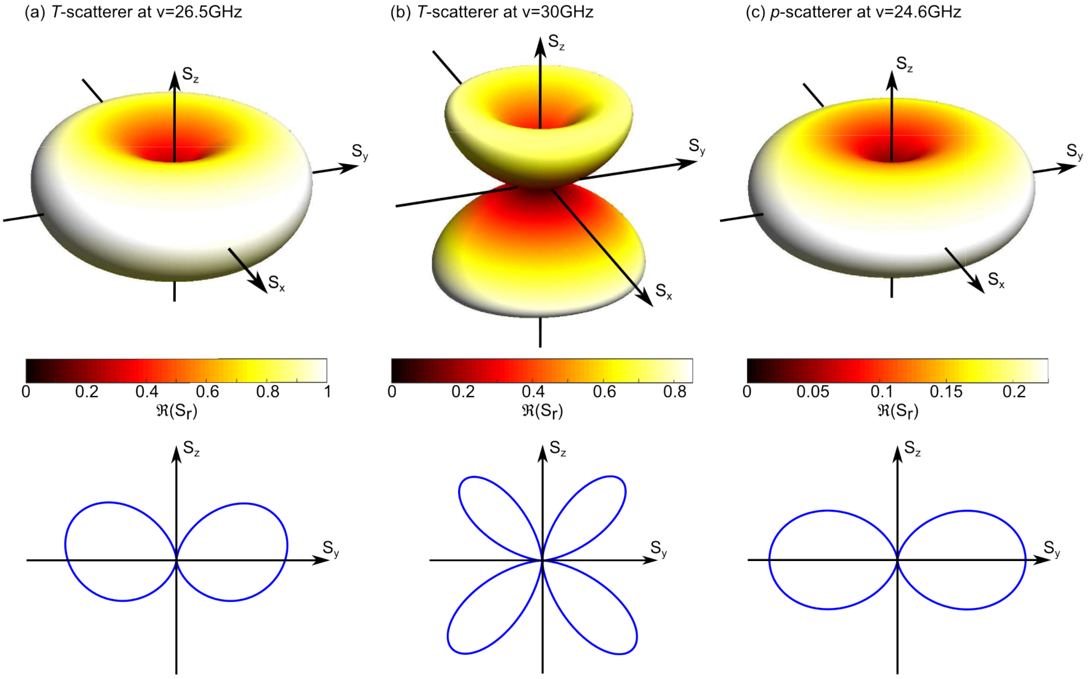

Figure 4.6: ***Far-field radiation patterns of the*** T ***and*** p***-scatterers.*** *This figure illustrates the radiation distributions of the* T *and* p*-scatterers given in terms of the radial component of the Poynting vector* $\Re(S_r)$ *at a radial distance of 1m from the respective scatterers. The upper panels depict the full three dimensional radiation patterns in terms of* S_x*,* S_y*, and* S_z*, whilst the lower panels give the cross-sections at* $S_x = 0$*. (a) shows the far-field radiation distribution emitted from the* T*-scatterer at the toroidal dipole resonance* $\nu_0(I_T^{(max)}) = 26.6$*GHz.(b) shows the far-field radiation distribution emitted from the* T*-scatterer off-resonance at* $\nu = 30$*GHz. (c) shows the far-field radiation distribution emitted from the* p*-scatterer at the electric dipole resonance* $\nu_0(I_p^{(max)}) = 24.6$*GHz. All values are normalised to the maximum value of* $\Re(S_r)$ *for the* T*-scatterer.*

The real part of the radial Poynting vectors $\Re(S_r)$ are plotted in Fig. 4.6. The radiation pattern of the T-scatterer is evaluated both at the toroidal dipole resonance ($\nu = 26.6$GHz) [Fig. 4.6(a)] and off-resonance ($\nu = 30$GHz) [Fig. 4.6(b)] where the electric quadrupole has become the dominant excitation. In the case of the p-scatterer, the electric dipole is dominant across the full frequency range considered, and so the radiation pattern is only evaluated at resonance ($\nu = 24.6$GHz) [Fig. 4.6(c)].

For the T-scatterer [Fig. 4.6(a)] at resonance, the doughnut-like radial Poynting vector distribution is typical of dipole radiation, as expected owing to the dominance of a z-aligned toroidal dipole at resonance [Fig. 4.5(a)]. We note that there exists a slight asymmetry to the radiation distribution, with a slight bias towards the positive S_z direction. This can be attributed to contributions from the non-resonant electric quadrupole, which slightly perturb the dominant dipole radiation. Owing to the high Q-factor of the toroidal dipole resonance, the T-scatterer only exhibits dipole-like radiation across a narrow frequency range. Outside of this frequency range, the electric quadrupole becomes the dominant excitation [Fig. 4.5(a)], leading to a typical quadrupole radiation pattern when the T-scatterer is off-resonance [Fig. 4.6(b)]. For the p-scatterer [Fig.4.6(c)], the observed radiation distribution is electric dipole in character, as expected from the scattering intensity analysis [Fig. 4.5(b)]. We note that all radiation patterns are symmetric about the ϕ direction to within noise levels.

From this analysis, it can be said that the two scatterers would be very difficult to distinguish in the far-field by their radiation patterns alone. However, the two scatterers can be identified by an examination of their frequency response, which is radically different for the two examined scatterers.

4.4 Summary

The T-scatterer exhibits a significantly higher quality resonance that couples more strongly to the incident field than the broadband p-scatterer resonance. This is can be examined in the context of antennas. In general, an electric dipole antenna is limited in both minimum [162–164] and maximum [165] Q-factor, with the geometry of the configuration being the primary consideration. Work by Hazdra et al [165] demonstrates that, for a $\frac{w}{\lambda}$ ratio of $\sim 4.1 \times 10^{-3}$ as in the case of our p-scatterer, the maximum Q-factor is ~ 4.7. This is in good agreement with our simulations [Fig. 4.5(c)], with discrepancies arising due to our choice of a 2D rather than 3D wire. The T-scatterer design using the same thickness of wire however, can substantially surpass this Q-factor limitation by a factor of 25, whilst maintaining an identical far-field radiation pattern. As such, we present the interaction between radially polarised light and toroidal scatterers as a means of achieving a far-field electric dipole radiation pattern that exceeds the conventional limitations on Q-factor.

The work presented here demonstrates the benefits of matching the topology of the illuminating light to the topology of the scatterer, a topic which we shall expand upon in the following chapter. It is explicitly demonstrated that the toroidal dipole couples strongly to radially polarised light. This could be expanded upon by considering more complex vector beams, for example beams with orbital angular momentum.

Chapter 5

The “focused doughnut” pulse

5.1 Introduction

In this chapter, we move from discussing toroidal excitations in matter to discussing propagating toroidal excitations in free-space. Specifically, these propagating toroidal excitations are exact pulse solutions to the homogeneous Maxwell’s equations introduced by Hellwarth and Nouchi in 1996 [20] and are known as“focused doughnut” pulses.

Conventionally, free-space electromagnetic propagation is described in terms of plane-waves i.e. non-diffracting infinite energy solutions to Maxwell’s equations [9], or diffracting beams such as Gaussian beams, which are solutions to the paraxial form of Maxwell’s equations in free-space [166]. In 1983 however, Brittingham introduced the concept of focus wave modes - exact three-dimensional solutions to Maxwell’s equations representing localised transmission of electromagnetic energy through free-space [167]. It was anticipated that the creation of such electromagnetic pulses would lead to a variety of novel applications based on complex light-matter interactions. These include infinite depth-of-field microscopes, low-loss power transmission, secure communications, remote sensing and directed energy weapons [124]. From a theoretical standpoint, a full description of localised EM energy transmission would satisfy Brittingham’s original goal of obtaining a classical description of a photon i.e. a finite energy solution to Maxwell’s equations exhibiting wave-particle duality [124, 167].

Since Brittingham’s original work on the concept of focus wave modes in 1983 [167], many families of pulses that satisfy the criteria for localised transmission of electromagnetic energy have been theoretically identified. Broadly speaking, these pulses remain diffractionless and localised over large distances of propagation, are space-time non-separable and possess a wide range of novel properties, such as complex field geometry, explicit single cycle nature, and spatiotemporal transformations [20, 168]. Our key interest lies in the *electromagnetic directed energy pulse train* (EDEPT) family of solutions introduced by Ziolkowski in 1989 [124], of which the “focused doughnut” pulse is a member.

The primary interest in the “focused doughnut” pulse stems from its direct topological similarities to the localised toroidal excitations in matter, characterising it as a free-space analogue of the toroidal multipoles. This similarity is anticipated to manifest as preferential excitation of toroidal modes in light-matter interactions involving “focused doughnut” pulses, which could be exploited for spectroscopy, sensing and communication applications.

Although the field of localised pulses has recieved significant theoretical discussion, experimental realisation has been limited. Demonstration of X-shaped pulses [169] and Airy-Bessel pulses [170] have been some of the first successes. However, experimental realisations of the EDEPT solution family, including the “ focused doughnut” pulse, have remained elusive with research confined to qualitative discussion [168, 171–173], preliminary work [174], analogies with observed terahertz pulses [175–178] and acoustic analogues [179, 180]. As such, the research presented here aims to lay a foundation for an experimental realisation of the “focused doughnut” pulses, in addition to highlighting their light-matter interactions that may be relevant to future applications.

In this chapter, a thorough theoretical background for the “focused doughnut” pulse shall be given, with its key properties identified and investigated. It shall be demonstrated that these pulses can be effectively simulated in commercial simulation software. Finally, the interactions of these pulses with continuous and particulate matter shall be numerically investigated, with particular attention to drawn to their coupling to toroidal modes in matter.

5.2 History of localised electromagnetic pulses

5.2.1 Conventional solutions to the electromagnetic wave equation

The form of free-space, source-free EM fields is determined by solving Helmholtz’s wave equation:

$$\left(\nabla^2 - \frac{1}{c^2}\frac{\partial^2}{\partial t^2}\right) f(\mathbf{r}, t) = 0, \tag{5.1}$$

Plane waves of the form $e^{i(kr-\omega t)}$ are the simplest solution to the wave equation, but are non-physical due to their infinite spatial extent and thus infinite energy [9]. Plane waves however are useful approximations in cases where the wavelength is significantly larger than the region of interest, or when the region of interest is suitably far from a source, where wavefront curvature can be neglected. Solutions that are more useful for describing real phenomena, particularly in the context of optics and laser physics, can be found by adopting the paraxial approximation of the Helmholtz equation, which assumes the longitudinal distribution of a wave pulse is slowly varying compared to the wavelength. This leads to wave solutions in the form of Gaussian and paraboloidal beams/pulses [9].

5.2.2 Localised electromagnetic beams and pulses

The search for localised electromagnetic beams and pulses was motivated by the phenomenon of diffraction, which significantly affects the transverse profile of conventional beams and pulses when propagating [166]. A Gaussian beam for instance with width at waist of order one wavelength, will have doubled it's width after propagation of only a few wavelengths. It was generally believed that the plane wave was the only waveform free of diffraction [166].

In 1941 Stratton introduced a monochromatic solution to the wave equation with a transverse profile defined by a Bessel function [181]. This solution was known as a Bessel beam and can be thought of as a series of plane waves propagating with non zero radial wavevectors k_r. This property means an ideal Bessel beam can propagate for an infinite distance without undergoing diffraction and will also possess self healing properties if the path of the beam is interrupted.

However, an ideal Bessel beam requires an infinitely wide aperture to be created and thus possesses infinite energy [166]. Approximations of Bessel beams can be produced experimentally by use of an axicon with a truncated finite aperture [166, 184, 185]. It was found that the beam could travel approximately 28 times further than a Gaussian beam before its transverse intensity peak is appreciably changed [166, 184], representing a real example of a non-diffracting beam. Bessel beams have since been produced from several mechanisms such as computer generated holograms [186, 187] and transformation optics waveguides [188], and have been found particularly useful for optical tweezer applications [189]. Other diffractionless beams, such as Mathieu beams [190, 191], which are comparable to Bessel beams have also been introduced.

In the same way that plane waves can form a basis function to synthesise Gaussian beams and pulses, Bessel beams can be used to synthesise further types of pulses. This has given rise to the so-called X-wave solutions to the wave equation, which are formed by a superposition of Bessel beams with the same phase velocity (i.e. same axicon angle) [Fig. 5.1(a)] [166, 169, 192] formed by a summation of Bessel beams. These represent some of the first examples of truly localised wave packets being experimentally realised [169] and have shown interesting properties such as propagation through dispersive media without distortion [192].

Recently there has been significant interest in combining Bessel beams with a variety of pulse envelopes as a means of achieving localised wavepackets. Much interest has been given to Airy profiles for beams, which have already attracted considerable interest due to properties of finite energy and the ability to accelerate along arbitrary trajectories

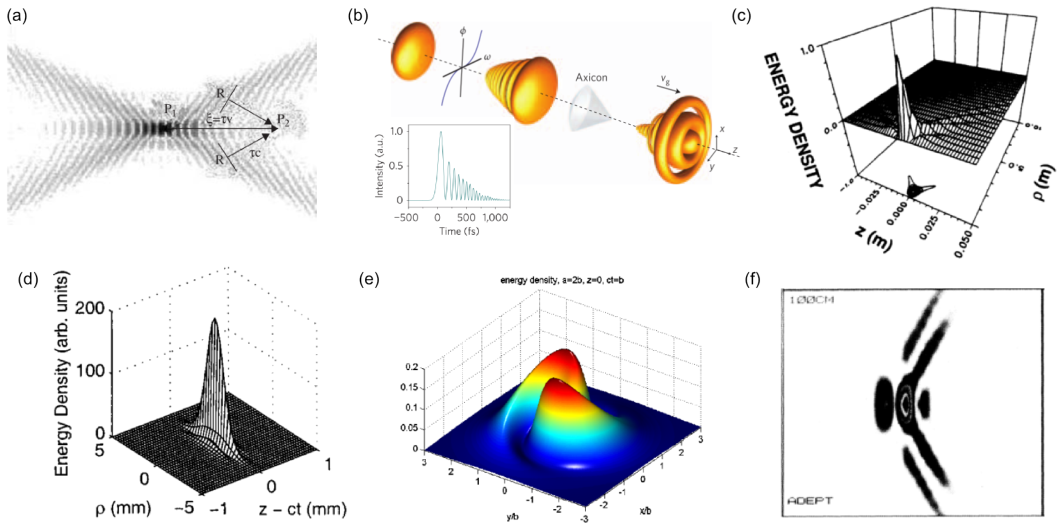

Figure 5.1: ***Examples of localised pulses.*** *This figure gives some examples of localised pulse solutions that have been examined in the literature, either experimentally or numerically. (a) shows the field of a localised X-shaped pulse formed by a superposition of Bessel beams. Figure adapted from [166]. (b) illustrates the construction of a localised Airy-Bessel wave packet, with a transverse Bessel profile and temporal Airy profile. Figure adapted from [170]. (c) depicts the first theroetically-identified EDEPT pulse solution, known as the modified power spectrum pulse. Figure adapted from [124]. (d) gives a further example of an EDEPT pulse solution, this one known as the “focused pancake” pulse. Figure adapted from [182]. (e) shows an EDEPT pulse solution constructed with an azimuthal dependence, that gives the pulse a non-zero angular momentum. Figure adapted from [183]. (f) shows an ultrasonic localised acoustic pulse generated in water by a synthetic line array. Figure adapted from [179].*

[193, 194]. Using a combination of phase masks and axicons, Airy-Bessel light pulses can be produced that represent localised wavepackets that are non significantly affected by either diffraction or dispersion due to their self-healing properties [Fig. 5.1(b)] [170]. Other types of pulse based on this methodology have also been considered, such as Gauss-Bessel, Airy-Gauss, and Airy-Airy pulses [193, 195].

5.2.3 Focus wave modes and electromagnetic directed energy pulse train (EDEPT) solutions

In this section, the methodology introduced by Brittingham and extended by Ziolkowski for constructing localised finite energy pulse solutions to Maxwell’s equations shall be discussed in detail. This methodlogy forms the theoretical basis for the construction of the “focused doughnut” pulse.

In Brittingham’s 1983 paper on focus wave modes [167], the criteria for a 3D, non-dispersive, source-free, classical EM pulse are written as follows:

1. **Must satisfy the homogenous Maxwell’s equations**

2. **Be continuous and non-singular**
3. **Have a 3D pulse structure**

   i.e. functional values fall off in all directions from the moving pulse centre.

4. **Be non-dispersive for all time**

   i.e. the pulses’ envelope shape remains unchanged after propagation.

5. **Move at light velocity in straight lines**
6. **Carry finite energy**

The final requirement ensures that any resultant pulse forms are practical and applicable. Brittingham’s pulse solutions were subsequently shown not to satisfy this crucial final condition [196]. It was shown by Ziolkowski that Brittingham’s original focused wave mode solutions represent modified Gaussian pulses [124, 197]. The form of this pulse is given below:

$$\phi_k(\mathbf{r}, t) = \frac{e^{(-k\rho^2/V)}}{4\pi i V} e^{ik(z+ct)}, \tag{5.2}$$

Where $1/V = 1/A - i/R$, $A = z_0 + \tau^2/z_0$, $R = \tau + z_0^2/\tau$ and $\tau = z - ct$. A represents the pulse spread and R represents the radius of curvature of the phase fronts. The parameter z_0 represents the complex source location of the pulse at $(\rho, \tau) = (0, iz_0)$ [197]. This is known as the *moving, modified Gaussian pulse* (MMGP). It is immediately clear that the presence of both $z + ct$ and $z - ct$ terms in the equation for the MMGP means this pulse is bidirectional. In fact, generalised solutions to the scalar wave equation can be expressed in terms of such bidirectional functions [166]. A superposition of forward propagating Bessel beam modulated by backwards propagating plane waves is such a decomposition [166]. Work such as that by Ziolkowski [124], demonstrated that localised pulse solutions could be ‘tweaked’ to ensure that the backwards propagating components of the pulse are negligible, and only the forward propagating components contribute to the resultant pulse.

The MMPG propagates through space with only local deformations but possesses infinite energy. The same conclusions were drawn for extensions of the MMPG utilising Hermite [198] and Laguerre [199] polynomials, analogous to conventional Hermite-Gaussian and Laguerre-Gaussian modes. However, it was realised by Ziolkowski that the fundamental MMGP can be used as a basis equation to form new transient solutions to the scalar wave equation (equation 5.1) [124]. Due to the localised nature of the MMGP, it is clear that it is better suited for describing directed EM energy transmission than plane wave summations using the conventional Fourier approach [124].

Transient solutions are achieved by integration of the basis functions over a carefully chosen weighting function $F(k)$:

$$f(\mathbf{r}, t) = \int_0^\infty \phi_k(\mathbf{r}, t) F(k) dk. \tag{5.3}$$

By integration of equation (5.3) with the *modified power spectrum* (MPS) chosen as $F(k)$, the wave equation solution known as the MPS pulse can be found:

$$f(\boldsymbol{r}, t) = f_0 \frac{e^{-s/q_3}}{(q_1 + i(z - ct))(s + q_2)^\alpha}, \tag{5.4}$$

Where:

$$s = \frac{\rho^2}{(q_1 + i(z - ct))} - i(z + ct). \tag{5.5}$$

The parameters q_1, q_2 and q_3 are all real and adjustable with dimensions of length and f_0 and α are real, dimensionless constants [124]. It is reported by Hellwarth and Nouchi that the parameters q_1 and q_2 are, respectively, measures of the wavelength and focal region depth of these EDEPT solutions [20]. The MPS pulse satisfies all of the aforementioned localised pulse criteria set out by Brittingham [167], in particular, the finite energy requirement [124].

By chosing the values of these parameters, multiple localised pulses can be constructed. Ziolkowski initially used the constraints $q_1 \ll q_3 \ll q_2$ and $\alpha = 1$ in his analysis of the MPS pulse [124]. This was expanded on by Hellwarth and Nouchi, and subsequently by Feng et al, who used the constraints $q_1 \ll q_2$, $\alpha = 1$ and $q_3 \to \infty$ [20, 168]. The MPS pulse was further extended in work by Lekner, who introduced azimuthal dependence of the form $e^{im\phi}$, where m is some positive or negative integer, to the previously axisymmetric pulse. This led to an analysis of azimuthally dependent [200] and helical [183] localised light pulses. This was the first case of localised pulse with orbital angular momentum.

Localised $\mathbf{E}$ and $\mathbf{H}$ pulse fields can then be formed from the MPS by constructing a Hertz vector, and subsequently vector potential $\mathbf{A}$, from $f(\boldsymbol{r}, t)$ [20,124,168] as shown in Eq. 5.6:

$$\mathbf{A}(\mathbf{r}, t) = \mu_0 \nabla \times (\hat{\mathbf{n}} f(\mathbf{r}, t)), \tag{5.6}$$

Where $\hat{\mathbf{n}}$ is some arbitrary unit vector. The choice of direction of this Hertz vector allows for a wide variety of pulses to be constructed in this regime. Cases of Hertz vectors parallel to [20,124] and transverse to [168,182] the propagation axis have been considered.

5.2.4 Examples of EDEPT solutions

Through the methodology in the previous section, the choice of parameters values and the alignment of the Hertz vector allows for an arbitrary number of solutions to Maxwell’s equations to be synthesised (although not without some algebraic effort).

The first of these was Ziolkowski’s MPS pulse solution from the original paper, with $q_1 \ll q_3 \ll q_2$ and $\alpha = 1$, and a Hertz vector aligned along the direction of propagation [Fig. 5.1(c)]. Key general properties of the EDEPT solutions were identified from this pulse, such as the single cycle nature, broadband spectrum, and energy localisation [124]. The “focused doughnut” pulses, which are the key topic of this chapter, were introduced by Hellwarth and Nouchi shortly afterwards [20] and shall be addressed in detail in the next section. ”Focused pancake” pulses were introduced by Feng et al, so named due to their transverse extent far exceeding the longitudinal extent [Fig. 5.1(d)]. These pulses were analysed extensively particularly in terms of their spatiotemporal evolution, revealing the field transformations that EDEPT solutions undergo during propagation [168, 182]. This shall be discussed further in Section 5.3.1.

The parameter space for the EDEPT solutions was extended by Lekner, by introducing azimuthal dependence of the form $e^{im\theta}$, giving localised pulses with angular momentum as well as with circular polarisation [Fig. 5.1(e)] [183, 200, 201].

It can be noted that Ziolkowski identified that their could be acoustic analogues of the EDEPT solutions (known as ADEPT solutions) that could be synthesised experimentally in the ultrasound regime [Fig. 5.1(f)] [179, 180, 202]. Many potential generation schemes for EDEPT pulses have been suggested, and these shall be discussed in more detail in Chapter 6.

5.3 Properties of the “focused dougnut” pulse

The “focused doughnut” pulse was first established as an exact solution to the homogeneous Maxwell’s equations by Hellwarth and Nouchi [20]. They followed the procedure established by Ziolkowski to create localised finite-energy pulses through a superposition of MMGPs with a weighting function given by the MPS (see Section 5.2.3). As illustrated by Eq. 5.4 and 5.5, the MPS pulse that arises as a result of this summation is characterised by four parameters: q_1, q_2, q_3, and α, which can be freely chosen. Hellwarth and Nouchi chose the following constraints in their analysis: $q_1 \ll q_2$, $q_3 \to \infty$, and $\alpha = 1$. Following Eq. 5.6, the vector potential for this pulse can be constructed by choosing an alignment for the Hertz vector. Here Hellwarth and Nouchi chose $\hat{\mathbf{n}} \to \hat{\mathbf{z}}$ i.e. a Hertz vector aligned along the direction of propagation.

With this choice of parameters, the field equations for a torus shaped pulse known as a “focused doughnut” can be constructed. The fields for the TE “focused doughnut”

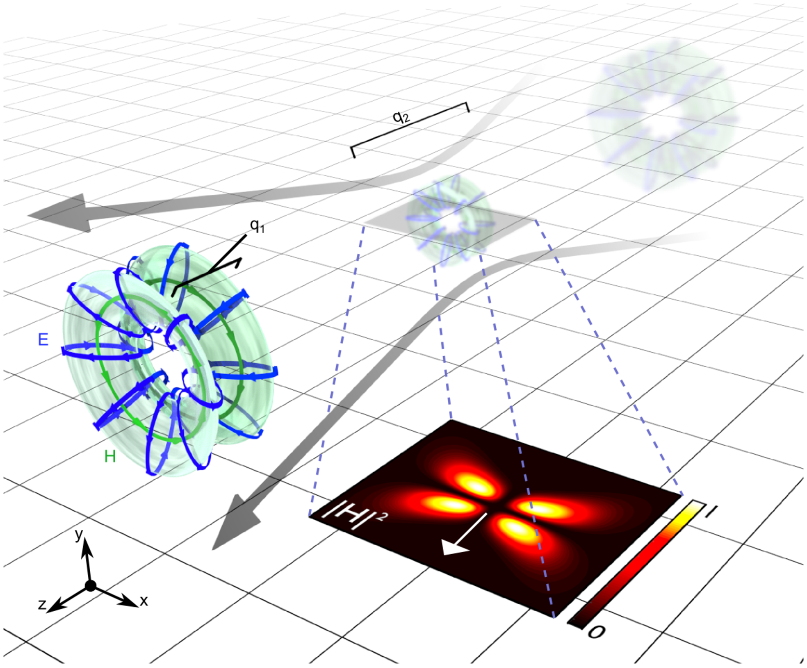

Figure 5.2: ***3D schematic of “focused doughnut” pulses.*** *This figure gives a full artistic representation of a TM focused doughnut pulse propagating from right to left. Here, the magnetic field H is azimuthally polarised and confined in a torus-shaped region, and the electric field E is winding along the meridians of the torus, resulting in a longitudinal component at the centre of the pulse. The projected cross-section illustrates the confinement of the pulse energy in two adjacent toroidal regions, and the white arrow indicates the propagation direction.*

pulse solutions from Ref. [20] are given below:

$$E_\theta = -4if_0\sqrt{\frac{\mu_0}{\epsilon_0}}\frac{\rho\left(q_1+q_2-2ict\right)}{\left[\rho^2+\left(q_1+i\tau\right)\left(q_2-i\sigma\right)\right]^3}, \tag{5.7}$$

$$H_\rho = 4if_0\frac{\rho\left(q_2-q_1-2iz\right)}{\left[\rho^2+\left(q_1+i\tau\right)\left(q_2-i\sigma\right)\right]^3}, \tag{5.8}$$

$$H_z = -4f_0\frac{\rho^2-\left(q_1+i\tau\right)\left(q_2-i\sigma\right)}{\left[\rho^2+\left(q_1+i\tau\right)\left(q_2-i\sigma\right)\right]^3}, \tag{5.9}$$

Where $\tau = z - ct$, $\sigma = z + ct$ and f_0 is a real constant. The complementary TM fields can be constructed using the identities:

$$\mathbf{E}_{TM} = \sqrt{\frac{\mu_0}{\epsilon_0}}\mathbf{H}_{TE}, \tag{5.10}$$

$$\mathbf{H}_{TM} = -\sqrt{\frac{\epsilon_0}{\mu_0}}\mathbf{E}_{TE}. \tag{5.11}$$

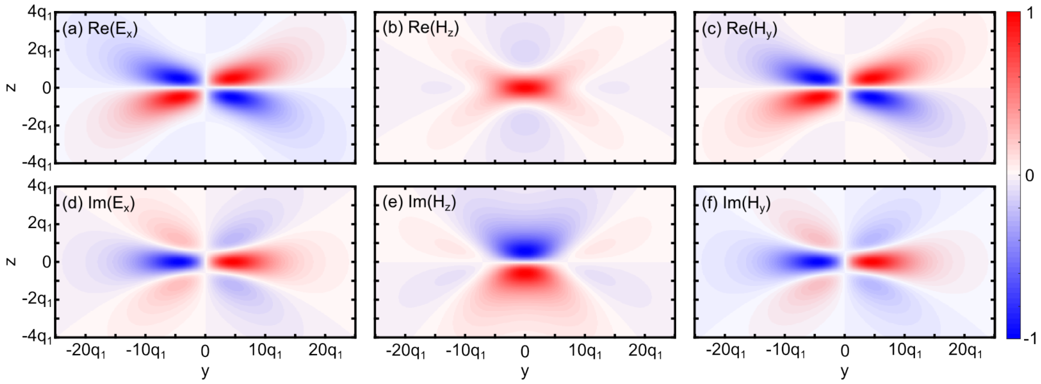

Figure 5.3: ***Field structure of at TE "focused doughnut" pulse.*** *This figure shows the field topology on a yz plane at $x = 0$ of a TE FD pulse at focus (t=0). (a) shows the transverse electric field E_x, (b) shows the longitudinal magnetic field H_z, and (c) shows the in-plane magnetic field H_x of the real part of the TE pulse. (d) to (f) show the analogous fields for the imaginary part of the TE pulse. The characteristic parameters of the FD pulse in all cases are $q_2 = 100q_1$. All plots are generated from the analytical form of the FD pulse [Eq. 5.7-5.9] and are normalised to their maximum values.*

The parameters q_1 and q_2 are found to represent respectively the effective wavelength of the pulse and the focal region depth. Beyond the focal region ($|z| > q_2$), the FD diffracts in the same manner as a Gaussian pulse with wavelength q_1 and Rayleigh length q_2. The azimuthal electric field in Eq. 5.7 forms closed loops that are zero valued on axis. The magnetic field components [Eqs. 5.8 and 5.9] form closed loops around the electric field, forming the meridians of a torus structure. The field along the meridians of the torus results in strong longitudinal field component on axis due to the increase in field density within the centre of the torus. Further separating the real and imaginary parts of Eqs. 5.7-5.9 yields two families of pulses which independently satisfy Maxwell's equations. These correspond to a $1\frac{1}{2}$ cycle and a single cycle pulse respectively, which is as defined by the behaviour of the on-axis field in the vicinity of focus. It is key to identify that Eqs. 5.7-5.9 cannot be separated into separate functions of only spatial and only temporal variables. The spatial and temporal components of the pulse are inherently coupled rendering the pulse space-time non-separable.

A full 3D schematic of a "focused doughnut" pulse with respect to its characteristic parameters q_1 and q_2 is given in Fig. 5.2 early illustrating the toroidal topology and few-cycle nature of the pulse as it evolves through focus.

Eqs. 5.7-5.9 are plotted out explicitly in Fig. 5.3 along a yz cross-section for pulse parameters $q_2 = 100q_1$at a time t=0 i.e. in the region of focus. Both the real and imaginary components of the field equations are depicted, which clearly illustrates the distinction between the $1\frac{1}{2}$ cycle and a single cycle pulses. It can be seen that a single ($1\frac{1}{2}$) cycle azimuthal and radial field will correspond to a $1\frac{1}{2}$ (single) cycle longitudinal field. As expected, the longitudinal field component of FD pulses is the only component that is non-zero at $\rho = 0$. The energy density $\left(\mu_0 H^2 + \epsilon_0 E^2\right)$ drops off polynomially with r, decaying as r^{-8} for the real pulse and r^{-10} for the imaginary pulse, at the point of maximum focus $(z = 0, t = 0)$. Both real and imaginary FD solutions have been shown to possess equal and finite total energy [20].

5.3.1 Spatiotemporal evolution

It is worth discussing further the spatiotemporal evolution of the FD pulse families. The definition for the 'long' and 'short' cycle pulses is only valid for the $z \gg q_1$ limit, and is ambiguously defined with relation to the pulse parameter q_2, which represents an effective focal region depth. Analysis of the field equations reveals that both the real and imaginary pulses are subject to pulse transformations between the single and $1\frac{1}{2}$ cycle pulse forms as they propagate through the focus over a distance of q_2.

This is clearly illustrated in Fig. 5.4, which shows traces of the (a) real and (b) imaginary azimuthal electric field E_θ at a radius of $\rho = 5q_1$ for five different propagation distances along the z axis. In the case of the real FD pulse, the form of the pulse evolves from $1\frac{1}{2}$ cycle at $z = -q_2/2$ to single cycle at $z = 0$, and returning to $1\frac{1}{2}$ cycle as it propagates out to $z = q_2/2$. The complementary transformation occurs for the imaginary FD pulse, changing from single → $1\frac{1}{2}$ → single over the q_2 propagation distance.

Similar pulse transformations have been described for other members of the EDEPT family, such as the "focused pancake" pulses described by Feng et al [168,182]. Experimental work has also demonstrated similar behavior for single cycle Gaussian pulses in the Terahertz domain [175]. These transformations can be understood in terms of the Gouy phase shift of the focus wave modes, which lead to significant temporal reshaping [168,182].

5.3.2 Fourier decomposition

As a result of their few-cycle nature, FD pulses are considered to be ultra–broad bandwidth pulses. Hellwarth and Nouchi give a far-field $(z \gg q_2)$ approximation for the Fourier spectra of a real FD in their original paper:

$$F'_\omega = \left(\frac{i\pi\mu_0 f_0 \omega \left|\omega\right| sin\psi}{2rc^2}\right) e^{(i\omega r - |\omega| Q)/c}, \tag{5.12}$$

Where $Q = (q_1 + q_2 - (q_2 - q_1)cos\psi)/2$, and ψ is the polar angle. The equivalent Fourier spectrum for the imaginary pulse is formed by $F''_\omega = (i\omega/\left|\omega\right|)F'_\omega$ [20], though this does not affect the magnitude. However, we seek to evaluate the Fourier spectrum

(a) Real pulse

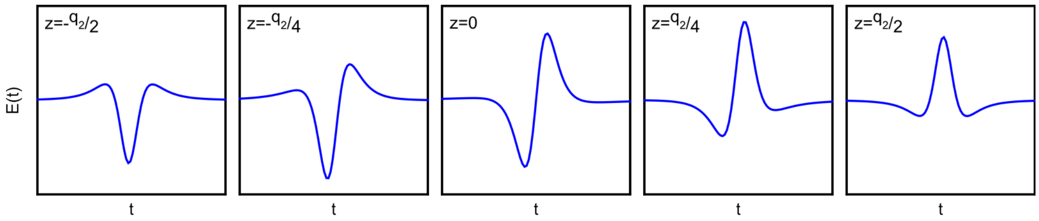

(b) Imaginary pulse

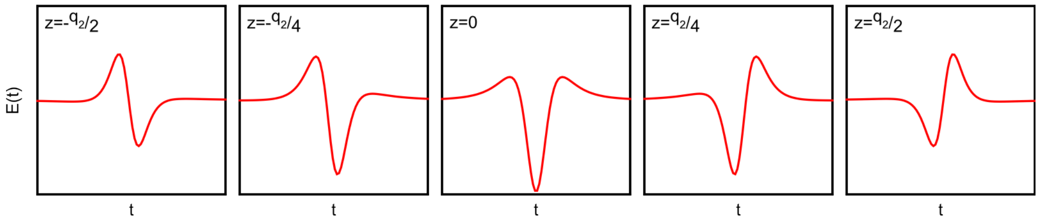

Figure 5.4: ***Spatiotemporal evolution of “focused doughnut” pulses.*** *This figure illustrates the spatiotemporal evolution of both the (a) real and (b) imaginary “focused doughnut” pulses of $q2 = 100q_1$ as they propagate over a distance of q_2 i.e. effective focal region depth from $z = -q_2/2 \rightarrow q_2/2$. All plots show traces of the azimuthal electric field E_θ at a radius of $\rho = 5q_1$, with each plot spanning a time of $t = 9q_1/c$ centred on the pulse. Spatiotemporal evolution is shown at 5 spatial points to illustrate the transitions between single and $1\frac{1}{2}$ cycle nature.*

of the FD pulse in the region of focus $(z = 0, t = 0)$ using a numerical analysis. We consider a TE FD pulse with characteristic parameters $q_2 = 100q_1$ and conduct a Fourier decomposition from the azimuthal electric field E_θ.

Fig. 5.5(a) shows the intensity of the calculated Fourier spectrum as a function of frequency ν and radial position ρ. A number of intriguing properties of the FD pulse can be inferred from the Fourier decomposition. It is clear that owing to the space-time non-separability of the pulse, the Fourier spectrum is strongly dependent on radial position ρ. This is emphasised in Fig. 5.5(b) which plots cross-sections of Fig. 5.5(a) at four different values of ρ. It can be seen that in the region of small ρ, high frequency components are more prevalent. As ρ increases, the peak frequency at these positions decreases and low frequency components become more dominant. This effect can be visualised by considering Fig. 5.3, where the curvature of the pulse wavefronts indicates a change in frequency as ρ increases. From Fig. 5.5(a), we see that the peak energy content of the pulse occurs for a frequency of $\frac{c}{4q_1}$ at a radius of $\approx 5q_1$. We note that as the FD evolves in space, different radial points acquire different peak frequencies due to diffraction. However, it can be noted that as the pulse propagates, the peak frequency at the point of peak intensity remains constant.

The property of a varying peak frequency transverse to the pulse propagation direction is known as spatial chirp, and is a common occurrence in ultrafast optics [203]. However, whilst the spatial chirp of the FD is intrinsic to the pulse, it generally arises in ultrafast optics due to misalignment of optical elements used for production of ul-

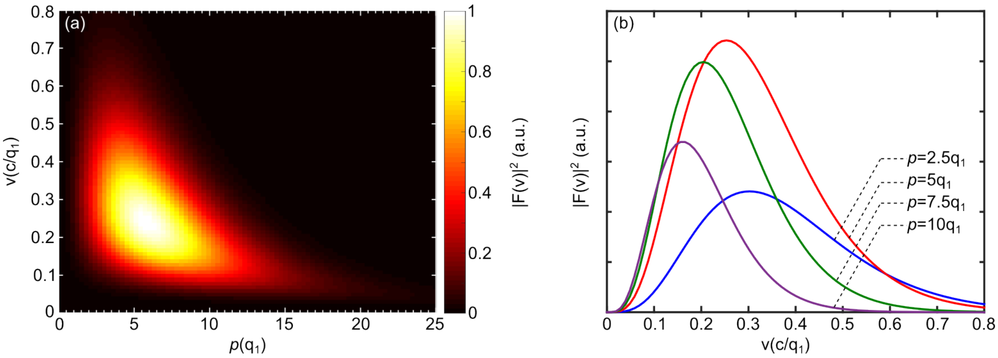

Figure 5.5: ***Fourier spectra of a "focused doughnut" pulse.*** *(a) shows the Fourier spectrum intensity of a "focused doughnut" pulse with $q_2 = 100q_1$, calculated at focus ($z = 0$, $t = 0$) as a function of radius ρ and frequency ν normalised to the maximum value. (b) shows the Fourier spectra intensity at specific radii from (a), these being $\rho = 2.5q_1, 5q_1, 7.5q_1$, and $10q_1$. Both figures illustrate a clear dependence of the bandwidth, intensity, and peak frequency on radial position.*

trashort pulses e.g. prisms, tilted substrates and Fourier pulse shapers. This lack of control of the phenomenon leads to the spatial chirp being considered an undesirable side-effect. The well-defined spatial chirp of the FD pulse however, allows to exploit this property by coupling frequency information to spatial positions of the pulse, a situation which is of interest for spectroscopy for example. In addition, it can be noted that the spatial chirp of the FD is axially symmetric, as per the topology of the pulse, and so can in fact be termed radial chirp. This radial chirp is a manifestation of the space-time non separability of the FD pulse.

A further point is that for all ρ, the bandwidth of the FD pulse is greater than the peak frequency. As an example we consider the Fourier spectrum at $\rho = 5q_1$ [Fig. 5.5(b), red curve]. The peak frequency ν_0 at this ρ value is $\frac{c}{4q_1}$, compared to a full width at half maximum bandwidth of $\sim 1.1\nu_0$. For instance, an FD pulse with a peak frequency in the green region of the optical spectrum (ν_0 =550THz), would possess a total bandwidth of $\sim$ 605THz, covering the entire optical spectrum and extending into both the infra-red and ultra-violet. This can be taken in contrast to the typical bandwidth-limited pulses produced by solid-state lasers, for which the bandwidth will always be smaller than the peak frequency.

The space-time non-separability of the FD pulse can be further examined by considering the effects of truncating the bandwidth of the pulse. For a conventional pulse, for example a Gaussian pulse, restricting the bandwidth would only affect the temporal structure of the pulse. However, in the case of the FD, it can be anticipated that bandwidth limitations will affect both the temporal and transverse profile of the pulse.

We consider this scenario in Fig. 5.6, which shows the effects of bandwidth limitation on pulse topology. Fig. 5.6(a) illustrates the full Fourier spectrum of a FD pulse at focus with characteristic parameters $q_2 = 100q_1$ (as seen in Fig. 5.5), with the cor-

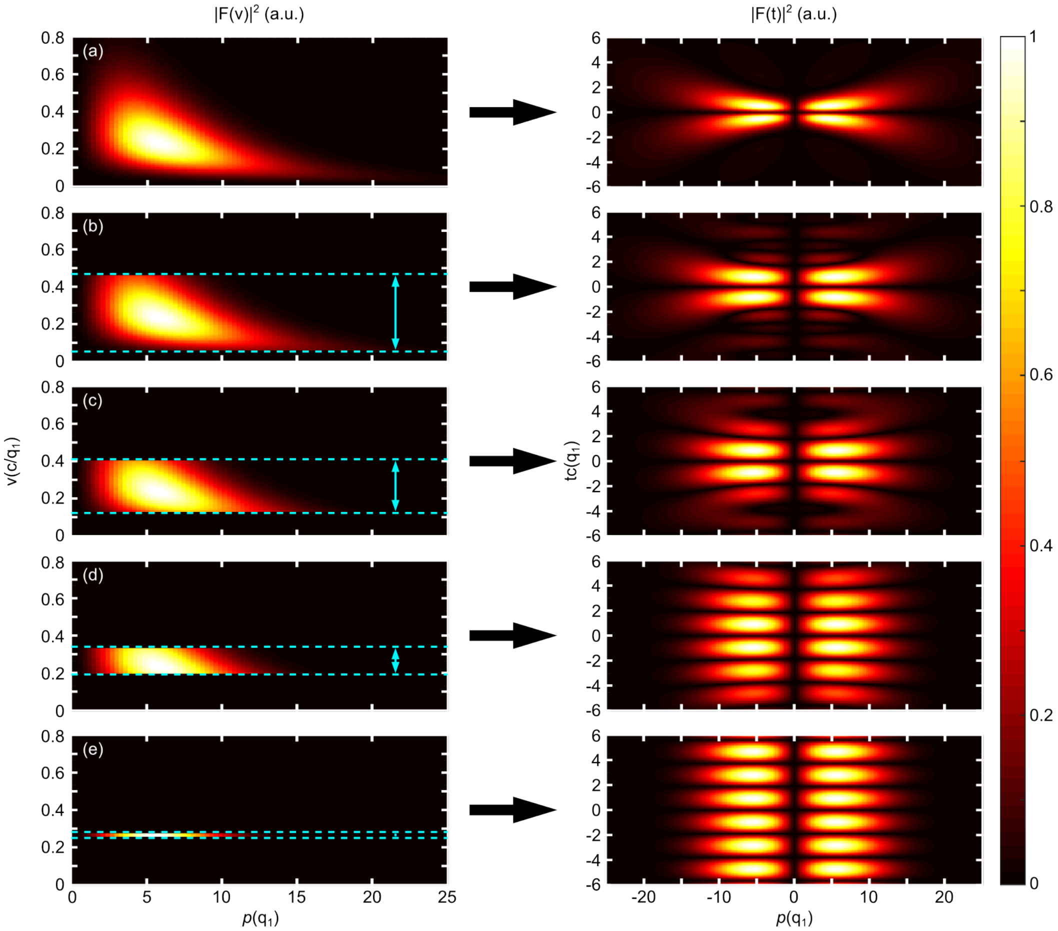

Figure 5.6: ***Reconstructions of "focused doughnut" pulses with truncated frequency spectra.*** *This figure shows how the topology of "focused doughnut" pulses is affected by a truncations to their bandwidth. The left-hand column shows Fourier spectra intensities as a function of radius and frequency, with (a) showing the full spectra for a "focused doughnut" at focus with parameters $q_2 = 100q_1$, and (b)-(e) showing the spectra with increasing levels of frequency truncation indicated by the dashed blue lines. The right-hand maps show the field intensity as a function of radius and time for the pulses reconstructed from the Fourier spectra on the left.*

responding pulse topology. Subsequent plots [Fig. 5.6(b)-(e)] illustrate an increasing truncation of the Fourier spectra from both high and low frequency ends of the spectra, along with the pulses reconstructed from the available bandwidth.

Although the topology of the FD pulse is relatively unaffected for small truncations - with only small deformations to the head and tail of the pulse occurring [Fig. 5.6(b)] - increasing bandwidth truncation leads rapidly to a loss of single-cycle nature, decrease in transverse pulse extent, and reduction in radial chirp [Fig. 5.6(c)-(d)]. The reduction in size can be interpreted in terms of the loss of low frequency components during the bandwidth truncation, which are dominant at larger radii. Under the limiting case of significant bandwidth truncation, the FD pulse collapses towards a single-frequency radially polarised beam [Fig. 5.6(e)].

This analysis is of particular relevance for any scheme that seeks to generate an FD pulse experimentally, which will likely be subject to some limitations in the available frequency bandwidth. The consequences of such limitations shall be examined further in Chapter 6.

5.3.3 Potential applications

With its range of intriguing properties, there are a range of potential applications that could benefit from an experimental realisation of the FD pulse. We have already mentioned one addressed in Hellwarth and Nouchi’s original paper, which is that of utilising the longitudinal field components of the FD pulse to accelerate particles [20]. This suggestion has been further examined in other works [204], with similar schemes having been demonstrated in the Terahertz regime [205].

Spectroscopy applications have been suggested that take advantage of the broadband nature of the FD pulse. However we mentioned in the previous section how the radial chirp of the pulse could be exploited to couple frequency information to spatial positions of the pulse. Furthermore, it is anticipated that the spatiotemporal coupling of the pulse, combined with the unusual field topology, could be used to drive excitation modes in an analyte that would not be accessible under illumination with conventional electromagnetic radiation. This is particularly true of toroidal excitations in matter, which we have already identified as bearing topological similarity to these free-space toroidal pulses. However, it is important here to note that only the TM FD pulse shares similarities in field structure to the toroidal multipoles, with the field distribution of the TE FD pulse being analogous to the magnetic multipoles. This is expected to manifest as a distinction in the light-matter interactions of the two pulses, which shall be examined later in this chapter.

Communications applications have been of particular interest owing to the strong energy confinement and tunable diffraction of the FD pulse. This is relevant not just in the context of a new free-space information carrier, but also as a new form of guided wave in waveguides or optical fibers, which would be of particular interest to the telecommunications field. Indeed the topic of guided localised waves has already received some theoretical discussion in the literature [172, 206, 207]. Ultimately, this could lead to communication schemes purely based on dedicated FD antennas, emitters and detectors.

Several new experimental methodologies could be enhanced by a FD pulse. For example, one could take advantage of the focusing properties and arbitrary focal region depth of the FD pulse to realise high depth-of-field microscopes. In addition, light-assisted manufacturing methods could benefit from utilising the FD as a tightly-confined energy packet that exhibits unique interactions with matter.

5.4 Simulation of "focused doughnut" pulses

Finite-element modeling of 'focused doughnut' pulses, and more generally any of the focus wave modes derived from Ziolkowski's work [124], is a non-trivial exercise. Owing to the complex spatiotemporal coupling and broadband nature of these pulse solutions to Maxwell's equations, the suitability of commercially available finite-element software for modeling the propagation and interaction of these pulses is unclear. To the author's knowledge, this problem has not previously been addressed in any literature. Indeed, the propagation in non-free-space environments and interactions of focus wave modes as a whole has received little attention [168, 172].

As such, the potential of utilising COMSOL 3.5a for modelling of FD pulses shall be evaluated here. There are two aims to this work; the first is to develop an understanding of how finite-element modeling treats these complex, space-time non-separable pulses. This would mean that in future, they can easily be recognised as the output from a pulse transformation simulation. The second is that it would allow simulation of the interaction of FD pulses with a variety of media, which will provide an insight into potential applications of these pulses.

Simulations of the FD are conducted in the transient domain of COMSOL Multiphysics, using the methodology outlined in Section 2.4.3. A (real) TE FD pulse is chosen as a case study with characteristic parameters $q_2 = 100q_1$. It is defined in the simulation by the azimuthal electric field E_θ exclusively [Eq. 5.7]. This is converted into a Cartesian basis so as to be compatible as a transient input field on a scattering boundary in COMSOL (see Section 2.4.3) :

$$E_\theta \hat{\theta} \rightarrow -E_\theta sin\left(\theta\right) \hat{\mathbf{x}} + E_\theta cos\left(\theta\right) \hat{\mathbf{y}}. \tag{5.13}$$

As the real component of E_θ is chosen, it is anticipated that the simulated field topology will resemble the analytic pulse shown in Fig. 5.3(a)-(c). Simulations are conducted in a cylindrical domain of length $15q_1$ and radius $25q_1$ over a time range of $t = -\frac{30q_1}{c} \rightarrow \frac{30q_1}{c}$ with a time step $t_{step} \approx \frac{q_1}{8c}$. As the length of the cylindrical domain is significantly smaller than the q_2 parameter (considering $q_2 = 100q_1$), no significant diffraction of the pulse should be expected within the domain. The cylindrical domain is aligned along the z-axis i.e. the propagation axis of the pulse.

Fig. 5.7 shows the results of the simulation at a time $t = 0$, corresponding to the point of focus for the pulse. The three field components - transverse electric field, and longitudinal and in-plane magnetic field - are shown in (a)-(c) and show a strong correlation with the analytic fields depicted in Fig. 5.3(a)-(c), with the fields being

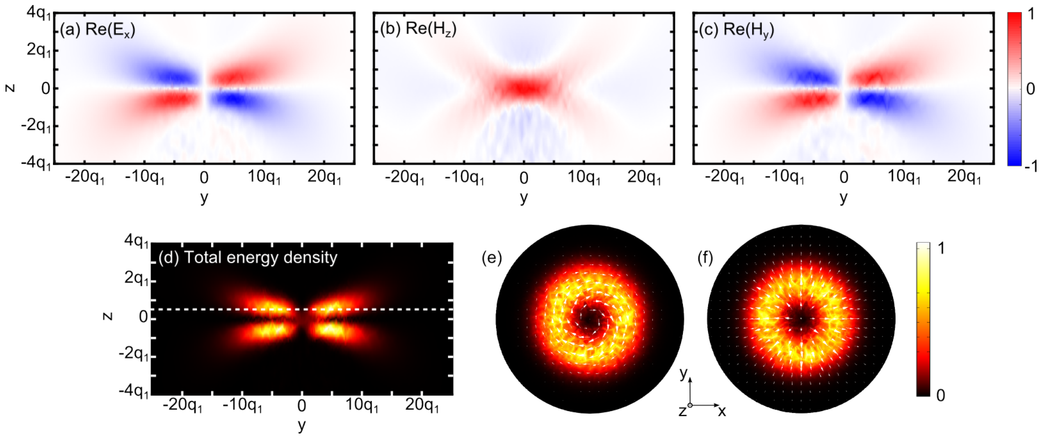

Figure 5.7: ***Simulation of a "focused doughnut" pulse.*** *This figure shows field plots on a yz plane at a time $t = 0$ extracted from a simulation of a (real) TE FD pulse ($q_2 = 100q_1$) propagating through free-space. The transverse electric field E_x, and longitudinal H_z and in-plane H_y magnetic fields are plotted in (a)-(c) respectively. The total energy density is shown in (d) with xy cross sections shown in (e) and (f) at a position of $z = 0.5q_1$ (dashed line). Arrows in (e) and (f) show the orientation of the electric and magnetic fields respectively.*

tightly confined within few-cyle toroidal structure. The energy confinement is further illustrated by considering the total energy density of the pulse [Fig. 5.7(d)], which also shows a non-zero energy density on-axis owing to the longitudinal field components of the pulse. The toroidal topology of the pulse is reinforced by Fig. 5.3(e) and (f), which show the total energy density on an xy cross-section i.e. perpendicular to the propagation direction, in addition to arrows corresponding to the E and H fields respectively. These show clearly the azimuthal E field component and the H field circling around the meridians of the toroidal pulse structure. Note that the strong longitudinal H field component seen in Fig.5.7(b) is a result of the high density of these meridian fields as they converge within the ring of the torus.

Evidence of numerical noise in both the main pulse structure and in the region behind the pulse, suggests that simulation of FD pulses is susceptible to resolution issues in both the time and spatial domain. Considering the broadband nature of the pulse established in Section 5.3.2, it is expected that high frequency components of the pulse will not be adequately resolved in the case of the time steps or spatial steps being too large. This could potentially be an issue in the case of simulations of FD interactions, but it is anticipated that suitable truncation of the analysis in the frequency domain will minimise these problems.

5.5 Interactions of “focused doughnuts” with interfaces

Whilst this work is predominantly focused on the goal of obtaining localised waveform transformations from metamaterial structures, there is also interest in what applications these waveforms could potentially be utilised, with some of these already mentioned in previous sections. As such, it would be desirable to have knowledge of how these complex waveforms interact with dielectric and metallic objects in the path of their propagation. As with the modeling described in the previous section, these scenarios have not been addressed in literature. However, with knowledge that COMSOL 3.5a is a suitable tool for modeling the propagation of “focused doughnut” pulses in free-space, we can now begin using it for simulating interaction scenarios.

We first consider the case of a FD pulse at normal incidence to macroscopic media, these being a semi-infinite dielectric medium and a PEC interface, giving an understanding of how the pulse interacts at a boundary and how the field topology is altered under reflection and transmission. It can be noted that the topic of reflection and refraction of localised waves has already received some discussion in the literature [208], illustrating some of the intricacies of the interaction particularly in the case of oblique incidence.

We first consider a PEC boundary located at $z = 20q_1$ in the free-space propagation domain. Fig. 5.8(a) and (b) show the TE and TM pulse respectively at two times - one prior to incidence on the boundary (t_1) and one after the pulse has been reflected (t_2).

For the TE FD pulse in Fig. 5.8(a), the transverse electric and longitudinal magnetic field components are shown. It is clear from examining the field distributions at the two time steps that, upon reflection, the transverse electric field of the TE pulse rotates in the same direction with respect to the propagation direction as before reflection. Similarly, the longitudinal magnetic field component both before and after reflection has a component parallel to the propagation direction leading the pulse.

In contrast however, the reflection of the TM pulse at the boundary in Fig. 5.8(b) results in the reversal of both the electric and magnetic field components. After reflection, the transverse magnetic fields are counter-rotating with respect to the propagation direction. The longitudinal electric field component is dominated by a strong component parallel to the propagation direction at the pulse front. Upon reflection, the electric field at the pulse front is anti-parallel to the propagation of the pulse. The presence of a longitudinal field component, anti-parallel to the propagation direction, at the leading edge of the pulse is a particularly intriguing and non-intuitive property of the reflected TM FD pulse.

This modeling of the FD pulse also highlights the spatiotemporal transformations the pulse undergoes, as described in Section 5.3.1 and Fig. 5.4(c) and (d). These transformations are independent of the interaction of the pulse with the interface. It can be clearly seen in Fig. 5.8(a) how, after reflection at the boundary, the transverse magnetic field of the pulse is beginning to transform from single cycle to $1\frac{1}{2}$ cycle nature. Equivalently, the longitudinal electric field is beginning to transform from $1\frac{1}{2}$ cycle to single cycle nature. This spatiotemporal transformation is also evident in Fig.

(a) TE FD incident on PEC boundary

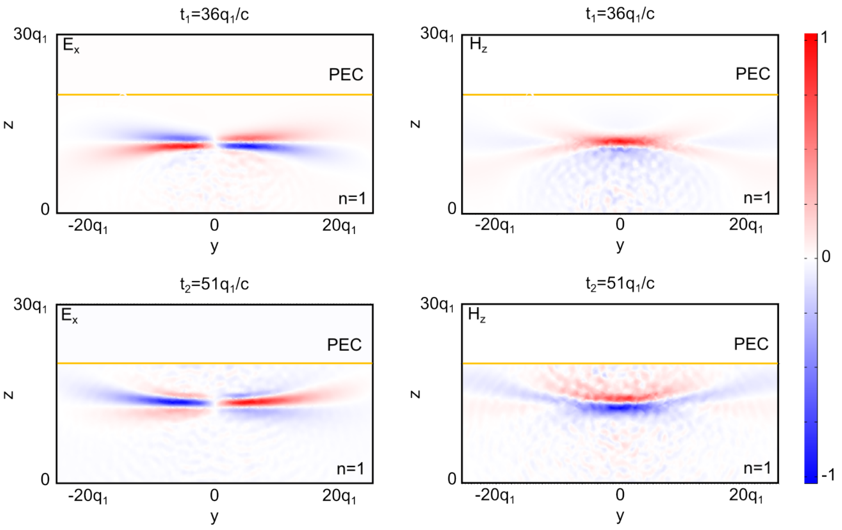

(b) TM FD incident on PEC boundary

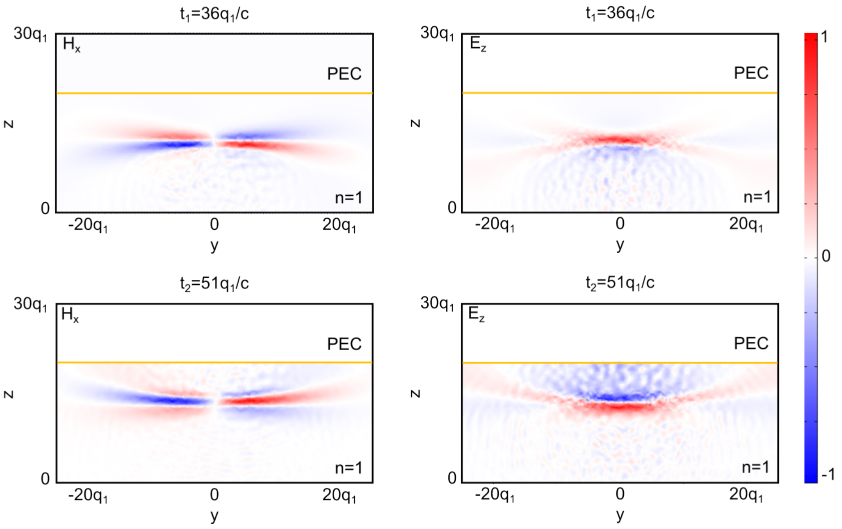

Figure 5.8: ***Interaction of “focused doughnut” pulses with continuous PEC boundaries.*** *This figure illustrates reflection of “focused doughnut” pulses from a perfect electrical conductor. (a) Transverse electric (left) and longitudinal (right) magnetic field components of a transverse electric FD pulse before (t_1) and after (t_2) reflection. (b) Similar to (a) but for a transverse magnetic pulse. In both cases the parameters of the FD pulse are $q_2 = 100q_1$ and the boundary is located at a distance $z = 20q_1$ from the focal point of the pulse ($z = 0$). All field components have been normalized to their maximum value.*

5.8(b) for the TE FD pulse.

We now consider interaction at a dielectric boundary. The modeling space is separated into two regions - one free-space and one of refractive index $n = 2$, with the boundary located at $z = 15q_1$ so as to illustrate both the reflected and transmitted pulse. Fig. 5.9 shows the results of these models in both TE and TM incidence cases, with the transverse and longitudinal fields shown at two times - one prior to incidence on the boundary (t_1) and one after the pulse has been reflected and transmitted (t_2). In

(a) TE FD incident on dielectric boundary

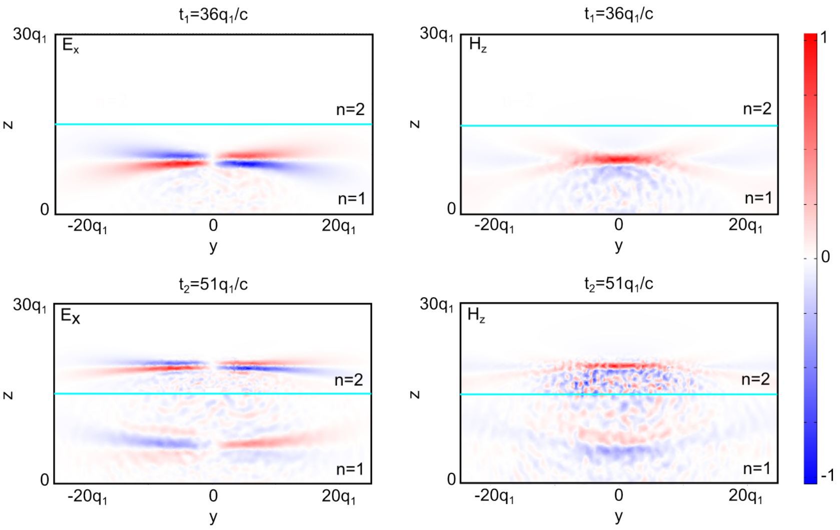

(b) TM FD incident on dielectric boundary

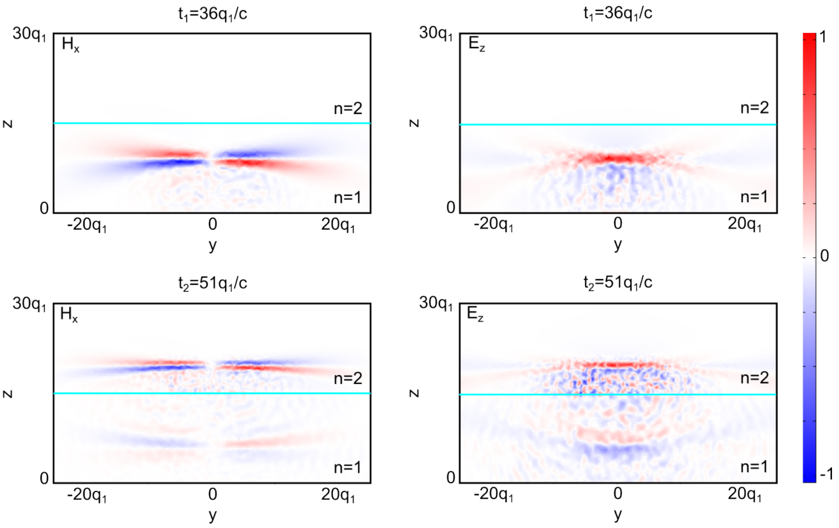

Figure 5.9: ***Interaction of “focused doughnut” pulses with semi-infinite dielectrics.*** *This figure illustrates reflection and refraction of “focused doughnut” pulses at a vacuum-dielectric interface. (a) Transverse electric (left) and longitudinal magnetic field (right) components of a transverse electric FD pulse before (t_1) and after (t_2) incidence on the interface. (b) Similar to (a) but for a transverse magnetic pulse. In both cases the parameters of the FD pulse are $q_2 = 100q_1$ and the boundary is located at a distance $z = 15q_1$ from the focal point of the pulse ($z = 0$). All field components have been normalized to their maximum value. The dielectric is considered to be semi-infinite with a refractive index $n = 2$.*

both polarisation cases the toroidal topology of the pulse is maintained after being transmitted though the dielectric boundary and it undergoes the expected increase in momentum within the medium as for conventional electromagnetic pulses. Similarly the reflected pulse also maintains its toroidal topology. Evaluation of reflection and transmission coefficients for the reflected and transmitted respectively pulses indicates that both TE and TM FD pulses interact with the semi-infinite dielectric as predicted by evaluation of the Fresnel equations.

It is worth noting that all models in this section utilise idealised non-dispersive metals and dielectrics, in the form of PEC and a dielectric refractive index of $n = 2$. This is due to limitations in Maxwell's equations solver utilised for this study, which prohibits temporal dispersion for transient models. As illustrated previously in this paper, the FD pulse is highly broadband with a bandwidth greater than the peak frequency. For realistic materials, it is likely that dispersive effects would be present over such a wide frequency range, inducing some reshaping to the temporal profile of the pulse. However, it is expected that this will not limit the analysis of the reflected and transmitted geometries. It could also be considered that this would be a valid description for the interaction of matter with FD pulses in the microwave regime. This is owing to the dispersion of metals at microwave frequencies, which allows metals generally be approximated as PECs for thicknesses greater than μm-scale [209, 210].

5.6 Interactions of "focused doughnuts" with particles

In this section we shall consider the interactions of FD pulses with particulate matter, which of particular relevance given the potential of these pulse to be utilised for sensing and spectroscopy applications.

First, we consider dielectric spheres, of diameter < the pulse diameter, in the path of the pulse. It is anticipated that the large bandwidth of these short cycle pulses should result in excitation of multiple modes within the particles. We then consider the interaction of FD pulses with a dielectric torus. Again we anticipate broad modal excitation within the particles, with the additional interest of the topological similarity between the FD pulse and a toroidal particle. Asin the previous sections, the FD pulses are defined with parameters $q_2 = 100q_1$.

5.6.1 Interaction with dielectric spheres

The case considered here is that of a spherical dielectric particle located at $\rho = z = 0$. The radius of the nanoparticle is given as q_1, such that it is less than the width of the FD pulse. In this regime, excitation by the ultra-broadband FD pulse can be expected to induce multiple Mie modes of the dielectric nanoparticle. As in the previous section, the dielectric is given a non-dispersive refractive index of $n = 2$. For an incident TM FD pulse, the interaction with the particle is dominated by the longitudinal electric field on axis. Fig. 5.10 shows both the simulated interactions [Fig. 5.10(a) and (b)] and artistic schematics [Fig. 5.10(c) and (d) insets] for both TE and TM cases.

We first evaluate the normalised electric field intensity within the particle as a function of frequency. This is calculated first by taking a Fourier transform of the E-field within the particle to move from the time to the frequency domain:

$$E_i(r,t) \xrightarrow[transform]{Fourier} E_i(r,\omega), \tag{5.14}$$

Where $i = x, y, z$. The E-field intensity is then integrated across the dielectric sphere, to give total intensity as a function of frequency within the particle:

$$P(\omega) = \int \left[|E_x(r,\omega)|^2 + |E_y(r,\omega)|^2 + |E_z(r,\omega)|^2 \right] d^3r. \tag{5.15}$$

This is then normalised to the power incident on the particle from the incident pulse.

The E-field intensity within the dielectric sphere is shown in Fig. 5.10(c) and (d) for the TE and TM incidence case respectively. For TE FD incidence, a clear series of Mie modes are excited corresponding to resonant distributions of the azimuthal field throughout the particle. This is emphasised in Fig. 5.10(e), which shows out-of-plane electric field distributions for a cross-section through the particle at three different peaks. In contrast, the spectrum for excitation of the particle by a TM pulse is more complicated, owing to the interplay between the radial and longitudinal electric field components. As such, the TM excitations are considerably weaker than those from TE pulse incidence. Modes corresponding to distributions of x-aligned (in-plane) E field from three frequencies are shown in Fig. 5.10(f), corresponding to a series of Mie resonances, similar to the TE pulse case.

We now evaluate the multipoles excited within the dielectric sphere to extend our description of the interaction. These are evaluated up to quadrupole order using the integrals in Section 2.2.1. As the initial simulations are conducted in the time domain we also utilise the methodology outlined in Appendix D.

In the case of TE FD incidence on the particle [Fig. 5.10(g)] it is clear that the dominant contributors to the scattering are the magnetic multipoles. This is anticipated owing to the azimuthal E field configuration of the TE FD pulse. Contributions from the electric and toroidal multipoles are significantly suppressed. For the case of TM incidence [Fig. 5.10(h)] however, the multipole excitations are more complex. As expected, electric multipoles dominate at lower frequencies, as a result of coupling to the longitudinal E field of the incident pulse. However at $\sim 0.46(c/q_1)$, the toroidal dipole becomes the dominant scattering multipole up to quadrupole order. This is a particularly intriguing feature as it demonstrates a significant toroidal response in a system with non-toroidal geometry, reiterating the importance of toroidal multipoles in evaluation of scattering systems.

It can be seen from Fig. 5.10(h) that in the case of TM FD incidence on a dielectric sphere, at a frequency of $\nu \approx 0.46c/q_1$ both the electric and toroidal dipoles are resonant. This gives an opportunity to study the unusual electromagnetic phenomenon

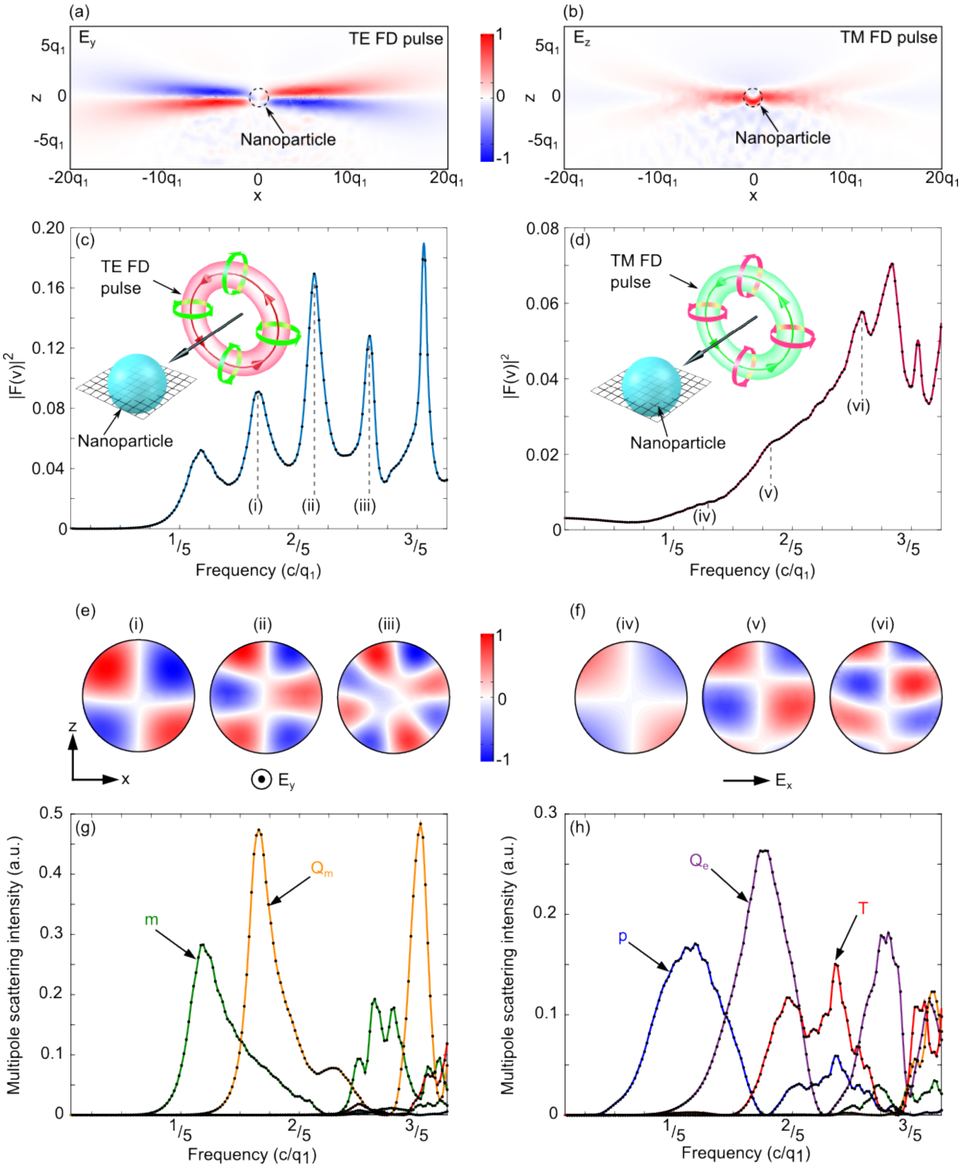

Figure 5.10: ***Interaction of “focused doughnut” pulses with dielectric nanoparticles.*** *This figure illustrates the interaction of “focused doughnut” pulses with dielectric spheres of radius q_1 and refractive index $n = 2$.(a) and (b) show the xz cross-sections of the COMSOL simulation domain at a time $t = 0$. (a) shows the normalised transverse electric field of a TE FD pulse, and (b) shows the normalised longitudinal electric field of the TM FD pulse. The outline of the spherical nanoparticle is shown by the dotted line. (c) and (d) show the electric field intensity integrated over the volume of the nanoparticle as a function of frequency, when under excitation from a transverse electric (TE) and a transverse magnetic (TM) FD pulse respectively. (e) and (f) show the electric field distributions on an xz cross-section of the nanoparticle (see grid in the insets to (c) and (d)) at resonance positions (i)-(vi). These have been individually normalised to emphasise each distribution. (g) and (h) show the scattering intensity of the individual Cartesian multipoles up to quadrupole order (electric dipole p, magnetic dipole m, toroidal dipole T, electric quadrupole Q_e, and magnetic quadrupole Q_m) for illumination with TE and TM FD pulses, respectively. In (c)-(d) and (g)-(h) dots correspond to simulation data points, while lines serve as eye guides.*

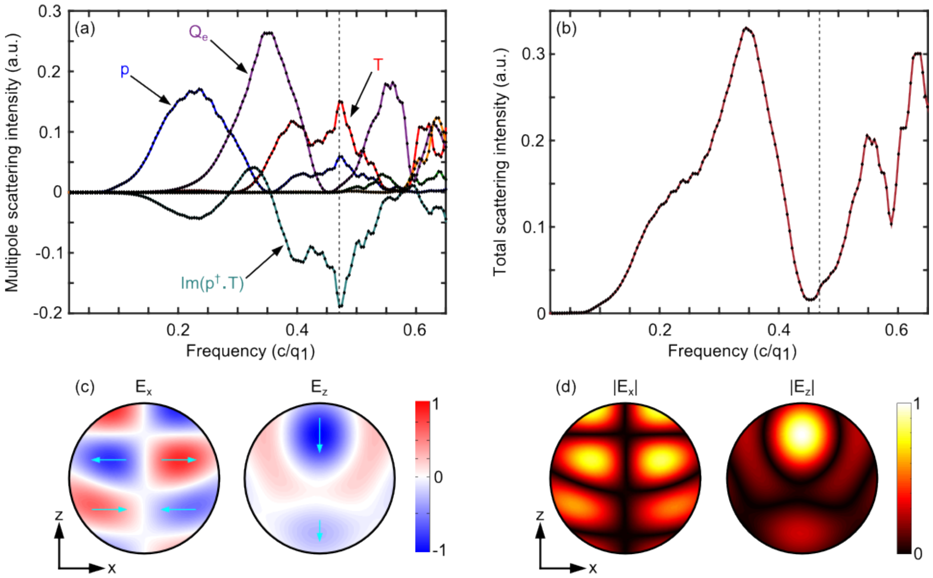

Figure 5.11: ***Anapole a in dielectric sphere excited by a TM “focused doughnut”.*** *(a) shows the scattering intensity of the individual Cartesian multipoles up to quadrupole order in a dielectric sphere when excited by a TM FD pulse. In an extension to the plot in Fig. 5.10(h), here we include the term proportional to* $\mathrm{Im}\left(\mathbf{p}^{\dagger}\cdot\mathbf{T}\right)$ *representing interference between the electric p and toroidal T dipoles with it’s maximum absolute value indicated by the dashed line. (b) gives the total scattering intensity summed over all multipoles. The point of suppressed scattering at* $\nu \approx 0.46c/q_1$ *is indicated by the dashed line. In both (a) and (b) dots correspond to simulation data points, while lines serve as eye guides. (c) and (d) show the* E_x *and* E_z *electric field distributions and absolute values of these fields respectively on an* xz *cross-section of the nanoparticle at the anapole resonance. These have been individually normalised to emphasise each distribution.*

known as the dynamic anapole, or non-radiating configuration. As discussed in Section 2.1.3 the toroidal dipole radiates in an identical manner in the far-field to the electric dipole, save for a phase shift and additional dependence on wavelength. For co-located and co-aligned electric and toroidal dipoles, their radiation patterns can destructively interfere in the far-field. This results in a non-radiating configuration which does not contribute in the far-field despite the existence of a charge-current distribution in the near-field. This can be seen in the expression for total multipole scattering intensity [Eq. 2.2.2] where the term proportional to $\mathrm{Im}\left(\mathbf{p}^{\dagger}\cdot\mathbf{T}\right)$ reflects constructive or destructive interference between the electric and toroidal dipoles and as such can take either positive or negative values.

We plot the multipole scattering intensity for a dielectric sphere with a TM FD incident upon it and include the $\mathrm{Im}\left(\mathbf{p}^{\dagger}\cdot\mathbf{T}\right)$ interference term [Fig. 5.11(a)]. It can be seen that at the point of electric and toroidal dipole reosnance ($\nu \approx 0.46c/q_1$) the interference term is negative with a large absolute value, indicating strong destructive interference between the excitations. This is reflected in the total scattering intensity summed over all multipoles [Fig. 5.11(b)] which reveals a distinct decrease in total scattering in the region of the resonant electric and toroidal dipoles, typical of a dynamic anapole.

Although the total scattering of the dielectric sphere decreases, the configuration at $\nu \approx 0.46c/q_1$ cannot be considered a true anapole for several reasons. Firstly, as the electric and toroidal dipoles are not equal in magnitude, destructive interference cannot completely cancel the far-field radiation, leaving some residual dipolar radiation. Furthermore, the scattering of other multipoles such as the electric quadrupole Q_e is non-negligible at the electric and toroidal dipole resonance. In addition, as the expansion here is only calculated up to the quadrupole order, it cannot be determined whether higher order multipoles e.g. electric octupole, will mask this dynamic anapole effect in the far-field.

Despite this, this quasi-anapole is dominant up to the quadrupole order at $\nu \approx 0.46c/q_1$. This reinforces the necessity of including the toroidal multipoles in the microscopic multipole analysis. We note that the minimum in total scattering in the region of the electric quadrupole anti-resonance shall not be observed if the toroidal dipole is neglected and only the electric dipole is taken into account.

5.6.2 Interaction with dielectric tori

In the previous section, it was demonstrated that FD pulses incident on dielectric spheres will induce broadband modal excitation and in particular, the excitation of a dominant toroidal mode in a system without toroidal topology. Here the case of FD pulses incident on a dielectric torus will be considered. Owing to the topological similarities between the FD pulse and toroidal particles, it is anticipated that such an interaction would lead to similar broadband mode excitation.

In the case of a TE FD pulse interacting with a toroidal particle, it is expected that excitation of toroidal modes will be suppressed in favour of magnetic modes. This is due to the field topology of the TE FD pulse [Fig. 5.12(a)], which consists of closed loops of azimuthal electric field and restricts the radial currents necessary for toroidal modes. In contrast, the field configuration of the TM FD pulse is analogous to the toroidal dipole in matter, with both possessing closed loops of azimuthal magnetic field [Fig. 5.12(b)]. Consequently, it is anticipated that toroidal modes could be excited dominantly across a broad frequency range in such an interaction.

Using the same methodology as in the previous section, we construct a transient model of both TE and TM FD pulses incident on a dielectric torus. The FD has characteristic parameters of $q_2 = 100q_1$ and is incident on a dielectric torus of small radius $r = q_1$, large radius $R = 2q_1$, and refractive index $n = 2$, located at $x, y, z = 0$. Cross sections of the simulated interaction at a time $t = 0$ are shown in Fig. 5.12, with (c) showing the transverse E-field of the TE FD pulse and (d) showing the longitudinal field of the TM pulse.

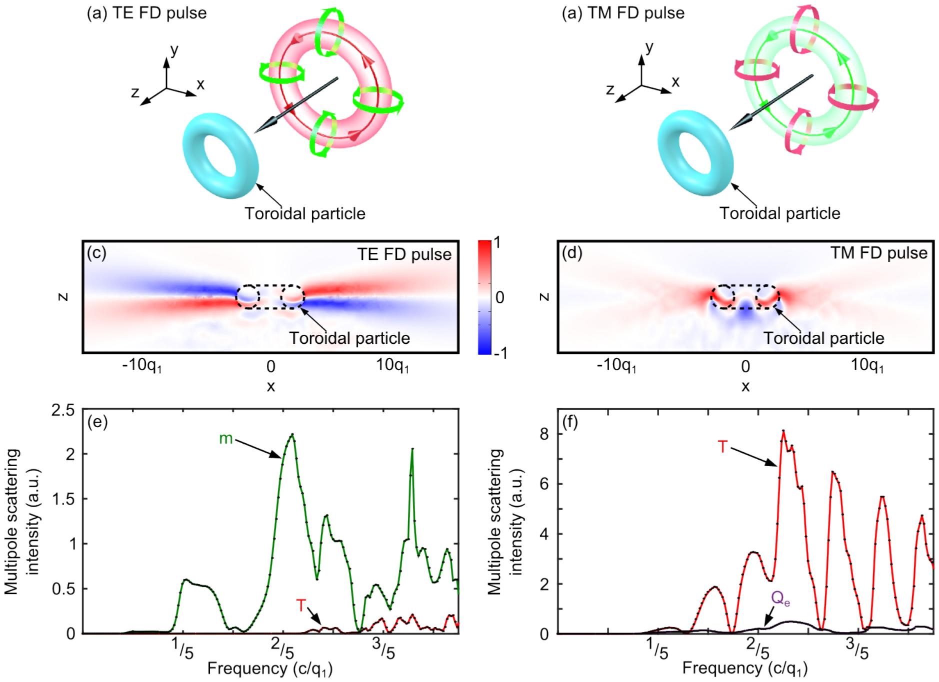

Figure 5.12: ***Interaction of “focused doughnut” pulses with dielectric tori.*** *This figure illustrates the interaction of “focused doughnut” pulses with toroidal dielectric particles of small radius q_1, large radius $2q_1$, and refractive index $n = 2$. (a) and (b) shows a schematic of TE and TM FD pulses respectively incident on a dielectric torus. (c) and (d) show the xz cross-sections of the COMSOL simulation domain at a time t = 0. (c) shows the normalised transverse electric field of a TE FD pulse, and (d) shows the normalised longitudinal electric field of the TM FD pulse. The outline of the toroidal particle is shown by the dotted line. (e) and (f) show the scattering intensity of the individual Cartesian multipoles up to quadrupole order for illumination with TE and TM FD pulses, respectively. The dots correspond to simulation data points, while lines serve as eye guides*

The microscopic multipoles are then extracted from the displacement currents excited within the dielectric tori, as per the same method described in the previous section. For TE FD incidence, the spectrum consists primarily of a series of magnetic dipole resonances [Fig.5.12(e)]. This can be understood in terms of the azimuthal E-field driving currents around the loop of the torus to give a typical magnetic dipole current distribution. Counter-intuitively there is also a weak contribution from the toroidal dipole at higher frequencies. This is attributed to the gradient in azimuthal field across the width of the dielectric torus.

In the case of TM FD incidence however, the excitation of conventional multipole modes is suppressed, with the spectrum instead being primarily composed of a series of toroidal dipole resonances, with a small electric quadrupole contribution [Fig .5.12(f)]. This can be understood in terms of both the radial and longitudinal E-fields of the incident pulse driving poloidal currents along the meridians of the dielectric torus, forming a closed loop of magnetic field that is characteristic of the toroidal dipole

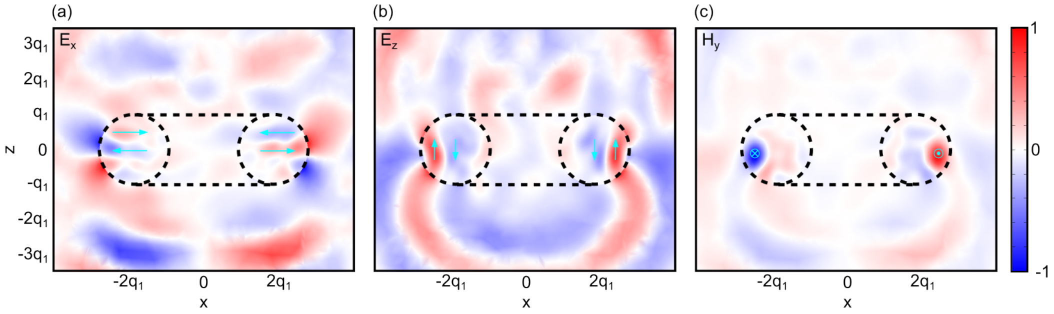

Figure 5.13: ***Fields excited within a dielectric torus by a TM "focused doughnut" pulse.*** *This figure shows xz cross-sections of the COMSOL simulation (TM FD pulse incident on dielectric torus) at a time* $tc = 10q_1$ *i.e. after the FD pulse has propagated past the torus. The figure shows (a) in-plane electric field* E_x*, (b) longitudinal electric field* E_y*, and (c) transverse magnetic field* H_y*. These have been individually normalised to emphasise each distribution.*

excitation. The symmetry of the system suppresses the excitation of the conventional electric and magnetic multipoles. The exception is a small electric quadrupole response, which is attributed to the varying intensity of the radial field across the nanoparticle. In particular, the electric dipole is almost completely suppressed. This is understood to be a result of the strongest longitudinal field components of the incident pulse existing in the central void of the dielectric torus, and so do not contribute strongly to the interaction. Within the dielectric torus, the dominant excitation mechanism is the radial field component of the TM FD, which due to symmetry cannot create an electric dipole resonance.

The presence of toroidal dipoles in TM excitation spectrum can be reinforced by considering the field distributions within the dielectric torus. The in-plane and longitudinal electric fields, and transverse magnetic fields are examined at a time $tc = 10q_1$, corresponding to a time significantly after the TM FD is incident on the torus [Fig. 5.13]. It is clear that the field distribution within the torus is closely correlated with that of an ideal toroidal dipole. The combination of in-plane and longitudinal electric fields seen in Fig. 5.13(a) and (b) would drive poloidal currents around the meridians of the dielectric torus. Fig. 5.13(c) shows a highly confined azimuthal magnetic field within the torus, typical of a toroidal excitation. It can be noted that the broad series of toroidal resonances observed in the excitation spectrum [Fig. 5.12(f)] allows for observation of the excited toroidal modes in the time domain, rather than after transformation to the frequency domain.

5.7 Summary

In this chapter, the history and theory behind localised pulse solutions to Maxwell's equations have been examined. In particular the "focused doughnut" pulse family has been identified as a particularly intriguing subset of these solutions that represents a propagating free-space analogue to the dynamic toroidal multipole moments in matter. Key properties of the FD pulses, such as spatiotemporal evolution, and broadband radial chirp have been identified and discussed.

This chapter reports on the first instance of a full 3D finite element simulation of FD pulses has been conducted and has been demonstrated to accurately reproduce the topology and propagation properties of the theoretical pulse. This methodology is utilised here to study the interactions of FD pulses with both continuous and particulate matter, with results such as unusual field configurations upon reflection, broad modal excitations and dominant toroidal dipole responses in dielectric particles, and dynamic anapole-like scattering.

The research into the FD pulse is still in its infancy, with no practical realisation of these pulses yet achieved. However, the results obtained here in this chapter suggest multiple potential applications of these pulses if they can be physically synthesised. Key amongst these is the use of FD pulses for spectroscopy, which would take advantage of the broadband nature of the pulse. This would be particularly relevant in the case of structures with toroidal topology [Fig. 1.2] where FD pulses could excite a range of toroidal modes which would not be otherwise accessible. In addition, the potential of FD pulses to preferentially excite toroidal modes could prove valuable in sensing applications and also form the basis of a detector to detect experimental realisations of these pulses.

Chapter 6

Generation of “focused doughnut” pulses

6.1 Introduction

In the previous chapter, we provided a detailed discussion of the history, theory, and properties of the intriguing “focused doughnut” pulse. We further produced a numerical analysis of the interactions the FD pulse undergoes with both continuous and particulate matter, demonstrating non-trivial light-matter interactions. This reinforces our interest in this unique electromagnetic pulse and in obtaining an experimental realisation of the FD pulse - something that has not yet been achieved to date. This is unsurprising given the complex field topology, ultra-broadband nature, and spatiotemporal coupling of the pulse. In this chapter, we shall seek to directly address this question of experimentally generating FD pulses, towards the ultimate aim of obtaining a pulse transforming device for converting conventional electromagnetic radiation into FD pulses.

Since Brittingham first introduced the concept of focus wave modes in 1983 [167], there are have been a series of theoretical works discussing how localised transmission of electromagnetic energy could be achieved experimentally. Many of these works were produced by Ziolkowski, focusing on generation of localised pulses from discrete, tunable antenna arrays [211, 213], driven apertures [214], and log-periodic antennae [215]. An example of a tunable antenna array is given in Fig. 6.1(a), which consists of N individual antenna elements, each with an individual driving function f_N. The feasibility of this antenna approach was verified by the synthesis of acoustic analogues of localised electromagnetic pulses using arrays of acoustic resonators [179, 180]. A depiction of one of these acoustic analogues was given in Fig. 5.1(e). Other suggested schemes include generation from oscillating electric dipoles [173], use of a dynamic Gaussian aperture [171], and launching from a waveguide [172]. In parallel to this, synthesis of electromagnetic Bessel beams [184–186] and X-shaped pulses [169] gave the first experimental forms of localised propagating electromagnetic energy. We note

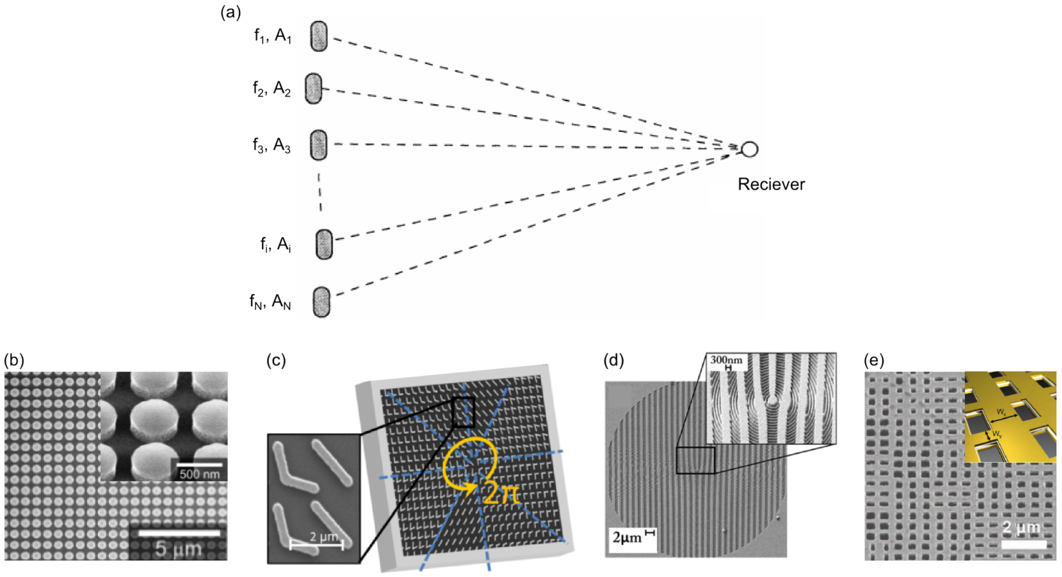

Figure 6.1: ***Prior art for our generator scheme.*** *(a) shows a generator scheme for localised waves suggested by Ziolkowski. The suggested generator scheme is based on an array of N independently addressable radiating elements positioned at arbitrary locations in space. Each element is assumed to have a radiating area of A_i associated with it and is excited with a driving function $f_i(t)$. Figure adapted from Ref. [211]. (b)-(e) give examples of planar metasurface resonator arrays for generation of complex wave shapes. (b) shows a Huygens' metasurface composed of dielectric electric and magnetic dipole resonators. Figure adapted from Ref. [212]. (c) shows a spatially varying V-shaped antenna array for creating optical vortex beams. Figure adapted from Ref. [87]. (d) gives a nanostructured hologram designed for the broadband manipulation of vector beams e.g. radially polarised light. Figure adapted from Ref. [159]. (e) shows a fishnet metamaterial structure that can be used for spatial and spectral light shaping with simultaneous amplitude and phase control. Figure adapted from Ref. [83].*

however that these beams/pulses are not the exact finite energy solutions to Maxwell's equations that the EDEPT solutions represent.

We seek to combine these theoretical works with recent advances in metamaterial engineering, in particular metasurface arrays for manipulating electromagnetic beam structure. Metasurfaces i.e. 2D structures of artificially engineered metamolecules, have received considerable interest over recent years owing to their ability to exercise amplitude, phase, and polarisation control over incident electromagnetic radiation. This had led to a series of designs exhibiting such phenomena as anomalous reflection and refraction [216, 217], generation and detection of optical vortices [87, 218], broadband manipulation of vector beams [159], wavevector selective surfaces [219], Huygens' metasurfaces [212, 220], beam shaping with surface plasmons [221], Gaussian-to-Bessel beam trasnformation [222], and spatial and spectral light shaping [83]. Examples of these metasurface arrays can be seen in Fig. 6.1(b)-(e). We note that these metasurfaces are designed primarily for interaction with harmonic beams as opposed to pulses. However, non-linear generation of Terahertz pulses from a metasurface array under

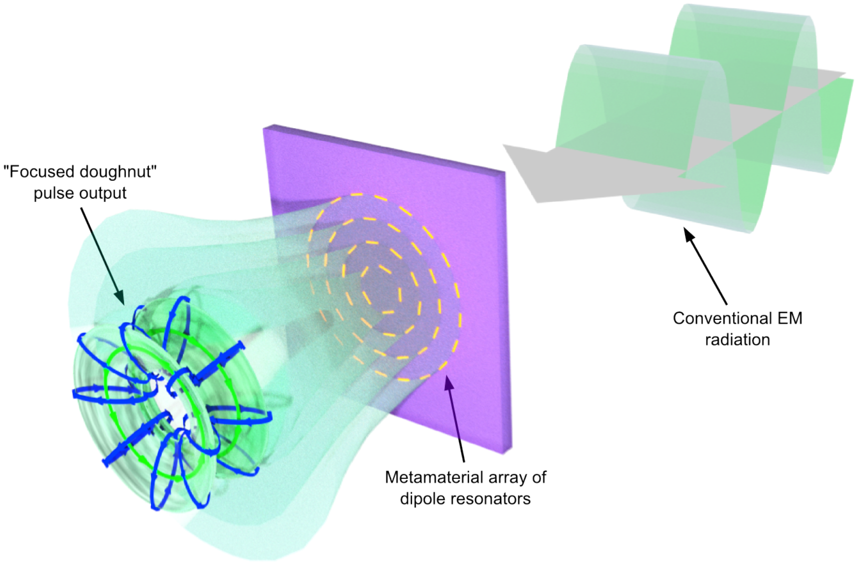

Figure 6.2: ***Schematic of "focused doughnut" generation from a metamaterial dipole array.*** *This figure illustrates the concept of a metamaterial transformer for converting conventional electromagnetic radiation into a "focused doughnut" pulse. Conventional transverse electromagnetic radiation is incident upon a metasurface array which possess a coupled spatial and frequency response. The collective response of the resonators in this array produces a propagating "focused doughnut" pulse.*

femtosecond pumping has been demonstrated [91].

The overall aim is to create a FD pulse generator that shall be, in essence, a sophisticated form of metasurface that exhibits a coupling between its spatial and frequency responses, thus allowing spatiotemporal engineering of incident light. A schematic of the intended system is given in Fig. 6.2, which depicts the conversion of conventional transverse electromagnetic radiation into a FD pulse through means of a metasurface transformer. We note that this scheme would also require the metasurface to convert from incident transverse polarisation to the radial or azimuthal polarisation characteristic of an FD pulse. A number of metasurface-based methodologies exist to address this added complexity [159, 223, 224]. The resonators in the array would be assigned specific frequency-dependent responses which would vary as a function of position on the array, thus achieving spatiotemporal coupling of the response. It is likely that these resonators will be required to operate over a broad bandwidth in order support the frequency components required for FD generation.

In this chapter, we shall begin to examine the various manifestations and complexities of such a generation scheme. We will begin by studying numerically the conditions under which an array of resonators with specified excitations can generate a localised wave approximating a FD pulse. We shall also evaluate the susceptibility of this scheme to typical experimental limitations in available bandwidth. This is anticipated to form the primary obstacle to an experimental scheme, particularly in the optical regime where broadband light control spanning an octave in frequency will be challenging. Finally, we shall consider the conditions under which the resonator array could generate a continuous train of FD pulses, and whether this is advantageous from an experimental perspective. Results obtained here lay a solid proof-of-principle foundation for the generation of FD pulse from metasurface arrays and shall be influential in designing the first experimental generators for these pulses.

6.2 Methodology for testing “focused doughnut” generation

With the ultimate aim of this work being to obtain a metamaterial based transformer for converting conventional electromagnetic radiation into FD pulses, it is necessary to evaluate the discrete, finite-sized resonator arrays for their ability to recreate FD pulses in ideal conditions.

Our methodology presented here is closely modeled off of work previously presented in the literature. In particularly, we adopt ideas based on Ziolkowski's work on discrete radiating arrays [211,213], and the analysis of few-cycle pulses generated by oscillating electric dipoles [173]. Furthermore, this approach can be considered analogous to the schemes used to produce acoustic analogues of localised electromagnetic waves [179,180].

As such, our scheme consists of a cylindrical array of individually addressable dipole resonators, arranged in concentric rings. An illustration of our test FD generator scheme is shown in Fig. 6.3. As the ideal FD pulse possesses either radial or azimuthal polarisation, the dipoles in the array are aligned in either the radial or azimuthal direction. The dipole resonators can be freely positioned, but to simplify the procedure and analysis, we chose rings at fixed radii on which to locate the dipoles, taking advantage of the azimuthal symmetry of the FD pulse. These dipoles radiate as per the radiation pattern described in Appendix B.1. It can be noted that only the far-field radiation contributions of the dipole resonators are included, as we are not interested in the field topology in the near-field of the generator array $(rl\lambda)$.

Each electric dipole $\mathbf{p}$ in the array can be independently assigned a time-dependent dipole excitation: $\mathbf{p} \rightarrow \mathbf{p}_i(t)$, with $i = 1 \rightarrow N$ where N is the total number of dipoles in the array. We note that for an ideal FD pulse, the bandwidth of the pulse decreases for larger radii, and as such we can anticipate a shorter temporal dipole excitation at the center of the array. A domain is established in which the generation scheme shall be tested, defined in units of q_1 - the effective wavelengh of the desired FD pulse. The dimensions chosen are $x, y = -100 \rightarrow 100$ and $z = 0 \rightarrow 200$ or $0 \rightarrow 400$, with the

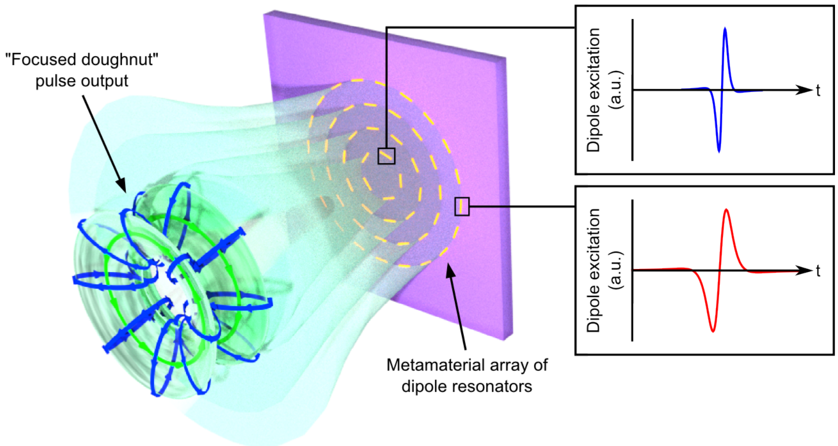

Figure 6.3: ***Schematic of “focused doughnut” generation from a driven metamaterial dipole array.*** *This figure illustrates the concept underpinning the modeling in this chapter. A metamaterial dipole array is driven with a short time-dependent excitation, which is also dependent on the radial position of the dipole in the array. The cumulative effect of the radiating dipoles results in a “focused doughnut” pulse as an output from the array.*

z-axis as the intended axis of propagation. As such, the metamaterial array is located at $z = 0$ and is aligned orthogonal to the z-axis.

The methodology for evaluating the electromagnetic field generated by the metamaterial array is as follows:

1. Consider an array of N time-dependent dipoles $\mathbf{p}_i(t)$ with $i = 1 \rightarrow N$ located on the xy plane.

2. Evaluate the frequency components of the dipole excitations through a Fourier transform.

$$\mathbf{p}_i(\nu) = \tilde{F}\left\{\mathbf{p}_i(t)\right\}. \tag{6.1}$$

3. Calculate the far-field radiation pattern of each dipole at each frequency ($\mathbf{E}_i(r,\nu)$) as per the methodology in Appendix B.1.

$$\mathbf{E}_i(r',\nu) = \frac{k^2 c}{4\pi}\sqrt{\frac{\mu_0}{\epsilon_0}}\left(\frac{e^{ikr'}}{r'}\right)\left[\hat{\mathbf{r}'} \times \mathbf{p}_i(\nu)\right] \times \hat{\mathbf{r}'}, \tag{6.2}$$

Where $\mathbf{r}' = \mathbf{r} - \mathbf{r_i}$, with $\mathbf{r_i}$ representing the position of the dipole in the array.

4. Sum the electric fields from each dipole in the array at all far-field positions of interest (i.e. position $\mathbf{r}$).

$$\mathbf{E}(r,\nu) = \sum_i^N \mathbf{E}_i(r',\nu). \tag{6.3}$$

5. Evalaute the time-dependent field generated by the array through a Fourier transform.
$$\mathbf{E}(r,t) = \tilde{F}^{-1}\left\{\mathbf{E}(r,\nu)\right\}. \tag{6.4}$$

This generated field $\mathbf{E}(r,t)$ can then be evaluated at positions and times of choice. We note that an xy aligned array will necessarily radiate in both the positive and negative z-directions. In general, we shall only be interested in the positive z direction.

6.3 Generating a single “focused doughnut” pulse

In this section, we shall utilise the methodology outlined in the previous section to test the generation of individual FD pulses by a discrete metamaterial dipole array. The analysis shall be presented in terms of the generated fields both in the time and frequency domain, and shall be compared with ideal analytic FD pulses.

6.3.1 Metamaterial pulse generator and dipole excitations

For the first proof-of-principle test of the generator scheme we consider a Huygen’s principle based approach to constructing a FD pulse. We shall begin with a stated aim of generating TE i.e. azimuthally polarised, FD pulse with characteristic parameters $q_2 = 100q_1$. In the previous section the far-field domain to be evaluated was characterised as spanning $x, y = -100 \to 100$ and $z = 0 \to 400$. As such we chose $q_1 = 3.6$, which gives an effective pulse wavelength significantly larger than the domain resolution and will lead to a pulse with a spatial extent confined within the domain. This gives a q_2 value of 360 which, following the analysis in Fig. 5.4, should allow for observations of the spatiotemporal transformations of the generated FD pulse over the z-extent of the domain. We note that the generation scheme is fully scalable from the arbitrary values used here.

For the generating array, we chose an array of 117 dipoles arranged in four concentric rings [Fig. 6.4(a)]. These rings are given radii $r = 5, 20, 35$, and 50. The choice of radii for the rings is made such that they are equidistant in radial separation, and cover the radial region in which $> 90\%$ of the desired pulse’s energy is confined. Upon each of these four rings, the dipoles are located equidistant from each other in the azimuthal direction. We note that the placement of dipoles does not produce any axes of symmetry for the array, though it is expected that the density of the dipoles should prevent the symmetry of the generated pulse from being significantly affected.

For generation of TE FD pulse, we are interested in the azimuthally polarised E-field, which is given in the previous chapter by Eq. 5.7. As such, we map the electric field of the desired ideal FD pulse to the time-dependent dipole excitations i.e. $\mathbf{p}_i(t) \propto \mathbf{E}_\theta(t)$

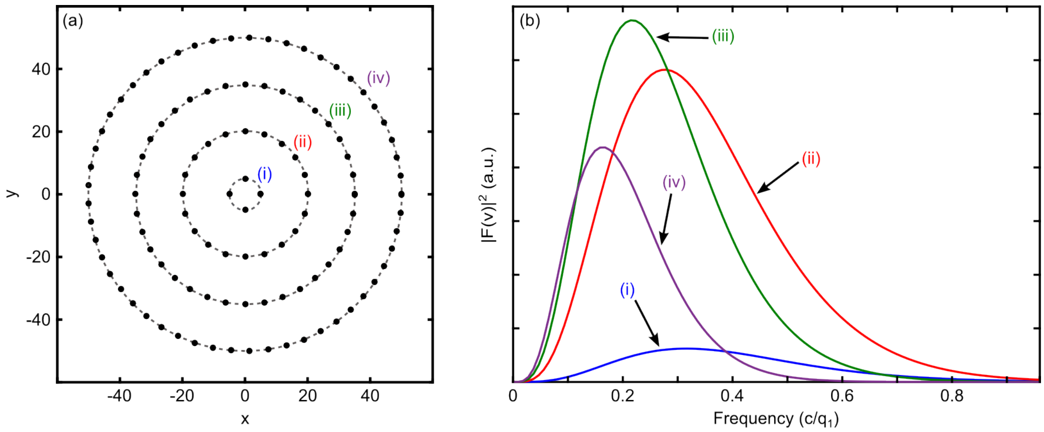

Figure 6.4: ***Metamaterial dipole array positions and excitation for generation of a single “focused doughnut”.*** *(a) shows the xy positions of the azimuthally-aligned dipoles in the generator array. There are 117 dipoles in total, located on four concentric rings with radii (i)* $r = 5$*, (ii)* $r = 20$*, (iii)* $r = 35$*, and (iv)* $r = 50$*. (b) shows the Fourier spectra of the dipole excitations. The excitation varies as a function of radial dipole position: (i)-(iv).*

at a given position. Substituting the full expression for the electric field [Eq. 5.7], we have an expression for the ith dipole as:

$$p_{\theta,i} = -4iA\sqrt{\frac{\mu_0}{\epsilon_0}}\frac{\rho_i\left(q_1 + q_2 - 2ict\right)}{\left[\rho_i^2 + \left(q_1 + i\tau\right)\left(q_2 - i\sigma\right)\right]^3}, \tag{6.5}$$

Where $\tau = z - ct$, $\sigma = z + ct$, $q_2 = 10q_1$ and A is a constant for normalisation and to ensure unit consistency. To achieve azimuthal alignment, the alignment of the ith dipole in a Cartesian basis shall vary according to:

$$p_{x,i} = -sin(\theta_i)p_{\theta,i}, \tag{6.6}$$

$$p_{y,i} = cos(\theta_i)p_{\theta,i}, \tag{6.7}$$

Where θ is the cylindrical coordinate in the xy plane.

From this, the dipole excitation is dependent on the radial position ρ_i.This can be seen clearly in the frequency spectra of the dipole excitations at each of the four rings [Fig. 6.4(b)]. Dipoles nearer the center of the array will have radiation dominated by higher frequency components, whereas lower frequencies shall be primarily generated by the dipoles in the outer rings.

In principle, the distance from the array at which the pulse can come to focus can be tailored by the choice of dipole excitations. By mapping FD electric fields at different propagation distances to the dipoles, the generated pulse can be brought to focus an arbitrary distance from the array, providing the array is large enough to generate the pulse in its diffracted state. We chose a focal position in front of the generating at $z = 180$.

In the generation scheme described here, the interactions between dipoles in the array are neglected in order to simplify this preliminary demonstration. It is currently unclear how susceptible the generation scheme would be to perturbations due to inter-dipole interactions. These interactions will be relevant for an experimental realisation of this scheme, and will warrant further investigation. It can be noted that the effect of dipole interactions on the generated pulse could be minimised through optimising the dipole placement in the array.

6.3.2 Analysis of generated pulse

To determine the viability of our generator scheme, we evaluate the electric field intensity emitted by the array (located at $z = 0$) on an xz cross-section at multiple points in time after the initial excitation at time $t = 0$. We note that although the array will radiate identically in both positive and negative z directions, we only evaluate the response along the positive z axis for values $z = 0 \rightarrow 400$. The normalised electric field intensity maps are plotted in Fig. 6.5(a)-(d) at four different times ($t = 50/c, 150/c, 250/c$, and $350/c$). Plots of the E-field amplitude are given in Appendix E to corroborate the analysis.

The evolution of the E-field intensity distribution from the near-field of the array in (a) to the far-field can be clearly traced from these images, revealing the creation of a few-cycle pulse with toroidal topology that propagates with a speed c away from the array. As anticipated, the field intensity is vanishing on axis at $x = 0$, owing to destructive interference between the fields from the azimuthally aligned dipoles in the array. These E-field intensity traces can be compared with FD pulses evaluated in Chapter 5, specifically Fig. 5.7(d) which shows the energy distribution of a simulated FD pulse. It can be seen that qualitivley there is a good match between these energy distributions.

It can be further noted that between $t = 150/c$ and $t = 350/c$ i.e between Figs. 6.5(b) and (d), the generated pulse undergoes a transformation between $1\frac{1}{2}$ cycle and single cycle. This correlates well with our analysis of the analytic FD pulse's spatiotemporal transformations recorded in Section 5.4, and reinforces the viability of this generation scheme.

The generated pulse can be further analysed by considering time traces of the E_field at several positions on the x-axis. This is motivated by the spatially-varying Fourier spectrum of the ideal FD pulse discussed in detail in Section 5.3.2. Time traces of the E-field intensity are evaluated at $z = 250$ i.e. Fig. 6.5(c), at x positions of 10,20, and 30. [Fig. 6.5(e)]. It can be clearly seen that the time traces vary as a function of radial

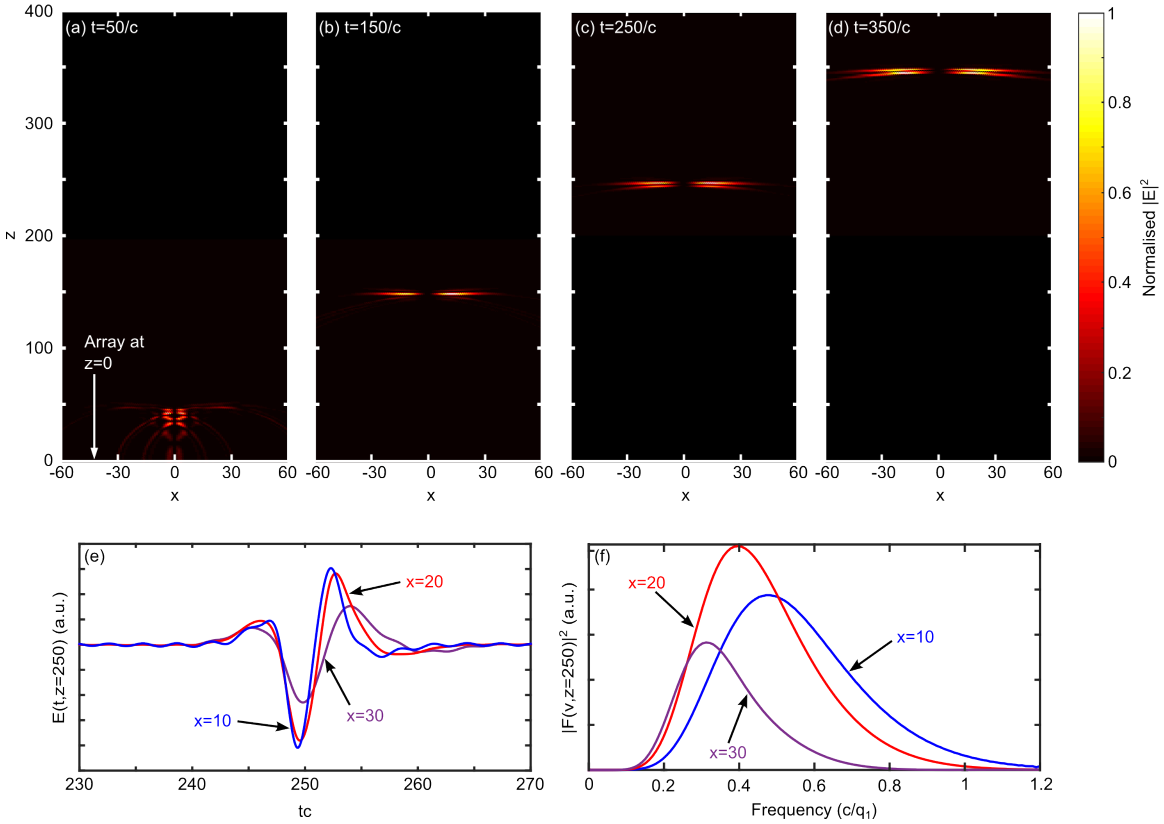

Figure 6.5: ***Generation of a single "focused doughnut" from a metamaterial dipole array.*** *This figure illustrates the excitation of a dipole array located a* $z = 0$ *resulting in a "focused doughnut" pulse in the far field. (a-d) depict the normalised E-field intensity on an* xz *cross-section in front of the dipole array. Four successive time shots show the evolution of the E-field as it propagates away from the array. (e-f) show respectively the time trace and Fourier spectrum of the E-field at* $z = 250$ *i.e. the field in (c). These are evaluated at three different* x *positions:* $x = 10, 20, 30$.

position as anticipated, with the shortest duration time trace being at $x = 10$ i.e. the smallest examined x position. Examining the Fourier spectra generated from these E-field time traces highlights this radial variation [Fig. 6.5(f)], with higher frequency components dominating the generated pulse at low x values, whilst lower frequencies dominate for larger x. This matches well with our analysis of the ideal FD pulse in Section 5.3.2.

In addition, we note that the time traces at the three different x-positions in Fig. 6.5(e) are slightly offset with respect to one-another, indicating a slight curvature to the wavefront. This is expected given that the designed focusing point of the generated pulse was $z = 180$ and so some small wavefront curvature is anticipated after propagation past this point. This holds for an ideal FD pulse, even in the well-collimated $z < q_2$ regime.

From these results, it can be seen that the designed generator array can create localised toroidal pulses that qualitatively match the ideal FD pulses in the far-field. In the following section, a more quantitative analysis to measure the correlation between the ideal FD pulse and the generated pulse shall be presented.

6.3.3 Figure of merit for pulse generation scheme

With the previous section establishing our generation scheme as a viable method for creating FD pulses, it is important to introduce a means of quantifying the correlation between our generated pulses and ideal analytic FD pulses i.e. a *figure of merit* (FOM).

We anticipate discrepancies between our generated pulses and the ideal FD pulse for several reasons. Firstly, the discretisation of the excitation into a finite number of dipoles in both the radial (in terms of the number of concentric rings rings) and azimuthal directions, leads to artifacts in the resultant pulse due to the inhomogeneous radiation pattern of electric dipoles. Secondly, the finite number of concentric rings and finite radial extent of the dipole array has implications for the frequency spectrum of the resultant pulse, owing to the space-time non-separability of the ideal FD pulse. This is anticipated to be particularly relevant for low frequency components of the FD pulse, which are dominant at large radii. The absence of dipoles in the array at these large radii could cause the Fourier spectrum of the generated pulse to differ substantially from the ideal FD pulse at low frequencies. The absence of frequency components could further manifest in differences from the focusing properties of the ideal FD, again owing to space-time non-separability.

We define the FOM for our FD generator scheme in terms of the electric fields of an ideal analytic FD pulse E_a and that created by our generator scheme E_g:

$$FOM = \frac{\langle E_a|E_g\rangle}{\left[\langle E_a|E_a\rangle \langle E_g|E_g\rangle\right]^{1/2}}, \tag{6.8}$$

Where the inner product is defined as:

$$\langle E_i|E_j\rangle = \int\int\int E_i \cdot E_j^* d\rho dt dz. \tag{6.9}$$

This allows comparison of the ideal FD pulse with or generated pulse for all simulated points in space and time. We note that by virtue of also integrating over the propagation direction z, an evaluation of the generated vs. ideal pulse diffraction is also implicitly considered. The FOM can take values $0 \rightarrow 1$, with 1 representing the case where E_a and E_g are identical. Necessarily, the FOM will be complex valued to represent any differences in phase between the ideal and generated pulse. The FOM can be equivalently defined in the frequency domain by using:

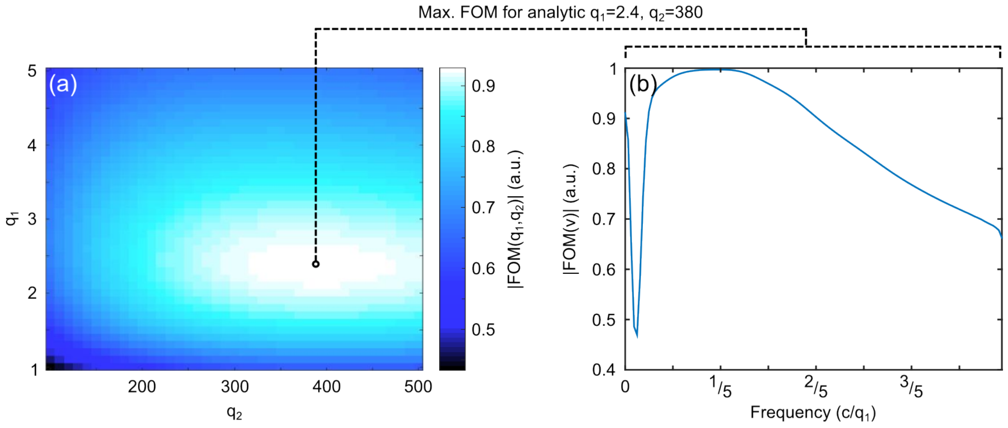

Figure 6.6: ***Figure of merit for generation of a single "focused doughnut".*** *This figure compares generated and analytic "focused doughnut" pulses to establish the FOM for the generation scheme. (a) evaluates the absolute value of the FOM [Eq. 6.8] for the generated pulse and analytic pulses with a range of q_1 and q_2 parameters. The maximum FOM is found for an analytic pulse with $q_1 = 2.4$ and $q_2 = 380$. (b) shows this maximum FOM case evaluated across the frequency components of the pulse.*

$$\left\langle \tilde{E}_i | \tilde{E}_j \right\rangle = \int \int \int \tilde{E}_i \cdot \tilde{E}_j^* d\rho d\nu dz. \tag{6.10}$$

As mentioned previously, the limitations of our generator scheme could affect the focusing properties of the generated pulse relative to an ideal FD. As such, it is feasible that the input q_1 and q_2 parameters used to characterise the array excitation will not correspond to the best fit q_1 and q_2 parameters for the generated pulse. To account for this, we comparing the generated pulse against a range of ideal FD pulses with varying q_1 and q_2 parameters, and evaluate the FOM in each case. We evaluate this for $q_1 = 1 \rightarrow 5$ and $q_2 = 100 \rightarrow 500$.

The results of this are plotted in Fig. 6.6(a), illustrating the absolute value of the FOM when using this range of ideal FD pulses as comparison points. It can be seen the maximum FOM is obtained when the generated pulse is compared to an ideal FD pulse with parameters $q_1 = 2.4$ and $q_2 = 380$. Here the absolute value of the FOM is ≈ 0.93, indicating a 93% match between the generated pulse and the ideal FD pulse. It can be noted that these best-fit values for q_1 and q_2 are different from those used as inputs for the dipole excitation ($q_1 = 3.6$ and $q_2 = 100q_1$), which gives a FOM value of ≈ 0.8 only, and reinforces the theory that truncating the array size and using a discrete number of concentric rings alters the focusing properties of the generated pulse.

Taking these best-fit ideal FD pulse parameters as $q_1 = 2.4$ and $q_2 = 380$, we can evaluate the FOM for this case as a function of frequency. This is achieved by only integrating over the spatial components of the inner product in Eq. 6.10. This then yields FOM(ν), from which the frequency components of the ideal FD pulse that are best recreated by the generator scheme can be determined.

Fig. 6.6(b) shows the absolute value of the frequency dependent FOM when comparing the generated pulse with the best-fit ideal FD pulse. It can be seen that the FOM approaches its maximum value of 1 in the region around the central frequency of the FD pulse where the majority of the energy is contained. For lower and higher frequencies however, the FOM decreases. This decrease is particularly rapid for the lower frequency components which are dominant at large radii. This can be understood as a consequence of the finite size of the generating array, and so lower frequency components that dominate at large radii are not fully reproduced by the generating scheme. As $\nu \to 0$, the FOM increases again as a consequence of the Fourier spectra of both the generated and ideal FD pulse tending to 0 for $\nu \to 0$.

Overall, it can be concluded that our scheme can accurately (to 93%) generate FD pulses, although not the FD pulse intended by the input parameters. A thorough study of the metasurface array size and the location and distribution of dipoles within the array would be necessary to evaluate fully how this discrepancy between input and output arises.

6.4 Generating a single “focused doughnut” pulse with a truncated bandwidth

Having demonstrated in the previous section that individual FD pulses can be created from a metamaterial generator arry with a good degree of accuracy, our attention now turns to practical considerations. The primary concern in this respect is how susceptible the generation scheme is to bandwidth limitations.

A key property of the FD pulses are their broadband frequency spectrum, which extends beyond that for conventional few-cycle optical pulses. This bandwidth would be challenging to accurately recreate in an experimental environment, owing to the difficulty of engineering resonators with such a broad resonance profile.

Following from this, it is important to evaluate how susceptible our FD generation scheme is to having the bandwidth truncated and what discrepancies arise in the spatiotemporal structure of the generated pulse.

6.4.1 Truncating the bandwidth of the dipole excitations

To test the limitations of our generation scheme, we consider the same same dipole array configuration used in the previous section [Fig. 6.7(a)]. We initally chose an excitation for this array identical to that used in Fig. 6.4(b), with parameters $q_1 = 3.6$ and $q_2 = 100q_1$. We note that this choice of input parameters does not necessarily correlate with the generated pulse, as established in section 6.3.3.

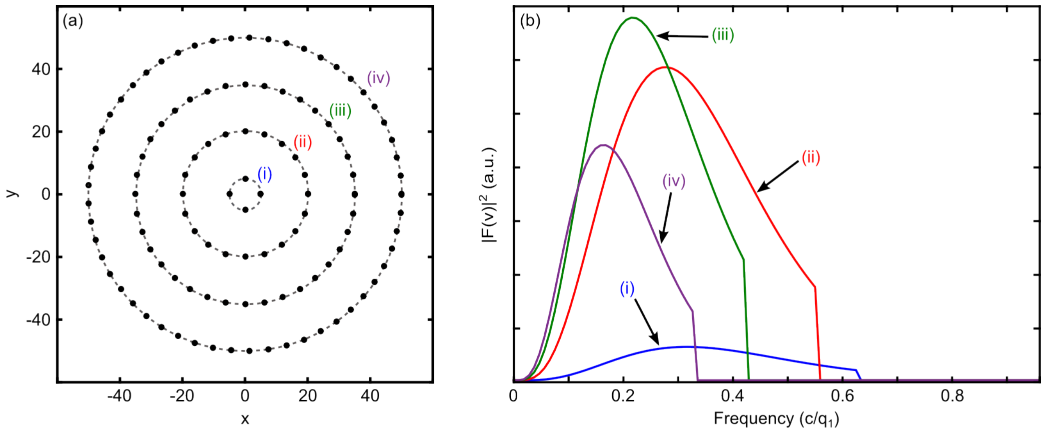

Figure 6.7: ***Metamaterial dipole array positions and excitation for generation of a single “focused doughnut” with truncated bandwidth.*** *(a) shows the xy positions of the azimuthally-aligned dipoles in the generator array. There are 117 dipoles in total, located on four concentric rings with radii (i)* $r = 5$*, (ii)* $r = 20$*, (iii)* $r = 35$*, and (iv)* $r = 50$*. (b) shows the Fourier spectra of the dipole excitations. The excitation varies as a function of radial dipole position: (i)-(iv). A cutoff frequency dependent on the peak frequency has been applied to the excitations of each ring.*

We now apply a bandwidth truncation scheme to these excitation spectra in order to determine the effect of reducing bandwidth on the generated pulse. We restrict ourselves to truncation at the high frequency end of the spectrum as the Fourier spectra [Fig. 6.5(f)] and the FOM analysis of the generated pulse in the previous section has indicated that the finite width of the generator array already results in a significant reduction in the low frequency components compared to the ideal pulse.

We chose to modify each of the excitation spectra as a function of their peak frequency ν_0, truncating the spectra such that they are only non-zero between frequencies of $\nu = 0 \rightarrow 2\nu_0$. This reflects four individual dipole resonators, each with their own maximum frequency that can be generated. This is shown in Fig. 6.7(b), which clearly illustrates the sharp cutoff to each excitation spectrum at a frequency of $2\nu_0$.

6.4.2 Analysis of generated pulse

To evaluate the generated pulse, we again consider the electric field intensity emitted by the array (located at $z = 0$) on an xz cross-section at multiple points in time after the inital excitation at time $t = 0$. The normalised electric field intensity maps are plotted in Fig. 6.8(a)-(c) at four different times ($t = 150/c, 250/c$, and $350/c$).

Whilst the generated here shares similarities with the pulse generated in the previous section [Fig. 6.5], there are some important differences. The toroidal topology of the generated pulse is retained, as is the few cycle nature. However, it is important to note the difference in effective width of this new pulse, which is significantly wider

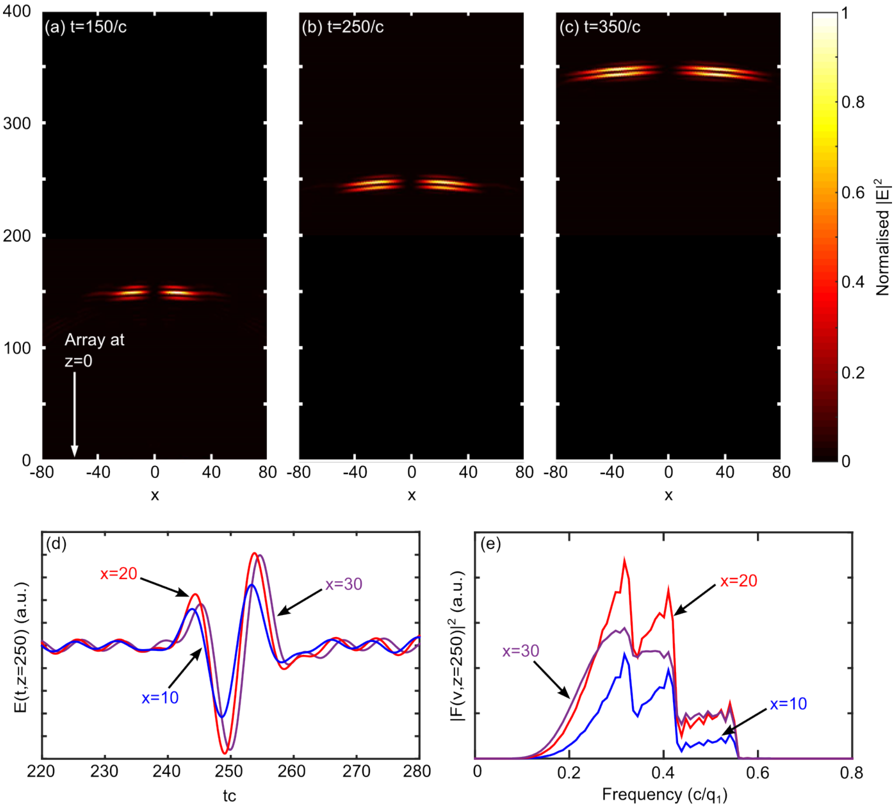

Figure 6.8: ***Generation of a single "focused doughnut" pulse from a metamaterial dipole array with truncated bandwidth.*** *This figure illustrates the excitation of a dipole array located a* $z = 0$ *resulting in a "focused doughnut" pulse in the far field. (a-c) depict the normalised* E*-field intensity on an* xz *cross-section in front of the dipole array. Four successive time shots show the evolution of the* E*-field as it propagates away from the array. (d-e) show respectively the time trace and Fourier spectrum of the* E*-field at* $z = 250$ *i.e. the field in (b). These are evaluated at three different* x *positions:* $x = 10, 20, 30$.

than in the case of no bandwidth truncation. This can be attributed to the complex spatiotemporal coupling of the FD pulse, whereby changing the frequency content of the pulse can be expected to effect the spatial focusing of the pulse.

In addition to the change in the spatial structure of the generated pulse, truncating the bandwidth also affects the temporal extent of the pulse. This can be seen in Fig. 6.8(d), which gives time traces of the E-field intensity are evaluated at $z = 250$ i.e. Fig. 6.8(b), at x positions of 10,20, and 30 [Fig. 6.8(d)]. It can be clearly seen that the generated pulse is no longer single cycle as in the non-truncated case in Fig. 6.5(e), but has no become closer to 2 cycles in nature, reflecting the significant reduction in available bandwidth. Additionally, the levels of noise at the head and tail of the pulse have now significantly increased relative to the non-truncated case.

Evaluating the Fourier spectra of these time traces [Fig. 6.8(e)] reveals how the bandwidth of the generated pulse is significantly reduced compared to the non-truncated pulse [Fig. 6.5(f)]. It can also be noted that the variation in frequency content as a function of position i.e. spatiotemporal coupling is no longer as pronounced as it was in the non-truncated case, with a series of peaks occurring in approximately the same location at each radial position.

This analysis outlines the susceptibility of the generation scheme to bandwidth limitations, and illustrates how a pulse generated from such a scheme would depart from the ideal FD case. Despite this, the generated pulse here still retains key properties such as few-cycle nature, broad bandwidth, and toroidal topology that would make it a desirable goal for a proof-of-principle experimental measurement. It is feasible that by optimising the positioning of the dipole resonators in the array, the effect of bandwidth truncation could be reduced or minimised. One potential way to achieve this would be by increasing the dipole density at low radii where high frequency components dominate, offsetting the bandwidth truncation at larger radii.

6.5 Generating a train of "focused doughnut" pulses

So far in this chapter, our consideration has been towards the generation of FD pulses in a single shot procedure. In this section, we shall examine the viability, and pros and cons, of a procedure that generates a FD pulse train rather individual processes. This would result in a system analogous to mode-locked lasers, but generating a a periodic train of FD pulses with some characteristic time separation.

6.5.1 Metamaterial pulse generator and dipole excitations

We begin with the same dipole array configuration used in previous sections for successful generation of individual FD pulses [Fig. 6.9(a)]. Generation of a train of pulses requires a modification of the excitation spectra of the array dipoles. We define the dipole excitation required to produce such a pulse train as being proportional to the sum of 4 FD fields, offset from each other in time by a factor of t_0:

$$p_i(t) \propto E_\theta(\rho_i, t) + E_\theta(\rho_i, t - t_0) + E_\theta(\rho_i, t - 2t_0) + E_\theta(\rho_i, t - 3t_0). \tag{6.11}$$

We define the $q_1 = 3.6$ and $q_2 = 100q_1$ as before, and define $t_0c = 60$ to ensure that separate FD pulses can be easily distinguished.

Fig. 6.9(b) shows the Fourier spectrum of this dipole excitation on each of the four concentric rings in the array. The distinction from the excitations required for an individual FD pulse [Fig. 6.4] is readily apparent. The frequency spectrum now takes on the form of a frequency comb spectrum, with the original FD pulse spectrum being restricted to a discrete series of peaks with equal separation. This significantly reduces

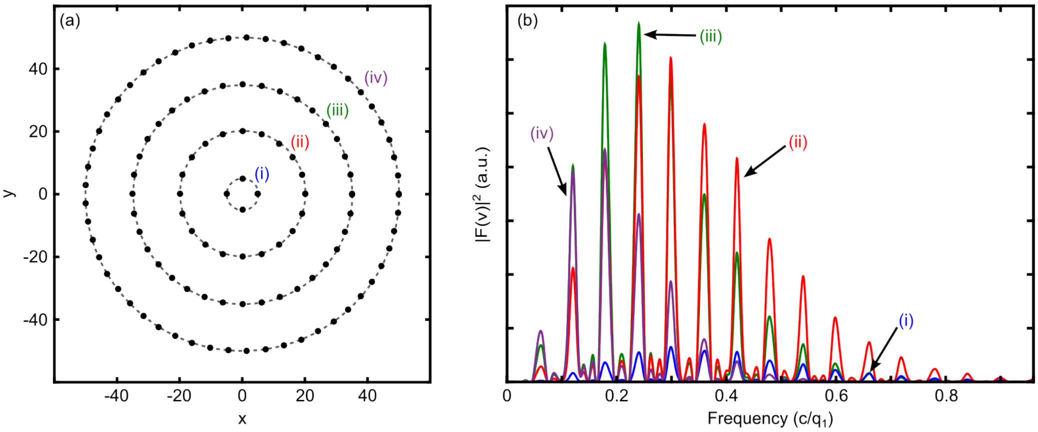

Figure 6.9: ***Metamaterial dipole array positions and excitation for generation of a train of “focused doughnut” pulses.*** *(a) shows the xy positions of the azimuthally-aligned dipoles in the generator array. There are 117 dipoles in total, located on four concentric rings with radii (i)* $r = 5$*, (ii)* $r = 20$*, (iii)* $r = 35$*, and (iv)* $r = 50$*. (b) shows the Fourier spectra of the dipole excitations. The excitation varies as a function of radial dipole position: (i)-(iv).*

the frequency components required for generation of the FD pulses, with only those coinciding with peaks in the frequency comb being significant in magnitude.

This distinction between the Fourier spectra required for individual FD generation and generation of a train of pulses, may have important implications for an experimental generator setup. In particular, it will be relevant for practical design of the resonators in the metamaterial array. This will depend on whether it is more advantageous or feasible to use individual broadband resonators, or a series of discrete narrow bandwidth resonators.

6.5.2 Analysis of generated pulse

Following the same procedures as in the previous sections, we evaluate the radiation from the excited dipole array [Fig. 6.9] in the time domain and observe the resultant pulses generated. Fig. 6.10 shows the normalised E-field intensity generated by the array on an xz cross-section at a time $t = 150/c$. It is immediately clear that multiple FD pulses have been generated my this methodology, with the first two pulses in the train visible at $z = 150$ and 90, and the third pulse forming in the near field of the array. The successive pulses travel independently, coming to focus at $z = 180$, and are sufficiently separated from each other in time and space that there is no interference between them.

The individual pulses in the train are directly analogous to those presented in Section 6.3 from the single shot process. As such it is known from the FOM analysis [Section 6.3.3] that these pulses approach a 93% match with the ideal FD pulse, albeit with different q_1 and q_2 parameters from those used in the input.

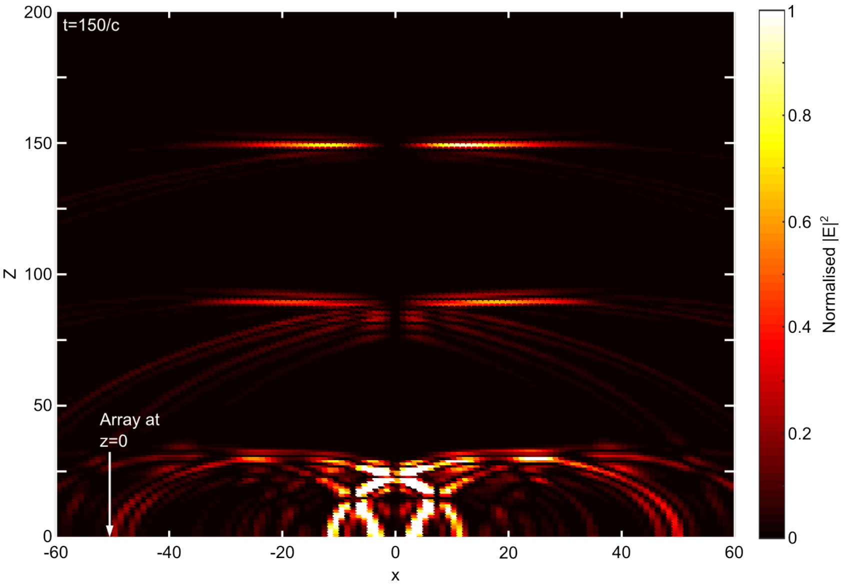

Figure 6.10: ***Generation of a train of “focused doughnut” pulses from a metamaterial dipole array.*** *This figure illustrates the excitation of a dipole array located a $z = 0$ resulting in a train of“focused doughnut” pulses in the far field. Depicted is the normalised E-field intensity on an xz cross-section in front of the dipole array at a time of $t = 150/c$.*

Analysis reveals that at the temporal separation defined here, the FOM of a given pulse in the train is not significantly affected by noise from the tail of the preceding pulses (such noise can be seen in teh time traces of Fig. 6.5(e)). It is anticipated that for decreased temporal separation of the pulses in the train, this noise will begin to have a more significant affect. Further studies could benefit from understanding the limits for temporal separation in such a pulse train.

6.5.3 Comparing single shot and pulse train “focused doughnut” generators

In this section, we will contrast the pros and cons of the single shot FD generation scheme presented in Section 6.3 with the pulse train generation scheme described here. From an application perspective, both single shot pulses and pulse trains find a range of applications throughout physics, with pulse trains being of particular use in the field of metrology [225, 226].

In terms of experimental feasibility, the potential of both schemes becomes a question of feasible resonator bandwidths. In the case of a single shot generation scheme, Fig. 6.4(b) indicates that generation of a single FD pulse would require highly broadband resonators with > one octave bandwidth compared to the peak frequency. Accurate control of frequency across such a bandwidth represents a daunting task, although our work in Section 6.4 reveals that some bandwidth limitations could be tolerated in such a scheme. In comparison, whilst generating a single FD pulse requires a continuous bandwidth, generating a train of FD pulses requires only multiple narrow-band peaks as per a frequency-comb structure [Fig. 6.9(b)]. In the case of an experimental array design, this could correspond to a series of narrowband resonators with different peak-frequencies co-located in space (i.e. closely spaced on a sub-wavelength scale). In such a configuration, coupling between resonators could become a potential issue. Attaining narrowband dipole radiation could also be challenging, but could be addressed by coupling the dipole to a sub-radiant quadrupole mode [80]. This would come at the expense of complicating the resonator design beyond the simple dipolar case.

6.6 Summary

In this chapter, we have provided a proof-of-principle numerical demonstration for the generation of “focused doughnut” pulses from discrete dipole arrays. In particular, we utilise a planar array of dipole resonators arranged in a series of concentric rings where each dipole can be individually orientated and assigned a specific temporal excitation. Study of the radiation from this array in the far-field reveals that the generated pulse can match an ideal FD pulse to a 93% accuracy. The focusing point of this pulse can be altered arbitrarily by tailoring the input parameters.

Further to this, we evaluated the susceptibility of the generator scheme to bandwidth limitations that will likely form a key consideration of any experimental realisation. Simulations indicate that truncating the available bandwidth does affect the coupled spatiotemporal structure of the pulse, but key properties of the ideal “focused doughnut”; such as spatiotemporal coupling, few cycle nature, and toroidal topology; are still present. This represents a more realistic outcome of an initial experimental FD generator scheme.

Finally, it is demonstrated that by applying a frequency-comb like structure to the dipole excitations, the generating array can be tailored to generate a train of “focused doughnut” pulses with an arbitrary separation in time. These individual pulses do not interfere with each other and can each be matched to an ideal FD pulse with a 93% accuracy.

The results presented here in this chapter lend support to the feasibility of producing “focused doughnut” pulses using a metamaterial paradigm. However, there remain several key questions to answer. Owing to the discrepancy between the desired pulse parameters and those of the generated pulse [Section 6.3.3], the direct relationship between the positioning of dipoles in the metamaterial array and the resultant spatiotemporal structure of the pulse requires a thorough analysis. It may be that there is some array configuration that could achieve an optimum matching between input and output parameters, which may be greater than the 93% match achieved here. Furthermore, it would be beneficial to characterise the maximum bandwidth truncation that can be tolerated in such a generation scheme before key properties of the FD pulse are lost. This would give the lower bounds for the tolerances of an experimental generator scheme.

Chapter 7

Conclusions

7.1 Summary

The aim of this thesis was to explore the various manifestations of toroidal electrodynamics in free-space, matter, and metamaterial structures. The results presented here are anticipated to pave the way towards practical applications of toroidal electrodynamics, particularly in the fields of sensing, spectroscopy and communications.

Prior to the work presented here, toroidal responses had been identified as a key component in the excitations of metamaterial structures across a variety of spectral ranges. In this thesis a number of theoretical and experimental advances have been made concerning toroidal responses in matter:

- The first instance of a chiral metamaterial structure that exhibits circular dichroism due to the simultaneous excitation of an electric quadrupole and a toroidal dipole. We term this new enantiomeric phenomenon **toroidal circular dichroism**.
- A methodology for determining the **microscopic origin of chirality in metamaterial structures**. The approach is based on evaluating changes to a material's polarisation eigenstates upon removal of radiating multipole components.
- A **toroidal scatterer** that can be excited by **radially polarised light**, and exhibits a high Q-factor dipole radiation pattern.

Insights have also been gained concerning the "focused doughnut" pulse. These theoretical pulses with a complex toroidal topology are as yet unsynthesised and are hypothesised to lead to non-trivial light-matter interactions. Numerous results have been presented in this thesis:

- First instance of a full 3D finite element **simulation of "focused doughnut" pulses**.
- Simulations of "focused doughnut" pulses **interacting with continuous interfaces**, including observation of these pulses under reflection and refraction.

- Simulations of “focused doughnut” pulses **interacting with particulate matter** with spherical and toroidal topologies. Explicit observation of broadband modal excitation, **preferential excitation of toroidal multipoles**, and excitation of a **quasi-anapole mode**.

Finally, potential schemes for generating “focused doughnut” pulses have been investigated with the aim of achieving a physical realisation of these pulses. Key results include:

- Demonstration of **“focused doughnut” pulses generated from a metamaterial dipole array**. The generated pulse can achieves a 93% match with the analytic pulse. The effects of **truncating the bandwidth** of the dipole array on the generated pulse were studied.
- Utilising a **frequency-comb-like** excitation spectra to generate a **train of “focused doughnut” pulses** form a metamaterial array.

7.2 Outlook

The work presented in this thesis covers a broad range of topics in toroidal electrodynamics, including both experimental and proof-of-principle numerical demonstrations of intriguing phenomena in matter, metamaterials, and free-space. There is significant scope for continued research in all the topics discussed in the previous chapters. Some of the suggestions for future research will be discussed below.

The mechanism of toroidal circular dichroism identified in Chapter 3 of this thesis, represents a new, previously unobserved, microscopic mechanism for optical activity in matter. We argue that this mechanism should be routinely taken into account in the interpretation of circular dichroism spectra as an extension of the textbook descriptions of conventional optical activity. This particularly relevant in the case of the many biological and chemical structures that exhibit both toroidal topology and an enantiomeric structure.

In Chapter 4, the interaction between radially polarised vector beams and toroidal scatterers was described. The demonstration of high-quality toroidal responses in the scatterer presents a new avenue for exciting and probing toroidal structures, and generating high-quality dipole radiation. Furthermore, the work here reinforces the preferential coupling of radially polarised light to the toroidal multipoles. Further work could seek to examine the excitation of toroidal modes with more complex vector beams, such as optical vorticies.

The research conducted on the properties, interactions, and generation of “focused doughnut” pulses, reported on in Chapter 5 and 6, offers a variety of avenues for future research, both in terms of continued numerical analysis and experimental work.

There remains a wealth of interactions scenarios that would expand knowledge of the light-matter interactions of these complex pulses. An example of this would be the viability of a guiding mechanism for FD pulses. This could take the form of waveguiding mechanisms in matter [172, 206], or guiding along metallic wires, as has been demonstrated in the Terahertz regime [227]. Demonstration of guided FD propagation would make the pulse increasingly viable as a new form of information carrier and would be of particular interest to the telecommunications industry. A demonstration of of FD stability whilst propagating through non-ideal environments would also be instructive for this aim. Examples of such environments would include dispersive media and media with noise-like fluctuations in refractive index, reflecting variations in air density and dust in an experimental setting.

Further light-matter interactions of interest would include optimal absorption of FD pulses, with respect to energy harvesting and detection applications; interaction with non-linear media, taking advantage of the highly localised energy density of the pulse to drive non-linear processes; and the hypothetical excitation of space-time non-separable electromagnetic “bursts” in matter, dispersive media, and plasmas.

Following on from our work in Chapter 6, an ultimate aim would be the experimental demonstration of the generation, transmission, and detection of a FD pulse. A generator system would be based on the proof-of-principle metasurface scheme presented here in this thesis. A full experimental realisation of a conventional-to- FD-pulse metasurface transformer would require further investigation of broadband light manipulation and polarisation conversion techniques. Both the Terahertz and optical regimes have been considered for experimental work, with the Terahertz benefiting from the ubiquity of broadband pulses in this regime and relative ease of fabricating sub-wavelength structures on this scale. Fabrication and attaining broadband light manipulation would be more challenging in the optical regime, but would open up more possible applications, for example spectroscopy, optical manufacturing techniques, and telecommunications.

Detection schemes could be based on the generator, or take advantage of the interactions described in Chapter 5. This could include detectors sensitive to the dominant excitation of toroidal modes, or detectors sensitive to the strong longitudinal field component of the FD pulse. A combination of generators and detectors could form the basis for integrated FD line-of-sight communication and directed energy transfer systems.

Appendix

A Interaction energies of multipoles

In this Appendix, the interactions energies of the electric, magnetic, and toroidal dipoles shall be calculated. Note that CGS units are used here to be consistent with the relevant literature.

We begin from the definition of the electromagnetic interaction energy W:

$$W = \int d^3r \left[\rho\phi - \frac{1}{c}\mathbf{J}\cdot\mathbf{A}\right]. \tag{A.1}$$

The relevant charge ρ and current $\mathbf{J}$ densities for the specific multipoles can then be inserted.

A.1 Interaction energy of the electric dipole

It can be shown that the charge-current density corresponding to an infinitesimally small electric dipole $\mathbf{p}$ located at the origin is given by [42]:

$$\rho(\mathbf{r}) = -\mathbf{p}\cdot\nabla\delta^{(3)}(\mathbf{r}), \tag{A.2}$$

$$\mathbf{J}(\mathbf{r}) = \frac{\partial\mathbf{p}}{\partial t}\delta^{(3)}(\mathbf{r}). \tag{A.3}$$

Substituting these definitions into Eq. A.1 gives:

$$W_p = \int d^3r \left[\left(-\mathbf{p}\cdot\nabla\delta^{(3)}(\mathbf{r})\right)\phi - \frac{1}{c}\frac{\partial\mathbf{p}}{\partial t}\cdot\mathbf{A}\delta^{(3)}(\mathbf{r})\right]. \tag{A.4}$$

The first term in the square brackets can be shown to be equivalent to:

$$W_p = \int d^3r \left[-\mathbf{p}\cdot\nabla\phi\delta^{(3)}(\mathbf{r}) - \frac{1}{c}\frac{\partial\mathbf{p}}{\partial t}\cdot\mathbf{A}\delta^{(3)}(\mathbf{r})\right]. \tag{A.5}$$

Integrating over the delta functions and substituting $\mathbf{E} = -\nabla\phi - \frac{1}{c}\frac{\partial\mathbf{A}}{\partial t}$ then yields:

$$W_p = -\mathbf{p}\cdot\mathbf{E} - \frac{1}{c}\frac{\partial}{\partial t}\left(\mathbf{p}\cdot\mathbf{A}\right). \tag{A.6}$$

As such, the electric dipole interacts with both the electric field $\mathbf{E}$ and the magnetic vector potential $\mathbf{A}$.

A.2 Interaction energy of the magnetic dipole

It can be shown that the charge-current density corresponding to an infinitesimally small magnetic dipole $\mathbf{m}$ located at the origin is given by [16]:

$$\rho(\mathbf{r}) = 0, \tag{A.7}$$

$$\mathbf{J}(\mathbf{r}) = \nabla \times \left(c\mathbf{m}\delta^{(3)}(\mathbf{r}) \right). \tag{A.8}$$

Substituting these definitions into Eq. A.1 gives:

$$W_m = -\frac{1}{c} \int d^3r \left(\nabla \times c\mathbf{m}\delta^{(3)}(\mathbf{r}) \right) \cdot \mathbf{A}. \tag{A.9}$$

This can be shown to be equivalent to:

$$W_m = -\int d^3r \, (\nabla \times \mathbf{A}) \cdot \mathbf{m}\delta^{(3)}(\mathbf{r}). \tag{A.10}$$

Integrating over the delta function and substituting $\mathbf{B} = \nabla \times \mathbf{A}$ then yields:

$$W_m = -\mathbf{m} \cdot \mathbf{B}. \tag{A.11}$$

As such, the magnetic dipole interacts with the magnetic field $\mathbf{B}$.

A.3 Interaction energy of the toroidal dipole

It can be shown that the charge-current density corresponding to an infinitesimally small toroidal dipole $\mathbf{T}$ located at the origin is given by [16]:

$$\rho(\mathbf{r}) = 0, \tag{A.12}$$

$$\mathbf{J}(\mathbf{r}) = \nabla \times \nabla \times \left(c\mathbf{T}\delta^{(3)}(\mathbf{r}) \right). \tag{A.13}$$

Substituting these definitions into Eq. A.1 gives:

$$W_T = -\frac{1}{c} \int d^3r \left(\nabla \times \nabla \times c\mathbf{T}\delta^{(3)}(\mathbf{r}) \right) \cdot \mathbf{A}. \tag{A.14}$$

This can be shown to be equivalent to:

$$W_T = -\int d^3r\,(\nabla \times \nabla \times \mathbf{A}) \cdot \mathbf{T}\delta^{(3)}(\mathbf{r}). \tag{A.15}$$

Integrating over the delta function and substituting Ampere's Law then yields:

$$W_T = -\mathbf{T} \cdot \left[\frac{4\pi}{c}\mathbf{J} + \frac{1}{c}\frac{\partial \mathbf{E}}{\partial t}\right]. \tag{A.16}$$

As such, the toroidal dipole interacts with the current $\mathbf{J}$ and the time derivative of the electric field $\partial \mathbf{E}/\partial t$.

B Radiation patterns of multipoles

In this Appendix the far-field radiation distributions of the first few orders of multipoles shall be constructed. Note that SI units shall be used here to be consistent with the relevant literature.

We begin with the solutions for scalar ϕ and vector $\mathbf{A}$ potentials of an arbitrary charge ρ and current $\mathbf{J}$ distribution based on the Green's function:

$$\phi(\mathbf{r}) = \frac{1}{4\pi\epsilon_0}\int \frac{e^{i\mathbf{k}|\mathbf{r}-\mathbf{r}'|}}{|\mathbf{r}-\mathbf{r}'|}\rho\left(\mathbf{r}'\right) d^3r', \tag{B.1}$$

$$\mathbf{A}(\mathbf{r}) = \frac{\mu_0}{4\pi}\int \frac{e^{i\mathbf{k}|\mathbf{r}-\mathbf{r}'|}}{|\mathbf{r}-\mathbf{r}'|}\mathbf{J}\left(\mathbf{r}'\right) d^3r'. \tag{B.2}$$

These solutions to the inhomogenous wave equation are constructed using the Lorenz Gauge for the vector potential $\mathbf{A}$:

$$\nabla \cdot \mathbf{A} - \frac{1}{c^2}\frac{\partial \phi}{\partial t} = 0 \tag{B.3}$$

The electric E and magnetic fields can then be constructed using the following relations:

$$\mathbf{E} = -\nabla\phi - \frac{\partial \mathbf{A}}{\partial t}, \tag{B.4}$$

$$\mathbf{B} = \nabla \times \mathbf{A}. \tag{B.5}$$

At this point we emphasise that only far-field (i.e. as $r \to \infty$) radiation components are considered in the following derivations, and as such consider only terms of order $O\left(1/r\right)$. In practice, the full expressions for the radiated fields contain terms dependent on higher order powers of r.

In addition, source terms $\propto \delta(\mathbf{r})$ that characterise the behaviour of the fields at the origin are ommited from the following derivations. These arise from a complete differentiation of the term $\left(\frac{e^{ikr}}{r}\right)$, and ensure the full field expressions satisfy Maxwell's equations for a radiating source. For example, the full **E**-field of a radiating electric dipole **p** contains a term $\propto \mathbf{p}\delta(\mathbf{r})$. For a full description of the complete field expressions for radiating dipoles and a discussion of the relevance of source terms, the reader is directed to references [9, 228, 229].

B.1 Radiation of the electric dipole

It can be shown that the charge-current density corresponding to an infinitesimally small electric dipole **p** located at the origin is given by:

$$\rho(\mathbf{r}) = -\mathbf{p} \cdot \nabla \delta^{(3)}(\mathbf{r}), \tag{B.6}$$

$$\mathbf{J}(\mathbf{r}) = -i\omega \mathbf{p} \delta^{(3)}(\mathbf{r}). \tag{B.7}$$

We note that this identity is consistent with both the continuity equation $i\omega\rho + \nabla \cdot \mathbf{J}$ and the definition for electric dipole in terms of a current integral in Section 2.2.1. These definitions for ρ and $\mathbf{J}$ can be inserted into Eqs. B.1 and B.2. First ϕ is calculated:

$$\phi_p(\mathbf{r}) = \frac{1}{4\pi\epsilon_0} \int \frac{e^{i\mathbf{k}|\mathbf{r}-\mathbf{r}'|}}{|\mathbf{r}-\mathbf{r}'|} \left[-\mathbf{p} \cdot \nabla' \delta^{(3)}(\mathbf{r}') \right] d^3r' = \frac{1}{4\pi\epsilon_0} \mathbf{p} \cdot \int \nabla' \frac{e^{i\mathbf{k}|\mathbf{r}-\mathbf{r}'|}}{|\mathbf{r}-\mathbf{r}'|} \delta^{(3)}(\mathbf{r}') d^3r'.$$

This can be shown to be equivalent to:

$$\phi_p(\mathbf{r}) = \frac{1}{4\pi\epsilon_0} \mathbf{p} \cdot (-\nabla) \int \frac{e^{i\mathbf{k}|\mathbf{r}-\mathbf{r}'|}}{|\mathbf{r}-\mathbf{r}'|} \delta^{(3)}(\mathbf{r}') d^3r' = -\frac{1}{4\pi\epsilon_0} \mathbf{p} \cdot \nabla \frac{e^{ikr}}{r}. \tag{B.8}$$

The vector potential A is calculated to be:

$$\mathbf{A}_p(\mathbf{r}) = \frac{\mu_0}{4\pi} \int \frac{e^{i\mathbf{k}|\mathbf{r}-\mathbf{r}'|}}{|\mathbf{r}-\mathbf{r}'|} \left[-i\omega \mathbf{p} \delta^{(3)}(\mathbf{r}') \right] d^3r' = -\frac{i\omega\mu_0}{4\pi} \mathbf{p} \frac{e^{ikr}}{r}. \tag{B.9}$$

These definitions of ϕ and $\mathbf{A}$ can now be substituted into Eq. B.4, assuming harmonic excitation of the form $-\frac{\partial \mathbf{A}}{\partial t} \rightarrow i\omega \mathbf{A}$:

$$\begin{aligned}
\mathbf{E}_p(\mathbf{r}) &= -\nabla \left[\frac{1}{4\pi\epsilon_0} \mathbf{p} \cdot \nabla \frac{e^{ikr}}{r} \right] - \frac{\partial}{\partial t} \left[-\frac{i\omega\mu_0}{4\pi} \mathbf{p} \frac{e^{ikr}}{r} \right], \\
&= -\frac{1}{4\pi\epsilon_0} \nabla \left[\mathbf{p} \cdot \nabla \frac{e^{ikr}}{r} \right] + \frac{\omega^2 \mu_0}{4\pi} \mathbf{p} \frac{e^{ikr}}{r}, \\
&= \frac{c}{4\pi} \sqrt{\frac{\mu_0}{\epsilon_0}} \left[k^2 \mathbf{p} - \nabla \left(\mathbf{p} \cdot \nabla \right) \right] \left(\frac{e^{ikr}}{r} \right).
\end{aligned}$$

Evaluating the differentials and considering only $O(1/r)$, the electric field $\mathbf{E}_p$ is then defined in the far-field as:

$$\mathbf{E}_p(\mathbf{r}) = \frac{k^2 c}{4\pi}\sqrt{\frac{\mu_0}{\epsilon_0}}\left[\mathbf{p} - \hat{\mathbf{r}}\left(\mathbf{p}\cdot\hat{\mathbf{r}}\right)\right]\left(\frac{e^{ikr}}{r}\right),$$

Which can be shown to be equivalent to:

$$\mathbf{E}_p(\mathbf{r}) = \frac{k^2 c}{4\pi}\sqrt{\frac{\mu_0}{\epsilon_0}}\left(\frac{e^{ikr}}{r}\right)(\hat{\mathbf{r}}\times\mathbf{p})\times\hat{\mathbf{r}}. \tag{B.10}$$

It can be seen from the factor $(\hat{\mathbf{r}}\times\mathbf{p})\times\hat{\mathbf{r}}$ that $\mathbf{E}_p$ will be primarily aligned along the axis of the dipole.

B.2 Radiation of the magnetic dipole

It can be shown that the charge-current density corresponding to an infinitesimally small magnetic dipole $\mathbf{m}$ located at the origin is given by:

$$\rho(\mathbf{r}) = 0, \tag{B.11}$$

$$\mathbf{J}(\mathbf{r}) = \nabla\times\left(c\mathbf{m}\delta^{(3)}(\mathbf{r})\right). \tag{B.12}$$

As the charge density ρ for a magnetic dipole is zero, only the vector potential $\mathbf{A}$ is required to construct the far-field radiation. The defintiion for $\mathbf{J}$ can be inserted into Eq. B.2:

$$\mathbf{A}(\mathbf{r}) = \frac{\mu_0}{4\pi}\int\frac{e^{i\mathbf{k}|\mathbf{r}-\mathbf{r}'|}}{|\mathbf{r}-\mathbf{r}'|}\left[\nabla\times c\mathbf{m}\delta^{(3)}(\mathbf{r})\right]d^3r'. \tag{B.13}$$

By following through the integration, it can be shown that:

$$\mathbf{A}_m(\mathbf{r}) = -\frac{c\mu_0}{4\pi}\left[\mathbf{m}\times\nabla\right]\left(\frac{e^{ikr}}{r}\right). \tag{B.14}$$

The electric field $\mathbf{E}$ can then be calculated from Eq. B.4. The scalar potential $\phi = 0$ and assuming harmonic excitation of the form $-\frac{\partial\mathbf{A}}{\partial t}\rightarrow i\omega\mathbf{A}$, this gives:

$$\begin{aligned}\mathbf{E}_m(\mathbf{r}) &= -\frac{i\omega c\mu_0}{4\pi}\left[\mathbf{m}\times\nabla\right]\left(\frac{e^{ikr}}{r}\right),\\ &= -\frac{ikc}{4\pi}\sqrt{\frac{\mu_0}{\epsilon_0}}\left[\mathbf{m}\times\nabla\right]\left(\frac{e^{ikr}}{r}\right).\end{aligned}$$

Evaluating the differential and considering only $O\left(1/r\right)$, the electric field $\mathbf{E}_m$ is then defined in the far-field as:

$$\mathbf{E}_m(\mathbf{r}) = -\frac{k^2 c}{4\pi}\sqrt{\frac{\mu_0}{\epsilon_0}}\left(\frac{e^{ikr}}{r}\right)(\hat{\mathbf{r}} \times \mathbf{m}) \,. \tag{B.15}$$

It can be seen from the $(\hat{\mathbf{r}} \times \mathbf{m})$ that $\mathbf{E}_m$ in the far-field will be aligned orthogonal to the dipole axis. This is in contrast to the radiated field $\mathbf{E}_p$ from an electric dipole, which is aligned primarily along the dipole axis

B.3 Radiation of the toroidal dipole

As the expression for radiation of a toroidal dipole is not given in the standard texts, here we will provide a full derivation. We start from the charge ρ and current $\mathbf{J}$ density distributions for a toroidal dipole:

$$\rho(\mathbf{r}) = 0, \tag{B.16}$$

$$\mathbf{J}(\mathbf{r}) = \nabla \times \nabla \times \left(c\mathbf{T}\delta^{(3)}(\mathbf{r})\right), \tag{B.17}$$

Where $\mathbf{T}$ represents a toroidal dipole. As the charge density ρ of a toroidal dipole is zero, the scalar potential ϕ= 0. The vector potential $\mathbf{A}_T$ is given by:

$$\mathbf{A}_T(\mathbf{r}) = \frac{c\mu_0}{4\pi}\int \frac{e^{(ik|\mathbf{r}-\mathbf{r}'|)}}{|\mathbf{r}-\mathbf{r}'|}\left[\nabla \times \nabla \times \mathbf{T}\delta^{(3)}(\mathbf{r}')\right])d^3r'. \tag{B.18}$$

By following through the integration, it can be shown that:

$$\mathbf{A}_T(\mathbf{r}) = \frac{c\mu_0}{4\pi}\left[\nabla\left(\mathbf{T}\cdot\nabla\right) - \mathbf{T}\nabla^2\right]\left(\frac{e^{ikr}}{r}\right). \tag{B.19}$$

The electric field $\mathbf{E}$ can then be calculated from Eq. B.4. The scalar potential $\phi = 0$ and assuming harmonic excitation of the form $-\frac{\partial \mathbf{A}}{\partial t} \rightarrow i\omega\mathbf{A}$, this gives:

$$\mathbf{A}_T(\mathbf{r}) = \frac{i\omega c\mu_0}{4\pi}\left[\nabla\left(\mathbf{T}\cdot\nabla\right) - \mathbf{T}\nabla^2\right]\left(\frac{e^{ikr}}{r}\right). \tag{B.20}$$

Evaluating the differentials and considering only $O\left(1/r\right)$, the $\mathbf{E}_T$ is then defined in the far-field as:

$$\mathbf{E}_T(\mathbf{r}) = \frac{ik^3 c}{4\pi}\sqrt{\frac{\mu_0}{\epsilon_0}}\left[\mathbf{T} - \hat{\mathbf{r}}\left(\hat{\mathbf{r}}\cdot\mathbf{T}\right)\right]\left(\frac{e^{ikr}}{r}\right), \tag{B.21}$$

$$\mathbf{E}_T(\mathbf{r}) = \frac{ik^3 c}{4\pi}\sqrt{\frac{\mu_0}{\epsilon_0}}\left(\frac{e^{ikr}}{r}\right)(\hat{\mathbf{r}} \times \mathbf{T}) \times \hat{\mathbf{r}}. \tag{B.22}$$

We note that the far-field radiation pattern of the toroidal dipole has a similar structure to that of the electric dipole [Eq. B.10], save for a phase factor and additional dependence on k. Indeed for $\mathbf{p} = -ik\mathbf{T}$, the two radiation patterns will be identical. For cases $\mathbf{p} = -ik\mathbf{T}$, the radiated fields of the two multipoles will be identical in magnitude but a factor of π out of phase, leading to destructive interference. This is the basis for a non-radiating configuration and will be demonstrated explicitly in Appendix B.4.

B.4 Interference between electric and the toroidal dipole radiation

Consider the superposition of far-field toroidal dipole radiation [Eq. B.22] and far-field electric dipole radiation [Eq. B.10] where the electric dipole $\mathbf{p} = -ik\mathbf{T}$:

$$\mathbf{E}_{p+T}(\mathbf{r}) = \mathbf{E}_p(\mathbf{r}) + \mathbf{E}_T(\mathbf{r}), \tag{B.23}$$

$$\mathbf{E}_{p+T}(\mathbf{r}) = \frac{k^2c}{4\pi}\sqrt{\frac{\mu_0}{\epsilon_0}}\left(\frac{exp\,(ikr)}{r}\right)(\hat{\mathbf{r}} \times (-ik\mathbf{T}))\times\hat{\mathbf{r}} + \frac{ik^3c}{4\pi}\sqrt{\frac{\mu_0}{\epsilon_0}}\left(\frac{exp\,(ikr)}{r}\right)(\hat{\mathbf{r}} \times \mathbf{T})\times\hat{\mathbf{r}}. \tag{B.24}$$

Collecting like terms and simplifying leads to:

$$\mathbf{E}_{p+T}(\mathbf{r}) = \left[\frac{ik^3c}{4\pi} - \frac{ik^3c}{4\pi}\right]\sqrt{\frac{\mu_0}{\epsilon_0}}\left(\frac{exp\,(ikr)}{r}\right)(\hat{\mathbf{r}} \times \mathbf{T}) \times \hat{\mathbf{r}}, \tag{B.25}$$

$$\mathbf{E}_{p+T}(\mathbf{r}) = 0. \tag{B.26}$$

This demonstrates the destructive interference of the far-field radiation components i.e. a non-radiating configuration in the case of co-located and co-aligned electric and toroidal dipoles where $\mathbf{p} = -ik\mathbf{T}$.

This can be reinforced by considering the equation for multipole scattering intensity as given by Eq. 2.2.2. Considering only the terms dependent on the electric and toroidal dipole we have:

$$I_{\mathbf{p},\mathbf{T}} = \frac{2\omega^4}{3c^3}|\mathbf{p}|^2 + \frac{2\omega^6}{3c^5}|\mathbf{T}|^2 - \frac{4\omega^5}{3c^4}\mathrm{Im}\left(\mathbf{p}^\dagger \cdot \mathbf{T}\right). \tag{B.27}$$

We note that the sign of the third term has changed from positive to negative relative to Eq. 2.2.2. This is because our derivation of radiation patterns in Appendix B utilises a $-i\omega t$ harmonic convention, whereas Eq. 2.2.2 utilises a $+i\omega t$ convention. Both descriptions are valid for the correct definitions of the dipole phases.

Substituting $\mathbf{p} = -ik\mathbf{T}$ into Eq. B.27 gives:

$$I_{\mathbf{p},\mathbf{T}} = \frac{2\omega^4}{3c^3}\left|-ik\mathbf{T}\right|^2 + \frac{2\omega^6}{3c^5}\left|\mathbf{T}\right|^2 - \frac{4\omega^5}{3c^4}\mathrm{Im}\left(ik\left|\mathbf{T}\right|^2\right), \tag{B.28}$$

$$I_{\mathbf{p},\mathbf{T}} = \frac{4\omega^6}{3c^5}\left|\mathbf{T}\right|^2 - \frac{4\omega^6}{3c^5}\left|\mathbf{T}\right|^2 = 0. \tag{B.29}$$

It can be seen that the total scattering intensity of the electric and toroidal dipoles vanishes for $\mathbf{p} = -ik\mathbf{T}$.

B.5 Radiation of the electric quadrupole

The radiation pattern of the electric quadrupole is difficult to obtain using the methodology outlined in the previous sections. This is due to the complexities in writing charge density ρ and current density $\mathbf{J}$ in terms of the electric quadrupole tensor $Q_{\alpha\beta}$. Nonetheless, a definition of electric quadrupole radiation can be extracted from the multipole expansion and is well covered in the literature:

$$\mathbf{E}_Q(\mathbf{r}) = \frac{-ik^3c}{24\pi}\sqrt{\frac{\mu_0}{\epsilon_0}}\left(\frac{e^{ikr}}{r}\right)(\hat{\mathbf{r}} \times \mathbf{Q}) \times \hat{\mathbf{r}}, \tag{B.30}$$

Where Q_α is defined in terms of the electric quadrupole tensor as:

$$Q_\alpha = \sum_\beta Q_{\alpha\beta} r_\beta. \tag{B.31}$$

We refer the reader to Ref. [9] for an in-depth derivation.

C Definition of current in simulation domains

Numerical simulations in COMSOL 3.5a do not include a predefined definition of current density within a simulation domain. This is necessary in order to fully evaluate the multipoles excited in matter. Here a working definition shall be defined. We start with Ampere's circuital law (with Maxwell's addition):

$$\nabla \times \mathbf{B} = \mu_0\mathbf{J} + i\omega\mu_0\epsilon_0\mathbf{E}. \tag{C.1}$$

In COMSOL 3.5a, it is given in equivalent form as:

$$\nabla \times \mathbf{B} = \mu_0\sigma\mathbf{E} + i\omega\mu_0\epsilon_0\epsilon_r\mathbf{E}, \tag{C.2}$$

Where σ represents the electrical conductivity and ϵ_r represents the relative permittivity. Equating these two definitons gives:

$$\mu_0\mathbf{J} + i\omega\mu_0\epsilon_0\mathbf{E} = \mu_0\sigma\mathbf{E} + i\omega\mu_0\epsilon_0\epsilon_r\mathbf{E}, \tag{C.3}$$

$$\mathbf{J} = \sigma\mathbf{E} + i\omega\epsilon_0\left(\epsilon_r - 1\right)\mathbf{E}. \tag{C.4}$$

Noting that in dielectric $\sigma = 0$, we are left with the definition:

$$\mathbf{J} = i\omega\epsilon_0\left(\epsilon_r - 1\right)\mathbf{E}. \tag{C.5}$$

This can be utilised to calculate current density within simulation domains, and thus multipoles from volume rather than surface currents.

D Multipole integrals in transient simulations

The multipole integrals given in Section 2.2.1 are explicitly frequency dependent, and can be utilised to extract the microscopic multipoles from harmonic domain simulations. However, many of the simulations conducted in support of this thesis utilise transient domain simulations, specifically the research reported on in Chapter 5. As such, here the methodology for extracting frequency-dependent multipoles from transient data will be described.

Here we modify the charge-current integrals given in Section 2.2.1 (up to quadrupole order) with a Fourier transform so that they can be extracted from a transient simulation. The subsitution $\mathbf{J} = i\omega\epsilon_0\left(\tilde{\epsilon_r} - 1\right)\mathbf{E}$ is also used for the definition of induced current density.

$$\mathbf{p}\left(\omega\right) = \epsilon_0(\epsilon_r - 1)\tilde{F}\left\{\int \mathbf{E}(t)d^3r\right\}, \tag{D.1}$$

$$\mathbf{m}(\omega) = \frac{i\omega}{2c}\epsilon_0(\epsilon_r - 1)\tilde{F}\left\{\int \mathbf{r}\times\mathbf{E}(t)d^3r\right\}, \tag{D.2}$$

$$\mathbf{T}(\omega) = \frac{i\omega}{10c}\epsilon_0(\epsilon_r - 1)\tilde{F}\left\{\int \left[\lfloor\mathbf{r}\cdot\mathbf{E}(t)\rfloor\,\mathbf{r} - 2r^2\mathbf{E}(t)\right]d^3r\right\}, \tag{D.3}$$

$$Q_{\alpha\beta}(\omega) = \frac{1}{2}\epsilon_0(\epsilon_r - 1)\tilde{F}\left\{\int \left[r_\alpha E_\beta(t) + r_\beta E_\alpha(t) - \frac{2}{3}\delta_{\alpha\beta}\lfloor\mathbf{r}\cdot\mathbf{E}(t)\rfloor\right]d^3r,\right\} \tag{D.4}$$

$$M_{\alpha\beta}(\omega) = \frac{i\omega}{3c}\epsilon_0(\epsilon_r - 1)\tilde{F}\left\{\int \left[\lfloor\mathbf{r}\times\mathbf{E}(t)\rfloor_\alpha r_\beta + \lfloor\mathbf{r}\times\mathbf{E}(t)\rfloor_\beta r_\alpha\right]d^3r\right\}, \tag{D.5}$$

Where $\tilde{F}$ represents the Fourier transform from the time to the frequency domain. This gives the Fourier spectra of the microscopic multipoles from a time-dependent simulation.

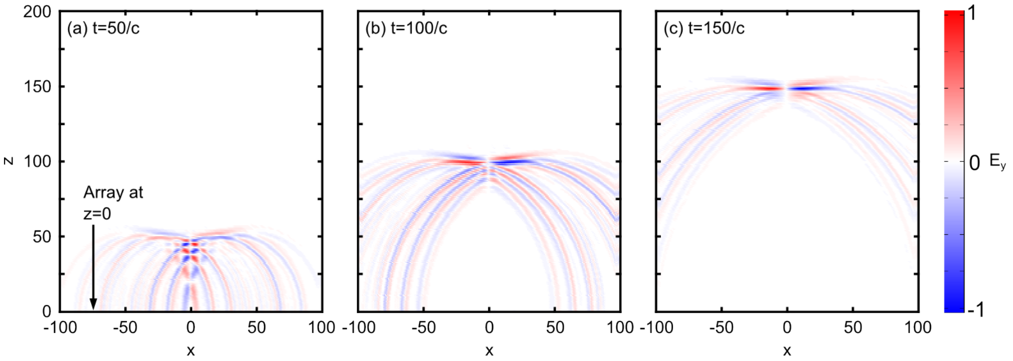

Figure E.1: ***Transverse electric field of a "focused doughnut" pulse generated by a metamaterial dipole array.*** *This figure illustrates the excitation of a dipole array located a* $z = 0$ *resulting in a "focused doughnut" pulse in the far field. (a-c) depict the transverse i.e. out-of-plane E-field on an xz cross-section in front of the dipole array. Three successive time shots show the evolution of the E-field as it propagates away from the array.*

E Fields generated by "focused doughnut" generation scheme

In Chapter 6 it was demonstrated that "focused doughnut" pulses could be synthesised from metasurface dipoles array with a 93% accuracy. The results in this chapter were presented in terms of intensity maps of the fields emitted from the array [Fig. 6.5]. In this appendix, we shall additionally examine the fields emitted by the array to complement the intensity plots and clarify the polarisation of the generated pulse.

Fig. E.1 depicts the equivalent FD generation scheme as shown in Section 6.3 (only depicted over a z range of 0-200) at three time points, but plots the transverse i.e. out-of-plane component of the E-field as opposed to the E-field intensity.

The azimuthal polarisation of the generated pulse is clear from these plots, as indicated by the out-of-phase field components for positive and negative x values. The plots here can be directly compared with the analytic FD field plots presented in Fig. 5.3 to give a qualitative comparison between the analytic FD and our generated pulse.

It can be noted that the radiation generated by the array with low k_z values i.e. primarily propagating along the $x - direction$, is clearly visible in these field plots. This radiation would be responsible for inter-dipole interaction in the generating array and would be a relevant concern for experimental relaisations of this scheme.

F Publications

F.1 Peer-reviewed articles

- T. A. Raybould, V. A. Fedotov, N. Papasimakis, I. J. Youngs, and N. I. Zheludev, “Electromagnetic excitation of anapole and toroidal modes in dielectric particles”, submitted to ACS Photonics.
- T. A. Raybould, V. A. Fedotov, N. Papasimakis, I. Kuprov, I. J. Youngs, W. T. Chen, D. P. Tsai and N. I. Zheludev, “Toroidal circular dichroism”, Physical Review B **94**, 035119 (2016).
- N. Papasimakis, V. A. Fedotov, V. Savinov, T. A. Raybould, and N. I. Zheludev, “Electromagnetic toroidal excitations in matter and free space”, Nature Materials **15**, 263 (2016).
- T. A. Raybould, V. A. Fedotov, N. Papasimakis, I. J. Youngs, and N. I. Zheludev, “Focused electromagnetic doughnut pulses and their interaction with interfaces and nanostructures”, Optics Express **24**, 3150 (2016).

F.2 To-be published

- N. Papasimakis, T. A. Raybould, V. A. Fedotov, I. J. Youngs, and N. I. Zheludev, “Generation of electromagnetic flying toroids from metamaterial arrays”
- T. A. Raybould, V. A. Fedotov, N. Papasimakis, I. J. Youngs, and N. I. Zheludev, “Interaction of structured light with toroidal scatterers”

F.3 Conference contributions

- (poster) T. A. Raybould, N. Papasimakis, V. A. Fedotov, I. Youngs, and N. I. Zheludev, “Generation of flying electromagnetic doughnuts via spatiotemporal conversion of transverse electromagnetic pulses”, Nanometa 2017, Seefeld, Austria, 4 - 7 Jan 2017.
- (invited) T. A. Raybould, V. Savinov, N. Papasimakis, V. A. Fedotov, and N. I. Zheludev, “Electromagnetic doughnuts: localised and propagating toroidal excitations enabled by metamaterials”, Metamaterials 2016, Chania, Greece, 17 - 22 Sep 2016.
- (invited) T. A. Raybould, V. Savinov, N. Papasimakis, V. A. Fedotov, and N. I. Zheludev, “Metamaterials as a platform to study localised and propagating toroidal excitations”, CIMTEC 2016, Perugi, Italy, 5 - 9 June 2016.

- (poster) T. A. Raybould, V. A. Fedotov, N. Papasimakis, I. Youngs, and N. I. Zheludev, "Toroidal excitations in space and matter", New Horizons for Nanophotonics, Newport Pagnell, UK, 23 - 24 May 2016.
- (invited) T. A. Raybould and N. I. Zheludev, "Flying and localized electromagnetic doughnuts", KnIFE Programme Lunchtime Seminar, DSTL, Porton Down, UK, 14 Mar 2016.
- (poster) T. A. Raybould, V. A. Fedotov, N. Papasimakis, I. Youngs, and N. I. Zheludev, "Toroidal excitations in space and matter", Defence and Security Doctoral Symposium, Cranfield, UK, 25 - 26 Nov 2015.
- (oral) T. A. Raybould, V. A. Fedotov, N. Papasimakis, I. Kuprov, I. Youngs, W. T. Chen, D. P. Tsai, and N. I. Zheludev, "Chiral phenomena in toroidal metamaterials", Metamaterials 2015, Oxford, UK, 7 - 12 Sep 2015.
- (oral) T. A. Raybould, V. A. Fedotov, N. Papasimakis, I. Youngs, and N. I. Zheludev, "Propagating toroidal electromagnetic excitations and their interactions with metamaterials and nanostructures", Metamaterials 2015, Oxford, UK, 7 - 12 Sep 2015.
- (invited) N. I . Zheludev, V. A. Fedotov, N. Papasimakis, V. Savinov, T. A. Raybould, and I. Youngs, "Propagating and localized toroidal excitations in free space and metamaterials", SPIE Optics and Photonics 2015, San Diego, CA, USA, 9 - 13 Aug 2015.
- (invited) T. A. Raybould, V. A. Fedotov, N. Papasimakis, I. Youngs, and N. I. Zheludev, "Interrogating nanoparticles with focused doughnuts", PIERS 2015, Prague, Czech Republic, 6 - 9 Jul 2015.
- (oral) T. A. Raybould, V. A. Fedotov, N. Papasimakis, I. Youngs, W. T. Chen, D. P. Tsai, and N. I. Zheludev, "A new type of optical activity in a toroidal metamaterial", PIERS 2015, Prague, Czech Republic, 6 - 9 Jul 2015.
- (oral) T. A. Raybould, V. A. Fedotov, N. Papsimakis, I. J. Youngs, W. T. Chen, D. P. Tsai, and N. I. Zheludev, "New enantiomeric phenomena in toroidal media", CLEO/Europe-EQEC 2015, Munich, Germany 21 - 25 Jun 2015.
- (oral) T. A. Raybould, V. A. Fedotov, N. Papasimakis, I. Youngs, W. T. Chen, D. P. Tsai, and N. I. Zheludev, "A new type of optical activity in a toroidal metamaterial", CLEO 2015, San Jose, CA, USA, 10 - 15 May 2015.
- (oral) T. A. Raybould, V. A. Fedotov, N. Papasimakis, I. Youngs, and N. I. Zheludev, "Interrogating nanoparticles with focused doughnut pulses", Optical Wave and Waveguide Theory and Numerical Modelling Workshop, London, UK, 17 - 18 Apr 2015.

- (poster) T. A. Raybould, V. A. Fedotov, N. Papasimakis, I. Youngs, N. I. Zheludev, “Flying electromagnetic toroids: propagation properties and light-matter interactions”, Nanometa 2015, Seefeld, Austria, 5 - 8 Jan 2015.
- (invited) N. I. Zheludev, V. A. Fedotov, T. A. Raybould, N. Papasimakis, V. Savinov and I. Youngs, “Metamaterials, toroids and flying donuts”, IEEE Photonics Conference 2014, San Diego, CA USA, 12 - 16 Oct 2014.
- (poster) T. A. Raybould, N. Papasimakis, V. A. Fedotov, I. Youngs, and N. I. Zheludev, “Interaction of flying electromagnetic doughnut with nanostructures”, CLEO 2014, San Jose, CA, USA, 8 - 13 Jun 2014.

Bibliography

[1] N. I. Zheludev, “The Road Ahead for Metamaterials,” *Science*, vol. 328, p. 582, 2010.

[2] N. I. Zheludev, “A Roadmap for Metamaterials,” *Optics and Photonics News*, vol. 22, p. 30, Mar. 2011.

[3] N. I. Zheludev and Y. S. Kivshar, “From metamaterials to metadevices.,” *Nature materials*, vol. 11, pp. 917–24, Nov. 2012.

[4] J. B. Pendry, D. Schurig, and D. R. Smith, “Controlling electromagnetic fields.,” *Science*, vol. 312, p. 1780, June 2006.

[5] U. Leonhardt, “Optical conformal mapping.,” *Science*, vol. 312, p. 1777, June 2006.

[6] U. Leonhardt and T. G. Philbin, “Transformation Optics and the Geometry of Light,” p. 72, May 2008.

[7] T. Kaelberer, V. A. Fedotov, N. Papasimakis, D. P. Tsai, and N. I. Zheludev, “Toroidal dipolar response in a metamaterial.,” *Science*, vol. 330, p. 1510, Dec. 2010.

[8] D. J. Griffiths, *Introduction to Electrodynamics.* Prentice Hall, Inc., 3rd ed., 1999.

[9] J. D. Jackson, *Classical Electrodynamics.* John Wiley & Sons, Inc., 3rd ed., 1998.

[10] L. D. Landau and E. M. Lifshitz, *The Classical Theory of Fields.* Pergamon Press, 1971.

[11] R. E. Raab and O. L. de Lange, *Multipole Theory in Electromagnetism.* Oxford Science Publications, 2005.

[12] I. B. Zel’dovich, “Electromagnetic interaction with parity violation,” *Journal of Experimental and Theoretical Physics*, vol. 6, no. 6, p. 1184, 1958.

[13] V. V. Flambaum and D. W. Murray, “Anapole moment and nucleon weak interactions,” *Physical Review C*, vol. 56, no. 3, pp. 1641–1644, 1997.

[14] V. V. Flambaum and I. B. Khriplovich, "P-odd nuclear forces-a source of parity violation in atoms," *Journal of Experimental and Theoretical Physics*, vol. 52, no. 5, pp. 835–839, 1981.

[15] A. Ceulemans and L. F. Chibotaru, "Molecular Anapole Moments," *Physical Review Letters*, vol. 80, no. 9, pp. 1861–1864, 1998.

[16] G. N. Afanasiev and V.M. Dubovik, "Some remarkable charge–current configurations," *Physics of Particles and Nuclei*, vol. 29, p. 366, July 1998.

[17] G. N. Afanasiev, "Simplest sources of electromagnetic fields as a tool for testing the reciprocity-like theorems," *Journal of Physics D: Applied Physics*, vol. 34, p. 539, Feb. 2001.

[18] M. Dubovik and A. Tosunyan, "Axial toroidal moments in electrodynamics and solid-state physics," *Journal of Experimental and Theoretical Physics*, vol. 605, no. June 1985, p. 344, 1986.

[19] V. Dubovik and V. Tugushev, "Toroid moments in electrodynamics and solid-state physics," *Physics Reports*, vol. 187, pp. 145–202, Mar. 1990.

[20] R. W. Hellwarth and P. Nouchi, "Focused one-cycle electromagnetic pulses," *Physical Review E*, vol. 54, p. 889, July 1996.

[21] S. Suzuki, Y. Segawa, K. Itami, and J. Yamaguchi, "Synthesis and characterization of hexaarylbenzenes with five or six different substituents enabled by programmed synthesis.," *Nature chemistry*, vol. 7, pp. 227–33, Mar. 2015.

[22] R. Kovall and B. W. Matthews, "Toroidal Structure of Lambda-Exonuclease," *Science*, vol. 277, pp. 1824–1827, Sept. 1997.

[23] L. Joshua-Tor, H. Xu, S. Johnston, and D. Rees, "Crystal structure of a conserved protease that binds DNA: the bleomycin hydrolase, Gal6," *Science*, vol. 269, pp. 945–950, Aug. 1995.

[24] A. A. Simpson, Y. Tao, P. G. Leiman, M. O. Badasso, Y. He, P. J. Jardine, N. H. Olson, M. C. Morais, S. Grimes, D. L. Anderson, T. S. Baker, and M. G. Rossmann, "Structure of the bacteriophage phi29 DNA packaging motor.," *Nature*, vol. 408, pp. 745–50, Dec. 2000.

[25] C. M. Ho and R. J. Scherrer, "Anapole dark matter," *Physics Letters B*, vol. 722, pp. 341–346, May 2013.

[26] J. D. Seelig and V. Jayaraman, "Neural dynamics for landmark orientation and angular path integration," *Nature*, vol. 521, pp. 186–191, May 2015.

[27] N. A. Spaldin, M. Fiebig, and M. Mostovoy, "The toroidal moment in condensed-matter physics and its relation to the magnetoelectric effect," *Journal of Physics: Condensed Matter*, vol. 20, p. 434203, Oct. 2008.

[28] C. S. Wood, S. C. Bennett, D. Cho, B. P. Masterson, J. L. Roberts, C. E. Tanner, and C. E. Wieman, “Measurement of Parity Nonconservation and an Anapole Moment in Cesium,” *Science*, vol. 275, pp. 1759–1763, Mar. 1997.

[29] V. M. Dubovik, “Material equations for electromagnetism with toroidal polarizations,” *Physical Review E*, vol. 61, no. 6, pp. 7087–7097, 2000.

[30] C. Ederer and N. A. Spaldin, “Towards a microscopic theory of toroidal moments in bulk periodic crystals,” *Physical Review B*, vol. 76, p. 214404, Dec. 2007.

[31] N. A. Tolstoi and A. A. Spartakov, “Aromagnetism: A new type of magnetism,” *Journal of Experimental and Theoretical Physics Letters*, vol. 52, no. 3, p. 161, 1990.

[32] M. A. Martsenyuk and N. M. Martsenyuk, “On the origin of aromagnetism,” *Journal of Experimental and Theoretical Physics Letters*, vol. 52, no. 3, p. 229, 1991.

[33] V. A. Fedotov, K. Marinov, A. D. Boardman, and N. I. Zheludev, “On the aromagnetism and anapole moment of anthracene nanocrystals,” *New Journal of Physics*, vol. 9, p. 95, Apr. 2007.

[34] D. Khomskii, “Classifying multiferroics: Mechanisms and effects,” *Physics*, vol. 2, p. 20, Mar. 2009.

[35] A. P. Pyatakov and A. K. Zvezdin, “Magnetoelectric and multiferroic media,” *Physics-Uspekhi*, vol. 55, pp. 557–581, June 2012.

[36] C. Kittel, “Theory of the Structure of Ferromagnetic Domains in Films and Small Particles,” *Physical Review*, vol. 70, p. 965, 1946.

[37] I. S. Zheludev, E. M. Perekalina, T. M. Smirnovskaya, S. S. Fonton, and Y. N. Yarmukhamedov, “Magnetic properties of nickel-boracite iodide,” *JETP Letters*, vol. 20, p. 129, 1974.

[38] V. Ginzburg, A. Gorbatsevich, Y. Kopayev, and B. Volkov, “On the problem of superdiamagnetism,” *Solid State Communications*, vol. 50, pp. 339–343, Apr. 1984.

[39] D. G. Sannikov and I. S. Zheludev, “On the possibility of phase transitions with spontaneous toroidal moment formation in nickel boracites,” *Soviet Physics - Solid State*, vol. 27, p. 826, 1985.

[40] B. B. Van Aken, J.-P. Rivera, H. Schmid, and M. Fiebig, “Observation of ferrotoroidic domains.,” *Nature*, vol. 449, pp. 702–5, Oct. 2007.

[41] A. S. Zimmermann, D. Meier, and M. Fiebig, “Ferroic nature of magnetic toroidal order.,” *Nature communications*, vol. 5, p. 4796, Jan. 2014.

[42] G. N. Afanasiev and Y. P. Stepanovsky, "The electromagnetic field of elementary time-dependent toroidal sources," *Journal of Physics A: Mathematical and General*, vol. 28, p. 4565, Aug. 1995.

[43] E. Radescu and D. Vlad, "Angular momentum loss by a radiating toroidal dipole," *Physical Review E*, vol. 57, p. 6030, May 1998.

[44] E. Radescu and G. Vaman, "Exact calculation of the angular momentum loss, recoil force, and radiation intensity for an arbitrary source in terms of electric, magnetic, and toroid multipoles," *Physical Review E*, vol. 65, Apr. 2002.

[45] C. Vrejoiu, "Electromagnetic multipoles in Cartesian coordinates," *Journal of Physics A: Mathematical and General*, vol. 35, p. 9911, Nov. 2002.

[46] A. Gongora and E. Ley-Koo, "Complete electromagnetic multipole expansion including toroidal moments," *Revista Mexicana De Física*, vol. 52, pp. 188–197, 2006.

[47] K. Cho, "Microscopic Expression of Chiral Susceptibilities," in *Metamaterials '2011: The Fifth International Congress on Advanced Electromagnetic Materials in Microwaves and Optics*, pp. 672–674, 2011.

[48] F. B. Arango and A. Femius Koenderink, "Polarizability tensor retrieval for magnetic and plasmonic antenna design," *New Journal of Physics*, vol. 15, p. 073023, July 2013.

[49] P. Grahn, A. Shevchenko, and M. Kaivola, "Electromagnetic multipole theory for optical nanomaterials," *New Journal of Physics*, vol. 14, p. 093033, Sept. 2012.

[50] X.-L. Zhang, S. B. Wang, Z. Lin, H.-B. Sun, and C. T. Chan, "Optical force on toroidal nanostructures: Toroidal dipole versus renormalized electric dipole," *Physical Review A*, vol. 92, p. 043804, Oct. 2015.

[51] A. E. Miroshnichenko, A. B. Evlyukhin, Y. F. Yu, R. M. Bakker, A. Chipouline, A. I. Kuznetsov, B. Luk'yanchuk, B. N. Chichkov, and Y. S. Kivshar, "Non-radiating anapole modes in dielectric nanoparticles," *Nature Communications*, vol. 6, p. 8069, Aug. 2015.

[52] V. Savinov, V. A. Fedotov, and N. I. Zheludev, "Toroidal dipolar excitation and macroscopic electromagnetic properties of metamaterials," *Physical Review B*, vol. 89, p. 205112, May 2014.

[53] K. M. Aggarwal and F. P. Keenan, "Radiative rates for E1, E2, M1, and M2 transitions in S-like to F-like tungsten ions (W LIX to W LXVI)," *Atomic Data and Nuclear Data Tables*, vol. 111-112, pp. 187–279, Sept. 2016.

[54] S. Narayana and Y. Sato, “Heat flux manipulation with engineered thermal materials.,” *Physical review letters*, vol. 108, p. 214303, May 2012.

[55] R. Schittny, M. Kadic, S. Guenneau, and M. Wegener, “Experiments on Transformation Thermodynamics: Molding the Flow of Heat,” *Physical Review Letters*, vol. 110, p. 195901, May 2013.

[56] Z. G. Nicolaou and A. E. Motter, “Mechanical metamaterials with negative compressibility transitions.,” *Nature materials*, vol. 11, pp. 608–13, July 2012.

[57] X. Zheng, H. Lee, T. H. Weisgraber, M. Shusteff, J. DeOtte, E. B. Duoss, J. D. Kuntz, M. M. Biener, Q. Ge, J. A. Jackson, S. O. Kucheyev, N. X. Fang, and C. M. Spadaccini, “Ultralight, ultrastiff mechanical metamaterials.,” *Science (New York, N.Y.)*, vol. 344, pp. 1373–7, June 2014.

[58] J. Christensen, M. Kadic, O. Kraft, and M. Wegener, “Vibrant times for mechanical metamaterials,” *MRS Communications*, vol. 5, pp. 453–462, July 2015.

[59] S. A. Cummer, J. Christensen, and A. Alù, “Controlling sound with acoustic metamaterials,” *Nature Reviews Materials*, vol. 1, p. 16001, Feb. 2016.

[60] M.-H. Lu, L. Feng, and Y.-F. Chen, “Phononic crystals and acoustic metamaterials,” *Materials Today*, vol. 12, pp. 34–42, Dec. 2009.

[61] C. Caloz and T. Itoh, *Electromagnetic Metamaterials: Transmission Line Theory and Microwave Applications*. John Wiley & Sons, Inc., 2005.

[62] N. Yu and F. Capasso, “Flat optics with designer metasurfaces.,” *Nature materials*, vol. 13, pp. 139–50, Feb. 2014.

[63] N. Papasimakis, V. A. Fedotov, Y. Fu, D. Tsai, and N. I. Zheludev, “Coherent and incoherent metamaterials and order-disorder transitions,” *Physical Review B*, vol. 80, p. 1, July 2009.

[64] R. A. Shelby, D. R. Smith, and S. Schultz, “Experimental verification of a negative index of refraction.,” *Science*, vol. 292, p. 77, Apr. 2001.

[65] D. Schurig, J. J. Mock, B. J. Justice, S. A. Cummer, J. B. Pendry, A. F. Starr, and D. R. Smith, “Metamaterial electromagnetic cloak at microwave frequencies.,” *Science (New York, N.Y.)*, vol. 314, p. 977, Nov. 2006.

[66] N. Papasimakis, V. A. Fedotov, N. Zheludev, and S. Prosvirnin, “Metamaterial Analog of Electromagnetically Induced Transparency,” *Physical Review Letters*, vol. 101, p. 253903, Dec. 2008.

[67] N. Yu, P. Genevet, M. A. Kats, F. Aieta, J.-P. Tetienne, F. Capasso, and Z. Gaburro, “Light propagation with phase discontinuities: generalized laws of reflection and refraction.,” *Science (New York, N.Y.)*, vol. 334, pp. 333–7, Oct. 2011.

[68] D. Emerson, “The work of Jagadis Chandra Bose: 100 years of millimeter-wave research,” *IEEE Transactions on Microwave Theory and Techniques*, vol. 45, no. 12, pp. 2267–2273, 1997.

[69] D. R. Smith, W. J. Padilla, D. C. Vier, and S. Schultz, “Composite Medium with Simultaneously Negative Permeability and Permittivity,” *Physical Review Letters*, vol. 84, p. 4184, 2000.

[70] D. R. Smith, J. B. Pendry, and M. C. K. Wiltshire, “Metamaterials and negative refractive index.,” *Science*, vol. 305, p. 788, Aug. 2004.

[71] T. J. Yen, W. J. Padilla, N. Fang, D. C. Vier, D. R. Smith, J. B. Pendry, D. N. Basov, and X. Zhang, “Terahertz magnetic response from artificial materials.,” *Science*, vol. 303, p. 1494, Mar. 2004.

[72] J. Pendry, “Negative refraction makes a perfect lens,” *Physical Review Letterseview letters*, vol. 85, p. 3966, Oct. 2000.

[73] Z. Jacob, L. V. Alekseyev, and E. Narimanov, “Optical Hyperlens: Far-field imaging beyond the diffraction limit,” *Optics Express*, vol. 14, no. 18, p. 8247, 2006.

[74] Z. Liu, H. Lee, Y. Xiong, C. Sun, and X. Zhang, “Far-field optical hyperlens magnifying sub-diffraction-limited objects.,” *Science (New York, N.Y.)*, vol. 315, p. 1686, Mar. 2007.

[75] A. Boltasseva and H. A. Atwater, “Materials science. Low-loss plasmonic metamaterials.,” *Science (New York, N.Y.)*, vol. 331, pp. 290–1, Jan. 2011.

[76] V. Savinov, A. Tsiatmas, A. R. Buckingham, V. A. Fedotov, P. A. J. de Groot, and N. I. Zheludev, “Flux exclusion superconducting quantum metamaterial: towards quantum-level switching.,” *Scientific reports*, vol. 2, p. 450, Jan. 2012.

[77] V. Savinov, V. A. Fedotov, S. M. Anlage, P. A. J. de Groot, and N. I. Zheludev, “Modulating sub-THz radiation with current in superconducting metamaterial.,” *Physical review letters*, vol. 109, p. 243904, Dec. 2012.

[78] R. Singh and N. Zheludev, “Materials: Superconductor photonics,” *Nature Photonics*, vol. 8, pp. 679–680, Sept. 2014.

[79] M. Ricci, N. Orloff, and S. M. Anlage, “Superconducting metamaterials,” *Applied Physics Letters*, vol. 87, p. 034102, July 2005.

[80] N. Papasimakis and N. I. Zheludev, “Metamaterial-Induced Transparency: Sharp Fano Resonances and Slow Light,” *Optics and Photonics News*, vol. 20, p. 22, Oct. 2009.

[81] N. I. Zheludev, S. L. Prosvirnin, N. Papasimakis, and V. A. Fedotov, “Lasing spaser,” *Nature Photonics*, vol. 2, p. 351, May 2008.

[82] Y. W. Huang, W. T. Chen, P. C. Wu, V. A. Fedotov, N. I. Zheludev, and D. P. Tsai, “Toroidal lasing spaser.,” *Scientific reports*, vol. 3, p. 1237, Jan. 2013.

[83] B. Walther, C. Helgert, C. Rockstuhl, F. Setzpfandt, F. Eilenberger, E. B. Kley, F. Lederer, A. Tünnermann, and T. Pertsch, “Spatial and spectral light shaping with metamaterials.,” *Advanced materials*, vol. 24, p. 6300, Dec. 2012.

[84] S. Enoch, G. Tayeb, P. Sabouroux, N. Guérin, and P. Vincent, “A metamaterial for directive emission.,” *Physical review letters*, vol. 89, p. 213902, Nov. 2002.

[85] A. Alu, F. Bilotti, N. Engheta, and L. Vegni, “Subwavelength, Compact, Resonant Patch Antennas Loaded With Metamaterials,” *IEEE Transactions on Antennas and Propagation*, vol. 55, pp. 13–25, Jan. 2007.

[86] N. I. Zheludev and E. Plum, “Reconfigurable nanomechanical photonic metamaterials.,” *Nature Nanotechnology*, vol. 11, pp. 16–22, Jan. 2016.

[87] P. Genevet, N. Yu, F. Aieta, J. Lin, M. A. Kats, R. Blanchard, M. O. Scully, Z. Gaburro, and F. Capasso, “Ultra-thin plasmonic optical vortex plate based on phase discontinuities,” *Applied Physics Letters*, vol. 100, no. 1, p. 013101, 2012.

[88] N. I. Landy, S. Sajuyigbe, J. J. Mock, D. R. Smith, and W. J. Padilla, “Perfect metamaterial absorber.,” *Physical review letters*, vol. 100, p. 207402, May 2008.

[89] H.-t. Chen, “Interference theory of metamaterial perfect absorbers,” *Optics Express*, vol. 20, no. 7, pp. 7165–7172, 2012.

[90] I. V. Shadrivov, A. B. Kozyrev, D. W. van der Weide, and Y. S. Kivshar, “Tunable transmission and harmonic generation in nonlinear metamaterials,” *Applied Physics Letters*, vol. 93, p. 161903, Oct. 2008.

[91] L. Luo, I. Chatzakis, J. Wang, F. B. P. Niesler, M. Wegener, T. Koschny, and C. M. Soukoulis, “Broadband terahertz generation from metamaterials.,” *Nature communications*, vol. 5, p. 3055, Jan. 2014.

[92] P. Macha, G. Oelsner, J.-M. Reiner, M. Marthaler, S. André, G. Schön, U. Hübner, H.-G. Meyer, E. Il’ichev, and A. V. Ustinov, “Implementation of a quantum metamaterial using superconducting qubits.,” *Nature communications*, vol. 5, p. 5146, Oct. 2014.

[93] J. Q. Quach, C.-h. Su, A. M. Martin, A. D. Greentree, and L. C. L. Hollenberg, “Reconfigurable quantum metamaterials,” *Optics Express*, vol. 19, no. 12, pp. 11018–11033, 2011.

[94] M. a. Castellanos-Beltran, K. D. Irwin, G. C. Hilton, L. R. Vale, and K. W. Lehnert, “Amplification and squeezing of quantum noise with a tunable Josephson metamaterial,” *Nature Physics*, vol. 4, pp. 929–931, Oct. 2008.

[95] X. He, “Tunable terahertz graphene metamaterials,” *Carbon*, vol. 82, pp. 229–237, Feb. 2015.

[96] A. Andryieuski and A. V. Lavrinenko, “Graphene metamaterials based tunable terahertz absorber : effective surface conductivity approach,” *Optics Express*, vol. 21, no. 7, pp. 9144–9155, 2013.

[97] A. B. Khanikaev, S. H. Mousavi, W.-K. Tse, M. Kargarian, A. H. MacDonald, and G. Shvets, “Photonic topological insulators.,” *Nature materials*, vol. 12, pp. 233–9, Mar. 2013.

[98] A. Karvounis, B. Gholipour, K. F. Macdonald, and N. I. Zheludev, “All-dielectric phase-change reconfigurable metasurface,” *Applied Physics Letters*, vol. 051103, pp. 3–7, 2016.

[99] R. F. Waters, P. A. Hobson, K. F. Macdonald, and N. I. Zheludev, “Optically switchable photonic metasurfaces,” *Applied Physics Letters*, vol. 081102, pp. 3–6, 2015.

[100] K. Marinov, A. D. Boardman, V. A. Fedotov, and N. I. Zheludev, “Toroidal metamaterial,” *New Journal of Physics*, vol. 9, p. 324, Sept. 2007.

[101] N. Papasimakis, V. A. Fedotov, K. Marinov, and N. I. Zheludev, “Gyrotropy of a Metamolecule: Wire on a Torus,” *Physical Review Letters*, vol. 103, p. 1, Aug. 2009.

[102] Z.-G. Dong, P. Ni, J. Zhu, X. Yin, and X. Zhang, “Toroidal dipole response in a multifold double- ring metamaterial,” *Optics Express*, vol. 20, no. 12, pp. 13065–13070, 2012.

[103] Q. W. Ye, L. Y. Guo, M. H. Li, Y. Liu, B. X. Xiao, and H. L. Yang, “The magnetic toroidal dipole in steric metamaterial for permittivity sensor application,” *Physica Scripta*, vol. 88, p. 055002, Nov. 2013.

[104] Y. Fan, Z. Wei, H. Li, H. Chen, and C. M. Soukoulis, “Low-loss and high-Q planar metamaterial with toroidal moment,” *Physical Review B*, vol. 87, p. 115417, Mar. 2013.

[105] V. Savinov, K. Delfanazari, V. A. Fedotov, and N. I. Zheludev, “Planar Superconducting Toroidal Metamaterial: A Source for Oscillating Vector-Potential?,” in *CLEO: 2014*, (Washington, D.C.), p. FTu1C.1, OSA, 2014.

[106] M. Gupta, V. Savinov, N. Xu, L. Cong, G. Dayal, S. Wang, W. Zhang, N. I. Zheludev, and R. Singh, “Sharp Toroidal Resonances in Planar Terahertz Metasurfaces.,” *Advanced materials (Deerfield Beach, Fla.)*, July 2016.

[107] V. Savinov, *Novel Toroidal and Superconducting Metamaterials.* PhD thesis, University of Southampton, 2014.

[108] P. C. Wu, W. T. Chen, Y.-W. Huang, W.-L. Hsu, C. Y. Liao, V. A. Fedotov, V. Savinov, N. I. Zheludev, and D. P. Tsai, "Three-dimensional metamaterials: from split ring resonator to toroidal metamolecule," vol. 9163, p. 91630M, Sept. 2014.

[109] Z.-G. Dong, J. Zhu, J. Rho, J.-Q. Li, C. Lu, X. Yin, and X. Zhang, "Optical toroidal dipolar response by an asymmetric double-bar metamaterial," *Applied Physics Letters*, vol. 101, no. 14, p. 144105, 2012.

[110] J. Li, Y. Zhang, R. Jin, Q. Wang, Q. Chen, and Z. Dong, "Excitation of plasmon toroidal mode at optical frequencies by angle-resolved reflection," *Optics letters*, vol. 39, no. 23, pp. 6683–6686, 2014.

[111] B. Ögüt, N. Talebi, R. Vogelgesang, W. Sigle, and P. A. van Aken, "Toroidal plasmonic eigenmodes in oligomer nanocavities for the visible.," *Nano letters*, vol. 12, pp. 5239–44, Oct. 2012.

[112] A. A. Basharin, M. Kafesaki, E. N. Economou, C. M. Soukoulis, V. A. Fedotov, V. Savinov, and N. I. Zheludev, "Dielectric Metamaterials with Toroidal Dipolar Response," *Physical Review X*, vol. 5, p. 011036, Mar. 2015.

[113] V. A. Fedotov, A. V. Rogacheva, V. Savinov, D. P. Tsai, and N. I. Zheludev, "Resonant transparency and non-trivial non-radiating excitations in toroidal metamaterials.," *Scientific reports*, vol. 3, p. 2967, Jan. 2013.

[114] C. Ding, L. Jiang, C. Sun, L. Wu, D. Xu, G. Zhang, and J. Yao, "Stable terahertz toroidal dipolar resonance in a planar metamaterial," *Physica Status Solidi (B)*, vol. 6, pp. 1–6, Mar. 2015.

[115] Y. W. Huang, W. T. Chen, P. C. Wu, V. A. Fedotov, V. Savinov, Y. Z. Ho, Y. F. Chau, N. I. Zheludev, and D. P. Tsai, "Design of plasmonic toroidal metamaterials at optical frequencies.," *Optics Express*, vol. 20, p. 1760, Jan. 2012.

[116] P. C. Wu, W. T. Chen, Y.-W. Huang, W.-L. Hsu, C. Y. Liao, V. A. Fedotov, V. Savinov, N. I. Zheludev, and D. P. Tsai, "Three-dimensional metamaterials: from split ring resonator to toroidal metamolecule," in *Proc. SPIE 9163* (A. D. Boardman, ed.), p. 91630M, Sept. 2014.

[117] Z.-G. Dong, J. Zhu, X. Yin, J. Li, C. Lu, and X. Zhang, "All-optical Hall effect by the dynamic toroidal moment in a cavity-based metamaterial," *Physical Review B*, vol. 87, p. 245429, June 2013.

[118] Q. Zhang, J. J. Xiao, and S. L. Wang, "Optical characteristics associated with magnetic resonance in toroidal metamaterials of vertically coupled plasmonic nanodisks," *Journal of the Optical Society of America B*, vol. 31, no. 5, 2014.

[119] S.-H. Kim, S. S. Oh, K.-J. Kim, J.-E. Kim, H. Y. Park, O. Hess, and C.-S. Kee, “Subwavelength localization and toroidal dipole moment of spoof surface plasmon polaritons,” *Physical Review B*, vol. 91, p. 035116, Jan. 2015.

[120] W. Liu, J. Zhang, and A. E. Miroshnichenko, “Toroidal dipole-induced transparency in core-shell nanoparticles,” *Laser & Photonics Reviews*, vol. 9, pp. 564–570, Sept. 2015.

[121] Y. Bao, X. Zhu, and Z. Fang, “Plasmonic Toroidal Dipolar Response under Radially Polarized Excitation.,” *Scientific reports*, vol. 5, p. 11793, Jan. 2015.

[122] W. Liu, J. Zhang, B. Lei, H. Hu, and A. E. Miroshnichenko, “Invisible nanowires with interfering electric and toroidal dipoles,” *Optics letters*, vol. 40, no. 10, pp. 2293–2296, 2015.

[123] A. M. Zagoskin, A. Chipouline, E. Il’ichev, J. R. Johansson, and F. Nori, “Toroidal qubits: naturally-decoupled quiet artificial atoms.,” *Scientific reports*, vol. 5, p. 16934, Jan. 2015.

[124] R. W. Ziolkowski, “Localized transmission of electromagnetic energy,” *Physical Review A*, vol. 39, p. 2005, Feb. 1989.

[125] C. G. Gray, “Multipole expansions of electromagnetic fields using Debye potentials,” *American Journal of Physics*, vol. 46, no. 2, p. 169, 1978.

[126] A. D. Boardman, K. Marinov, N. Zheludev, and V. A. Fedotov, “Nonradiating toroidal structures,” pp. 595504–595504–12, Sept. 2005.

[127] E. A. Marengo and R. W. Ziolkowski, “Nonradiating sources, the Aharonov-Bohm effect, and the question of measurability of electromagnetic potentials,” *Radio Science*, vol. 37, pp. 19–1–19–10, Dec. 2002.

[128] S. Mühlig, C. Menzel, C. Rockstuhl, and F. Lederer, “Multipole analysis of meta-atoms,” *Metamaterials*, vol. 5, p. 64, June 2011.

[129] P. Grahn, A. Shevchenko, and M. Kaivola, “Electromagnetic multipole theory for optical nanomaterials,” *New Journal of Physics*, vol. 14, p. 093033, Sept. 2012.

[130] A. Chipouline, S. Sugavanam, J. Petschulat, and T. Pertsch, “Extension of the Multipole Approach to Random Metamaterials,” *Advances in OptoElectronics*, vol. 2012, p. 1, 2012.

[131] A. A. Pavlov, V. V. Klimov, Y. V. Vladimorova, and V. N. Zadkov, “Analysis of optical properties of planar metamaterials by calculating multipole moments of their constituent meta-atoms,” *Quantum Electronics*, vol. 43, p. 496, May 2013.

[132] B. Gallinet, J. Butet, and O. J. F. Martin, “Numerical methods for nanophotonics: standard problems and future challenges,” *Laser & Photonics Reviews*, vol. 9, pp. 577–603, Nov. 2015.

[133] W. Frei, “Using Perfectly Matched Layers and Scattering Boundary Conditions for Wave Electromagnetics Problems,” *[www.comsol.com/blogs/using-perfectly-matched-layers-and-scattering-boundary-conditions-for-wave-electromagnetics-problems/]*.

[134] E. Isaacson and H. B. Keller, *Analysis of Numerical Methods.* Courier Corporation, 1994.

[135] W. T. Kelvin, *Baltimore Lectures on Molecular Dynamics and the Wave Theory of Light.* Clay & Sons, London, 1904.

[136] Y. Saito and H. Hyuga, “Colloquium : Homochirality: Symmetry breaking in systems driven far from equilibrium,” *Reviews of Modern Physics*, vol. 85, pp. 603–621, Apr. 2013.

[137] T. D. Lee and C. N. Yang, “Question of Parity Conservation,” *Physical Review*, vol. 104, no. 1, pp. 254–258, 1956.

[138] The Jefferson Lab PVDIS Collaboration, “Measurement of parity violation in electron-quark scattering.,” *Nature*, vol. 506, pp. 67–70, Feb. 2014.

[139] L. M. Pasteur, “Sur les relations qui peuvent exister entre la forme cristalline, la composition chimique et le sens de la polarisation rotatoire,” *Annales de Chimie et de Physique*, vol. 24, p. 442, 1848.

[140] L. D. Barron, *Molecular light scattering and optical activity.* Cambridge University Press, 2004.

[141] L. Whitmore and B. A. Wallace, “Protein secondary structure analyses from circular dichroism spectroscopy: methods and reference databases.,” *Biopolymers*, vol. 89, pp. 392–400, May 2008.

[142] A. Kirilyuk, A. V. Kimel, and T. Rasing, “Ultrafast optical manipulation of magnetic order,” *Reviews of Modern Physics*, vol. 82, pp. 2731–2784, Sept. 2010.

[143] E. U. Condon, “Theories of Optical Rotatory Power,” *Reviews of Modern Physics*, vol. 9, p. 432, Oct. 1937.

[144] J. A. Schellman, “Symmetry rules for optical rotation,” *Accounts of Chemical Research*, vol. 1, pp. 144–151, May 1968.

[145] H. Nakano and H. Kimura, “Quantum Statistical-Mechanical Theory of Optical Activity,” *Journal of the Physical Society of Japan*, vol. 27, p. 519, 1969.

[146] A. D. Buckingham and M. B. Dunn, "Optical activity of oriented molecules," *Journal of the Chemical Society A: Inorganic, Physical, Theoretical*, vol. 38, p. 1988, 1971.

[147] T. Kosaka, Y. Inoue, and T. Mori, "Toroidal Interaction and Propeller Chirality of Hexaarylbenzenes. Dynamic Domino Inversion Revealed by Combined Experimental and Theoretical Circular Dichroism Studies.," *The journal of physical chemistry letters*, vol. 7, pp. 783–8, Mar. 2016.

[148] J. Gao, K. Zhang, G. Yang, and Q. Wu, "A Novel Four-Face Polarization Twister Based on Three-Dimensional Magnetic Toroidal Dipoles," *IEEE Transactions on Magnetics*, vol. 50, pp. 1–4, Jan. 2014.

[149] M. J. Urban, P. K. Dutta, P. Wang, X. Duan, X. Shen, B. Ding, Y. Ke, and N. Liu, "Plasmonic Toroidal Metamolecules Assembled by DNA Origami.," *Journal of the American Chemical Society*, vol. 138, pp. 5495–8, May 2016.

[150] E. Saenz, I. Semchenko, S. Khakhomov, K. Guven, R. Gonzalo, E. Ozbay, and S. Tretyakov, "Modeling of Spirals with Equal Dielectric, Magnetic, and Chiral Susceptibilities," *Electromagnetics*, vol. 28, pp. 476–493, Sept. 2008.

[151] M. Thiel, H. Fischer, G. von Freymann, and M. Wegener, "Three-dimensional chiral photonic superlattices," *Optics Letters*, vol. 35, no. 2, pp. 166–168, 2010.

[152] Rogers Corporation, "TMM 3 Laminates," *[www.rogerscorp.com/acs/products/46/TMM-3- Laminates.aspx]*.

[153] R. Oron, S. Blit, N. Davidson, A. A. Friesem, Z. Bomzon, and E. Hasman, "The formation of laser beams with pure azimuthal or radial polarization," *Applied Physics Letters*, vol. 77, no. 21, p. 3322, 2000.

[154] L. Yang, X. Xie, S. Wang, and J. Zhou, "Minimized spot of annular radially polarized focusing beam," *Optics letters*, vol. 38, no. 8, pp. 1331–1333, 2013.

[155] R. Dorn, S. Quabis, and G. Leuchs, "Sharper focus for a radially polarized light beam.," *Physical review letters*, vol. 91, p. 233901, Dec. 2003.

[156] A. V. Failla, H. Qian, A. Hartschuh, and A. J. Meixner, "Orientational imaging of subwavelength Au particles with higher order laser modes.," *Nano letters*, vol. 6, pp. 1374–8, July 2006.

[157] W. Chen, D. C. Abeysinghe, R. L. Nelson, and Q. Zhan, "Plasmonic lens made of multiple concentric metallic rings under radially polarized illumination.," *Nano letters*, vol. 9, pp. 4320–5, Dec. 2009.

[158] J. Zeng, X. Wang, J. Sun, A. Pandey, A. N. Cartwright, and N. M. Litchinitser, "Manipulating complex light with metamaterials.," *Scientific reports*, vol. 3, p. 2826, Jan. 2013.

[159] J. Lin, P. Genevet, M. A. Kats, N. Antoniou, and F. Capasso, “Nanostructured holograms for broadband manipulation of vector beams.,” *Nano letters*, vol. 13, pp. 4269–74, Sept. 2013.

[160] D. W. Watson, S. D. Jenkins, J. Ruostekoski, V. a. Fedotov, and N. I. Zheludev, “Toroidal dipole excitations in metamolecules formed by interacting plasmonic nanorods,” *Physical Review B*, vol. 93, p. 125420, Mar. 2016.

[161] J. Li, J. Shao, J.-Q. Li, X. Yu, Z.-G. Dong, Q. Chen, and Y. Zhai, “Optical responses of magnetic-vortex resonance in double-disk metamaterial variations,” *Physics Letters A*, vol. 378, pp. 1871–1875, May 2014.

[162] H. Wheeler, “Fundamental Limitations of Small Antennas,” *Proceedings of the IRE*, vol. 35, pp. 1479–1484, Dec. 1947.

[163] L. J. Chu, “Physical Limitations of Omni-Directional Antennas,” *Journal of Applied Physics*, vol. 19, no. 12, p. 1163, 1948.

[164] R. F. Harrington, “Effect of Antenna Size on Gain , Bandwidth , and Efficiencyl,” *Journal of the National Bureau of Standards*, vol. 64D, no. 1, pp. 1–12, 1960.

[165] P. Hazdra, M. Capek, and J. Eichler, “Radiation Q Factors of Thin-Wire Dipole Arrangements,” *IEEE Antennas and Wireless Propagation Letters*, vol. 10, no. 8, pp. 556–560, 2011.

[166] H. E. Hernandez-Figueroa, M. Zamboni-Rached, and E. Recami, *Localised Waves.* John Wiley & Sons, Inc., 2008.

[167] J. N. Brittingham, “Focus waves modes in homogeneous Maxwell’s equations: Transverse electric mode,” *Journal of Applied Physics*, vol. 54, no. 3, p. 1179, 1983.

[168] S. Feng, H. Winful, and R. Hellwarth, “Spatiotemporal evolution of focused single-cycle electromagnetic pulses,” *Physical Review E*, vol. 59, p. 4630, Apr. 1999.

[169] J. Y. Lu and J. F. Greenleaf, “Nondiffracting X waves - exact solutions to free-space scalar wave equation and their finite aperture realizations.,” *IEEE Transactions on Ultrasonics, Ferroelectrics, and Frequency Control*, vol. 39, p. 19, Jan. 1992.

[170] A. Chong, W. H. Renninger, D. N. Christodoulides, and F. W. Wise, “Airy–Bessel wave packets as versatile linear light bullets,” *Nature Photonics*, vol. 4, p. 103, Jan. 2010.

[171] A. M. Shaarawi, I. M. Besieris, R. W. Ziolkowski, and S. M. Sedky, “Generation of approximate focus-wave-mode pulses from wide-band dynamic Gaussian

apertures," *Journal of the Optical Society of America A*, vol. 12, p. 1954, Sept. 1995.

[172] A. M. Shaarawi, I. M. Besieris, and R. W. Ziolkowski, "Localized energy pulse trains launched from an open, semi-infinite, circular waveguide," *Journal of Applied Physics*, vol. 65, no. 2, p. 805, 1989.

[173] Z. Wang, Q. Lin, and Z. Wang, "Single-cycle electromagnetic pulses produced by oscillating electric dipoles," *Physical Review E*, vol. 67, p. 016503, Jan. 2003.

[174] K. Reivelt and P. Saari, "Experimental demonstration of realizability of optical focus wave modes," *Physical Review E*, vol. 66, p. 056611, Nov. 2002.

[175] S. Hunsche, S. Feng, H. G. Winful, A. Leitenstorfer, M. C. Nuss, and E. P. Ippen, "Spatiotemporal focusing of single-cycle light pulses," *Journal of the Optical Society of America A*, vol. 16, no. 8, p. 2025, 1999.

[176] S. Winnerl, R. Hubrich, M. Mittendorff, H. Schneider, and M. Helm, "Universal phase relation between longitudinal and transverse fields observed in focused terahertz beams," *New Journal of Physics*, vol. 14, p. 103049, Oct. 2012.

[177] K. Kan, J. Yang, A. Ogata, S. Sakakihara, T. Kondoh, K. Norizawa, I. Nozawa, T. Toigawa, Y. Yoshida, H. Kitahara, K. Takano, M. Hangyo, R. Kuroda, and H. Toyokawa, "Radially polarized terahertz waves from a photoconductive antenna with microstructures," *Applied Physics Letters*, vol. 102, no. 22, p. 221118, 2013.

[178] K. J. Kaltenecker, J. C. König-Otto, M. Mittendorff, S. Winnerl, H. Schneider, M. Helm, H. Helm, M. Walther, and B. M. Fischer, "Gouy phase shift of a tightly focused, radially polarized beam," *Optica*, vol. 3, p. 35, Jan. 2016.

[179] R. W. Ziolkowski, D. Lewis, and B. Cook, "Evidence of localized wave transmission.," *Physical Review Letters*, vol. 62, p. 147, Jan. 1989.

[180] R. W. Ziolkowski and D. K. Lewis, "Verification of the localized-wave transmission effect," *Journal of Applied Physics*, vol. 68, no. 12, p. 6083, 1990.

[181] J. A. Stratton, *Electromagnetic Theory.* New York: McGraw-Hill, 1941.

[182] S. Feng, H. G. Winful, and R. W. Hellwarth, "Gouy shift and temporal reshaping of focused single-cycle electromagnetic pulses," *Optics letters*, vol. 23, p. 385, July 1998.

[183] J. Lekner, "Helical light pulses," *Journal of Optics A: Pure and Applied Optics*, vol. 6, p. 29, Oct. 2004.

[184] J. Durnin and J. J. Miceli, "Diffraction-free beams," *Physical Review Letters*, vol. 58, p. 1499, Apr. 1987.

[185] J. Durnin, "Exact solutions for nondiffracting beams. I. The scalar theory," *Journal of the Optical Society of America A*, vol. 4, p. 651, Apr. 1987.

[186] A. Vasara, J. Turunen, and A. T. Friberg, "Realization of general nondiffracting beams with computer-generated holograms," *Journal of the Optical Society of America A*, vol. 6, p. 1748, Nov. 1989.

[187] R. P. Macdonald, J. Chrostowski, S. A. Boothroyd, and B. A. Syrett, "Holographic formation of a diode laser nondiffracting beam," *Applied Optics*, vol. 32, no. 32, p. 6470, 1993.

[188] C. Sheng, R. Bekenstein, H. Liu, S. Zhu, and M. Segev, "Wavefront shaping through emulated curved space in waveguide settings.," *Nature communications*, vol. 7, p. 10747, Jan. 2016.

[189] V. Garcés-Chávez, D. McGloin, H. Melville, W. Sibbett, and K. Dholakia, "Simultaneous micromanipulation in multiple planes using a self-reconstructing light beam.," *Nature*, vol. 419, p. 145, Sept. 2002.

[190] J. C. Gutiérrez-Vega, M. D. Iturbe-Castillo, and S. Chávez-Cerda, "Alternative formulation for invariant optical fields: Mathieu beams.," *Optics letters*, vol. 25, p. 1493, Oct. 2000.

[191] C. Dartora, M. Zamboni-Rached, K. Nóbrega, E. Recami, and H. Hernández-Figueroa, "General formulation for the analysis of scalar diffraction-free beams using angular modulation: Mathieu and Bessel beams," *Optics Communications*, vol. 222, pp. 75–80, July 2003.

[192] C. Day, "Intense X-Shaped Pulses of Light Propagate Without Spreading in Water and Other," *Physics Today*, vol. 57, no. 10, p. 25, 2004.

[193] G. A. Siviloglou and D. N. Christodoulides, "Accelerating finite energy Airy beams.," *Optics letters*, vol. 32, p. 979, Apr. 2007.

[194] G. A. Siviloglou, J. Broky, A. Dogariu, and D. Christodoulides, "Observation of Accelerating Airy Beams," *Physical Review Letters*, vol. 99, p. 213901, Nov. 2007.

[195] D. Abdollahpour, S. Suntsov, D. G. Papazoglou, and S. Tzortzakis, "Spatiotemporal airy light bullets in the linear and nonlinear regimes.," *Physical review letters*, vol. 105, p. 253901, Dec. 2010.

[196] T. T. Wu and R. W. P. King, "Comment on "Focus wave modes in homogeneous Maxwell's equations: Transverse electric mode"," *Journal of Applied Physics*, vol. 56, no. 9, p. 2587, 1984.

[197] R. W. Ziolkowski, "Exact solutions of the wave equation with complex source locations," *Journal of Mathematical Physics*, vol. 26, no. 4, p. 861, 1985.

[198] A. Sezginer, "A general formulation of focus wave modes," *Journal of Applied Physics*, vol. 57, no. 3, p. 678, 1985.

[199] P. A. Bélanger, "Packetlike solutions of the homogeneous-wave equation," *Journal of the Optical Society of America A*, vol. 1, p. 723, July 1984.

[200] J. Lekner, "Localized electromagnetic pulses with azimuthal dependence," *Journal of Optics A: Pure and Applied Optics*, vol. 6, p. 711, July 2004.

[201] J. Lekner, "Electromagnetic pulses which have a zero momentum frame," *Journal of Optics A: Pure and Applied Optics*, vol. 5, p. 15, July 2003.

[202] R. W. Ziolkowski, I. M. Besieris, and A. M. Shaarawi, "Localized wave representations of acoustic and electromagnetic radiation," *Proceedings of the IEEE*, vol. 79, no. 10, pp. 1371–1378, 1991.

[203] X. Gu, S. Akturk, and R. Trebino, "Spatial chirp in ultrafast optics," *Optics Communications*, vol. 242, pp. 599–604, Dec. 2004.

[204] C. Varin, M. Piché, and M. Porras, "Acceleration of electrons from rest to GeV energies by ultrashort transverse magnetic laser pulses in free space," *Physical Review E*, vol. 71, p. 026603, Feb. 2005.

[205] E. A. Nanni, W. R. Huang, K.-H. Hong, K. Ravi, A. Fallahi, G. Moriena, R. J. D. Miller, and F. X. Kärtner, "Terahertz-driven linear electron acceleration.," *Nature communications*, vol. 6, p. 8486, Jan. 2015.

[206] M. Zamboni-Rached and H. Hernández-Figueroa, "A rigorous analysis of localized wave propagation in optical fibers," *Optics Communications*, vol. 191, pp. 49–54, May 2001.

[207] M. A. Salem and H. Bagci, "On the propagation of truncated localized waves in dispersive silica," *Optics Express*, vol. 18, no. 25, pp. 25482–25493, 2010.

[208] R. Donnelly and D. Power, "The behavior of electromagnetic localized waves at a planar interface," *IEEE Transactions on Antennas and Propagation*, vol. 45, pp. 580–591, Apr. 1997.

[209] I. J. Youngs, N. Bowler, K. P. Lymer, and S. Hussain, "Dielectric relaxation in metal-coated particles: the dramatic role of nano-scale coatings," *Journal of Physics D: Applied Physics*, vol. 38, pp. 188–201, Jan. 2005.

[210] I. J. Youngs, N. Bowler, and O. Ugurlu, "Dielectric relaxation in composites containing electrically isolated particles with thin semi-continuous metal coatings," *Journal of Physics D: Applied Physics*, vol. 39, pp. 1312–1325, Apr. 2006.

[211] R. W. Ziolkowski, "Wave physics and engineering," *Physical Review A*, vol. 44, no. 6, pp. 3960–3984, 1991.

[212] M. Decker, I. Staude, M. Falkner, J. Dominguez, D. N. Neshev, I. Brener, T. Pertsch, and Y. S. Kivshar, "High-Efficiency Dielectric Huygens' Surfaces," *Advanced Optical Materials*, vol. 3, pp. 813–820, June 2015.

[213] R. W. Ziolkowski, "Properties of electromagnetic beams generated by ultra-wide bandwidth pulse-driven arrays," *IEEE Transactions on Antennas and Propagation*, vol. 40, no. 8, pp. 888–905, 1992.

[214] R. W. Ziolkowski, I. M. Besieris, and A. M. Shaarawi, "Aperture realizations of exact solutions to homogeneous-wave equations," *Journal of the Optical Society of America A*, vol. 10, p. 75, Jan. 1993.

[215] R. W. Ziolkowski and P. Jin, "Metamaterial-Based Dispersion Engineering to Achieve High Fidelity Output Pulses From a Log-Periodic Dipole Array," *IEEE Transactions on Antennas and Propagation*, vol. 56, pp. 3619–3629, Dec. 2008.

[216] N. Yu, P. Genevet, M. A. Kats, F. Aieta, J.-P. Tetienne, F. Capasso, and Z. Gaburro, "Light Propagation with Phase Discontinuities: Generalized Laws of Reflection and Refraction," *Science*, vol. 334, pp. 333–337, Sept. 2011.

[217] A. V. Kildishev, A. Boltasseva, and V. M. Shalaev, "Planar photonics with metasurfaces.," *Science*, vol. 339, p. 1232009, Mar. 2013.

[218] P. Genevet, J. Lin, M. A. Kats, and F. Capasso, "Holographic detection of the orbital angular momentum of light with plasmonic photodiodes.," *Nature communications*, vol. 3, p. 1278, Jan. 2012.

[219] V. A. Fedotov, J. Wallauer, M. Walther, M. Perino, N. Papasimakis, and N. I. Zheludev, "Wavevector Selective Metasurfaces and Tunnel Vision Filters," *Light: Science & Applications*, vol. 4, p. e306, July 2015.

[220] F. Monticone, N. M. Estakhri, and A. Alù, "Full control of nanoscale optical transmission with a composite metascreen.," *Physical review letters*, vol. 110, p. 203903, May 2013.

[221] I. Dolev, I. Epstein, and A. Arie, "Surface-Plasmon Holographic Beam Shaping," *Physical Review Letters*, vol. 109, p. 203903, Nov. 2012.

[222] C. Pfeiffer and A. Grbic, "Metamaterial Huygens' Surfaces: Tailoring Wave Fronts with Reflectionless Sheets," *Physical Review Letters*, vol. 110, p. 197401, May 2013.

[223] A. Arbabi, Y. Horie, M. Bagheri, and A. Faraon, "Dielectric metasurfaces for complete control of phase and polarization with subwavelength spatial resolution and high transmission.," *Nature nanotechnology*, vol. 10, pp. 937–43, Nov. 2015.

[224] S. Wang and Q. Zhan, "Reflection type metasurface designed for high efficiency vectorial field generation.," *Scientific reports*, vol. 6, p. 29626, Jan. 2016.

[225] T. Udem, J. Reichert, R. Holzwarth, and T. W. Hänsch, “Absolute Optical Frequency Measurement of the Cesium D 1 Line with a Mode-Locked Laser,” *Physical Review Letters*, vol. 82, pp. 3568–3571, May 1999.

[226] J. Stenger, H. Schnatz, C. Tamm, and H. R. Telle, “Ultraprecise measurement of optical frequency ratios.,” *Physical Review Letters*, vol. 88, p. 073601, Feb. 2002.

[227] K. Wang and D. M. Mittleman, “Metal wires for terahertz wave guiding.,” *Nature*, vol. 432, pp. 376–9, Nov. 2004.

[228] J. T. Leung, “Singular behaviour of the electrodynamic fields of an oscillating dipole,” *European Journal of Physics*, vol. 29, p. 137, Oct. 2008.

[229] S. D. Jenkins and J. Ruostekoski, “Theoretical formalism for collective electromagnetic response of collective metamaterial systems,” *Phys. Rev. B*, vol. 86, p. 085116, Oct. 2012.